Modification of optoelectrical properties of ZnO based thin films using Ar plasma treatment and post annealing with Al capping layer

by

Dao Thi Hoa

Student ID number: 1216006

A dissertation submitted to the
Engineering course, Department of Engineering,
Graduate School of Engineering,
Kochi University of Technology,
Kochi, Japan

for the degree of
Doctor of Philosophy

Assessment Committee:
Supervisor: Prof. Hisao Makino
Co-Supervisor: Prof. Chaoyang Li
Co-Supervisor: Prof. Hiroshi Furuta
Committee Member: Prof. Akimitsu Hatta
Committee Member: Prof. Mamoru Furuta

March, 2020

Abstract

Modification of optoelectrical properties of ZnO based thin films using Ar plasma treatment and post annealing with Al capping layer

ZnO based thin films have attracted much attention for applications in optoelectronic devices. Because of wide band gap of ~ 3.37 eV and high exciton binding energy of ~ 60 meV, ZnO is promising material for efficient UV light emitting devices and UV laser. Moreover, ZnO can be doped to become sufficiently conductive, with resistivity of ~10^{-4} Ωcm, that is especially promising for application as transparent electrodes (TEs). However, electrical and optical properties of ZnO based thin films are very sensitive to crystalline perfections and defects states, which depend on preparation procedures. Though enormous studies have been done on ZnO thin films and gained noticeable progress, the issues on defects, grain boundaries, film crystallinity and their correlations with optoelectrical properties of ZnO based thin films are being challenges and have not been fully elucidated. Better understandings about conducting mechanisms and defects formation are crucial for improving performance of devices based on ZnO films.

One important application of ZnO based thin films is TEs. For this application, ZnO based thin films should have good thermal stability to keep its high transparency and high electrical conductivity under thermal stress during device fabrication. Unfortunately, ZnO based thin films showed degradation in electrical properties under annealing. Using capping layers on ZnO films resulted in better thermal stability. However, the improvements were not enough, the degradation was still observed, even with thick capping layer (several tens or hundreds nm). Moreover, the degradation mechanism is under debate.

Therefore, this research was carried out in order to:

- Find simple methods to improve optoelectrical properties of ZnO based thin films, for application in transparent electrodes, or light emitting devices.
- Elucidate the relationship between defects states with optical and electrical properties.
- Get understanding on the thermal degradation mechanism of electrical properties of Al-doped ZnO (AZO) thin films, which is most promising ZnO based materials for applications as transparent electrodes.
- Improve thermal stability of AZO thin films.

In the first part of this research, Ar plasma treatment in a low vacuum chamber was employed to improve optoelectrical properties of ZnO thin films. The enhancement in electrical properties, the increase in near band edge emissions and the suppression of deep level emissions were obtained. Such improvements might be originated from the defect passivation and donor states of H, which incorporated into ZnO film during the plasma treatment.

The second part of the research concerns the electrical properties of AZO films and their thermal stability. Effect of crystallinity on thermal stability of AZO samples under annealing in N_2 gas was studied. The thermal degradation of electrical properties of AZO films under annealing in N_2 can be attributed to the Zn desorption and segregation of defects at the grain boundaries. Ultrathin (2.2 nm thick) Al capping layer, which was deposited using magnetron sputtering on AZO films, can prevent the Zn desorption and then prevent the degradation of electrical properties of AZO film under annealing in N_2 gas. Especially, an improvement in Hall mobility, to ~ 49 - 54 cm^2/Vs, was obtained in the Al coated AZO (Al/AZO) sample with good *c*-axis oriented AZO film deposited at relatively high substrate temperature. However, the Al capping layer could not passivate contribution of misaligned tilting domains to the grain boundaries scattering and the segregation of defects to GBs in sample with poor crystallinity deposited at low substrate temperature, resulting in the reduction in Hall mobility after the annealing at high temperature.

Thermal stability of AZO and Al/AZO samples under annealing in air was investigated. Compared to the annealing in N_2, annealing in air resulted in stronger reduction in carrier concentration and Hall mobility, possibly due to effects of oxygen. The ultrathin (2.2 nm-thick) Al capping layer exhibited insufficient effects. The degradation in electrical properties was still observed with annealing at a high temperature of 500 °C. Thicker Al capping layers, with thickness up to 10.8 nm, can prevent the degradation for a specific annealing duration. The maintenance of high conductivity was found strongly related to the interaction and interdiffusion between Al capping layer and bottom AZO layer, as well as to the existence of a non-equilibrium layer which revealed an absorption peak in visible range. The Ar plasma in low vacuum chamber was employed to increase the retention time of low resistance of Al/AZO samples, owing to the deceleration of the interaction and interdiffusion between capping and bottom layer. Our findings can be applied to optoelectronic devices which require high temperature processes.

Contents

List of Figures

List of Tables

Chapter 1. ZnO – promising material for optoelectronic devices

1.1. Brief introduction

Studies on ZnO material have been started from the mid-19th century [1]. ZnO is an attractive semiconductor material having a direct band gap around 3.37 eV and a high exciton binding energy of 60 meV [2]. With this energy gap, ZnO is transparent in the visible (Vis) region but absorbs the ultraviolet (UV) lights. Moreover, its exciton binding energy is much larger than room temperature thermal energy (kT~26 meV), makes it become extremely promising materials for UV detector, light emitting devices (LED) and laser [3-7]. The ionic covalent bonding feature of Zn-O and its high piezoelectric coefficient make ZnO as very promising materials for piezotronic transducer and sensor [4, 8, 9]. Moreover, ZnO materials are easily integrated with other substances to modify its properties, therefore, ZnO was used in gas sensor, biosensor and photocatalyst [4, 10, 11]. Additionally, due to non-toxicity, bio-compatibility and bio-degradability, ZnO has been employed in biomedicine, cosmetics, and textile industries [1, 10, 12]. Naturally, ZnO is non-stoichiometric semiconductor with n-type conduction properties. With small electron effective mass and high mobility, as well as modifiable opto-electrical properties, ZnO is strong candidates for applications in semiconductor devices such as transparent transistors, transparent resistive memories, and transparent electrodes [13-16]. Even though fabricating p-type conductive materials based on ZnO is hardly overcome due to its natural n-type properties, attractions on ZnO materials increased by years, because of its unique physical and chemical properties. ZnO can exist in both nanometric scale with all 0D, 1D, 2D or 3D structures such as nanodots and nanoparticles (0D), nanorods, nano-needles, nanowires, nanotubes, nanocombs (1D), nanosheets, nanoplates (2D) or nano-flower, nano-snowflakes (3d), and micrometric scale including thin film and solid bulk, with variety of fabrication methods including chemical methods such as sol-gel, solvothermal, hydrothermal, spray-pyrolysis, electrolysis, atomic layer deposition (ALD), and physical methods such as sputtering, pulsed laser deposition (PLD), electron-beam deposition, molecular-beam epitaxy [10, 12]. Below are basic properties of ZnO and potential application of ZnO based thin film in opto-electronic devices, as well as the scope of the thesis.

1.2. Structure properties

1.2.1. Crystalline structure

ZnO belongs to II-IV compound semiconductor with ionicity between covalent and ionic bonding. It exists in three types of crystalline structure, they are wurzite (Fig. 1.1 (a)), zinc blende (Fig. 1. 1 (b)) and rocksalt (Fig. 1. 1 (c)). In most of cases, ZnO exists in form of wurzite structure, which is well known the most stable and most common phase of ZnO [2] in normal conditions. Zinc blende structure was formed only when ZnO was grown on cubic substrate, and rocksalt structure need to be grown in relatively high pressure ~10 GPa [1, 2].

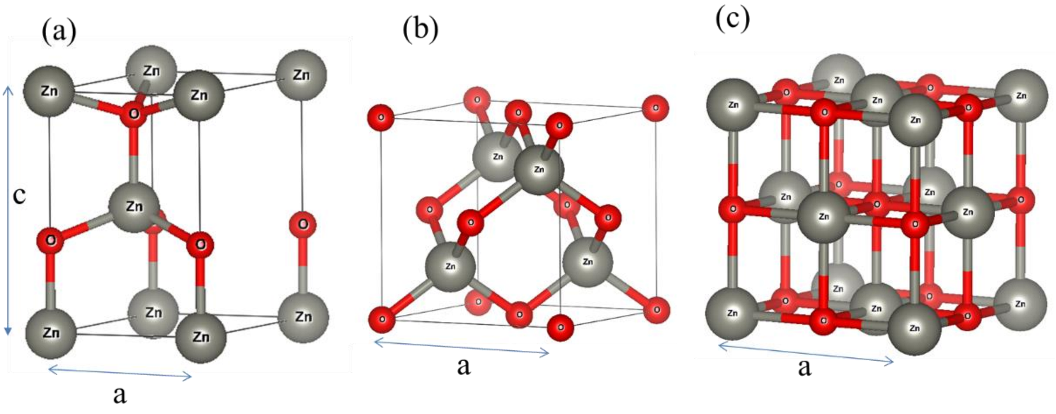

Fig. 1. 1. Crystalline structures of ZnO: Wurtzite (a), Zinc Blende (b), and Rocksalt (c).

The wurzite structure has a hexagonal unit cell with two lattice parameters, *a* and *c*, with the ideal ratio of $c/a = \sqrt{8/3}$ and belong to the space group of $P6_3mc$ (in Hermann-Mauguin notation). This structure comprises of two interpenetrating hexagonal close-packed sublattices of O atoms and Zn atoms, each of sublattice displaced along the threefold of *c*-axis by an amount of u ~3/8 with respect to each other. This is the nearest-neighbor distance of cation-anion bond length. Each sublattice unit cell consists of 4 atoms. Due to nature of sp^3 covalent bonding, each atom of one kind of element is surrounded by four atoms of other kind which locate at the corners of a tetrahedral, and vice versa. The crystallographic vectors of the wurzite structure are $\vec{a}$ = a (1/2, $\sqrt{3}$/2, 0), $\vec{b}$ = a (1/2, $-\sqrt{3}$/2, 0) and $\vec{c}$ = c (0, 0, 1). In Cartesian coordination, the basis atoms are (0, 0, 0), (0, 0, uc), a(1/2, $\sqrt{3}$/6, c/2a) and a(1/2, $\sqrt{3}$/6, (u +1/2)c/a). In practical, the wurzite structure can derivate from the ideal arrangements, depends on compositions, impurities, point defects and dislocations, and external strain [2]. For ZnO, *a* lattice constant is around ~3.247 – 3.250 Å, *c* is around ~5.204 – 5.207 Å, and u is ~ 0.383 – 0.385. *a* and *c* lattice constants in wurtzite structure can be estimated via X-ray diffraction profiles, by using inter-planar spacing according to following equation:

$$\frac{1}{d_{hkl}^2} = \frac{4}{3}\frac{h^2+k^2+hk}{a^2} + \frac{l^2}{c^2} \tag{1.1}$$

where *h, k, l* are miller indexes of the diffraction plane, d_{hkl} is inter-planar spacing of (hkl) planes.

In wurzite structure, due to nature of sp^3 bonding, the growing in [0001] direction is preferred, with lowest surface energy [17]. Therefore, in almost ZnO films, which were not grown on single crystal substrates, *c*-axis was preferred orientation. For polycrystalline ZnO films, the alignment of crystalline domains have strong influence on properties of ZnO films, not only piezo-electrical properties but also optoelectrical properties, which can be explained by large number of defects located at grain boundaries (GBs) [18, 19].

1.2.2. Crystallographic polarity

For crystals grown in *c*-axis direction of a wurzite structure, there are two un-equivalent faces, which consist of Zn atoms and O atoms. Due to lack of inversion symmetry, and polar feature of Zn-O bonding, in wurzite structure, there is an existence of a spontaneous polarization along the *c*-axis direction, leading to a crystallographic polarity. The direction points from the O plane to Zn plane was defined as $\langle 0001 \rangle$ and has been considered as positive *c*-axis direction. Therefore, the Zn plane is defined as (0001) plane and O plane is (000$\bar{1}$), and when the bonds along the *c*-axis from the O to Zn, the polarity is referred as O polarity and vice versa, if bonds from Zn to O, the polarity was called Zn polar (Fig. 1.2). Due to different outermost atomic species on two polar faces, the properties of ZnO materials varied with its polarity, including chemical stability and reactivity, defect generation caused by high energy bombardment, incorporation of impurities, and the crystalline growth of over layer [20-22]. These differences lead to different behaviors and performances of devices using ZnO material with different polarities [20].

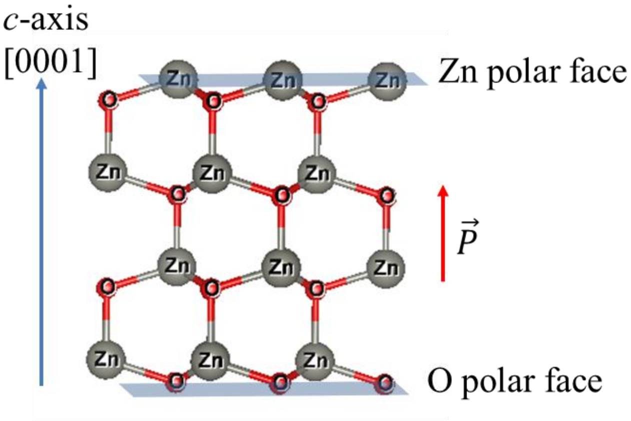

Fig. 1. 2. Polarity in wurtzite structure of ZnO.

1.3. Electrical and optical properties

1.3.1. Electrical properties - defects and charge carrier scatterings

Electrical conductivity is proportional to the carrier concentration and carrier mobility, and given by:

$$\sigma = ne\mu \tag{1.2}$$

with e is electron charge, n is carrier concentration, and μ is mobility.

The carrier concentration depends strongly on density of donor and acceptor states, and their activation energies inside the material. The mobility represents for the transport ability of carrier, and therefore it is depressed by charge scattering. The mobility is proportional to the relaxation time in which no collision occurs and given by:

$$\mu = \frac{e\langle\tau\rangle}{m^*} \tag{1. 3}$$

where e is electron charge, $\langle\tau\rangle$ is average relaxation time, and m^* is carrier effective mass. The average relaxation time can be calculated, according to Matthiessen's rule as [23]:

$$\langle\tau\rangle = \langle\sum_i \frac{1}{\tau_i}\rangle^{-1} \tag{1.4}$$

with τ_i is relaxation time in each type of scattering.

Then, the mobility should be:

$$\mu = 1/\sum_i \frac{1}{\mu_i} \tag{1.5}$$

During transportation, many types of scatterings can occur with the charge carriers, including carrier-phonon scattering, carrier-point defects scattering, potential barrier scattering, carrier-carrier scattering. Consequently, electrical properties, especially mobility of charge carriers strongly depend on the quality of the crystal, as well as the defect states inside material.

a) *Native defects and impurities*

In stoichiometric semiconductors, the carrier concentration at room temperature is in the order of 10^{13} – 10^{14} cm^{-3}, and practically they behave as insulator. However, pure ZnO material exhibits n-type conductivity and is considered as non-stoichiometric semiconductor with existence of intrinsic point defects such as Zn interstitials (Zn_i), oxygen vacancies (V_O), Zn vacancies (V_{Zn}), O interstitials (O_i) and antisites (Zn_O and O_{Zn}). While V_{Zn}, O_i, O_{Zn} have been considered as acceptors, and compensate the electrical conductivity of ZnO, Zn_i and V_O are donors and have been invoked as source of intrinsic n-type conductivity [2, 24]. However, recently calculation has shown that formation energy of V_O, even under Zn-rich conditions, is quite high, and the transition level of V_O occurs at ~ 1eV below the conduction band, therefore, V_O would be a deep donor instead of shallow donor [25]. According to theoretical calculation, Zn_i is shallow donor. Because of high formation energy and low migration barrier, Zn_i was considered as unstable donor [25]. Nevertheless, it was proposed as a stable donor when exist in complex with N impurities [24]. Recently, the reason for unintentional n-type conductivity of ZnO has been shifted to H interstitial (H_i) after calculation showing that H_i is a shallow donor

[26, 27] with very low migration barrier (0.4 – 0.5 eV) [24]. H was also considered as a passivant, which can substitute to the position of V_O and V_{Zn}, and therefore passivates these defects and becoming ultra-shallow donors. H has been employed in many studies and was found to improve electrical conductivity of ZnO based thin film [28-30]. In addition to the unintentional H doping, C has been also considered as an unintentional doping source accounting for n-type conduction, especially in ZnO fabricated using chemical method such as CVD, ALD but there was not much evidence [24].

Although pure ZnO has intrinsic n-type conduction with electron mobility of ZnO single crystal approximately of ~ 200 cm^2/Vs and carrier concentration around of ~ $10^{16} – 10^{17}$ cm^{-3} [2], the conductivity is not sufficient for application as transparent conductive electrodes. To increase carrier concentration, elements of group III (Al, Ga, In, B) and group IV (Si, Ti, Sn, Zr) have been employed as dopants, which act as shallow donors, and ZnO based thin films having significant low resistivity of ~10^{-4} Ωcm have been successfully fabricated [4, 31, 32]. F and Cl are also treated as shallow donors when substitute to the O sites [33-35]. Recently, numerous efforts have been paid on ZnO based quaternary compounds by cation-cation co-doping such as co-doped Al and Ga, In and Ga, Sn and Ti, or cation-anion co-doping such as Al and F, Sn and F [36]. Although several promising results have been obtained, with resistivity reduced to 10^{-4}-10^{-5} Ωcm, it is necessary to control the trade-off between carrier concentration with Hall mobility and optical transmittance.

Due to intrinsic n-type conduction, it is difficult to fabricated p-type semiconductor based on ZnO, even though great efforts have been done by doping Na, Li, K, Cu, Ag (group I) and N, P, As, or Sb (group V) [24, 37, 38]. The key challenge is creating acceptors efficiently enough to overcome the compensating native donors. Moreover, although theoretical calculation suggested that substitutional group I elements are shallow acceptors, the metal atoms exist in interstitial sites can contribute their one electrons to the free-carriers. Doping N was regarded to be the most promising candidate for p-type ZnO, because of its similar radius with O atoms. The difficulty in doping N is the low dopant solubility and precipitation formation. The theoretical calculation also shown that dopants in group V (P, As, N) are deep acceptors, accompanies with formation of many antisites [39-41]. In addition, the formation of defects during fabrication procedures using high energy bombardment such as sputtering, implantation or plasma assisted processes might cause difficulties to obtain p-type semiconductor.

Though doping can increase the carrier concentration, beside intrinsic defects, lots of new defects and their complexes can be created and prevent the carrier transport and then change the electrical properties.

b) *Charge scatterings*

– **Optical phonon scattering:** This scattering is due to interaction of electrons with electric field induced by lattice vibration polarization (polar longitudinal optical phonon) which occurs in polar semiconductor. This scattering is effective at high temperature range, above 200 K. The mobility can be calculated by [42]:

$$\mu_{op} = \frac{e}{2\alpha\omega_0 m^*}\left[exp\left(\frac{\hbar\omega_0}{KT}\right) - 1\right] \tag{1.5}$$

where $\hbar\omega_0$ is energy of longitudinal optical phonon, $\hbar\omega_0 = 73.1$ meV for ZnO, K is Boltzmann constant and *T* is absolute temperature, m^* is electron effective mass, α is polaron coupling constant, and given by:

$$\alpha = \left(\frac{1}{\epsilon_\infty} - \frac{1}{\epsilon_s}\right)\sqrt{\frac{m^* E_H}{m_e \hbar\omega_0}} \tag{1.6}$$

with ϵ_∞, ϵ_s are high frequency and static dielectric constants, respectively, and $E_H = 13.59\ eV$ is first ionization energy of H atom.

- **Acoustic phonons – deformation potential scattering**: Acoustic phonons lead to change in lattice spacing and therefore, causes the local shift of the band edge, then results in the deformation potential. The mobility is given by [23, 42]:

$$\mu_{dp} = \frac{2\sqrt{2\pi}\hbar^4 c_l e}{3E_1^2 m^{*5/2} (KT)^{3/2}} \tag{1.7}$$

where $\hbar$ is reduced Plank's constant, c_l is longitudinal elastic constant which proportional to the crystal density and square of sound velocity, e is electron charge, E_1 is band-edge deformation potential, but it is not well known and its value is normally calculated through fitting temperature dependence of Hall mobility, K is Boltzmann constant and *T* is absolute temperature. This scattering is dominated at high temperature, and more effective with light effective mass. For ZnO material, it is not dominate like other scattering.

- **Accoustic phonon-piezoelectric deformation scattering**: In polar materials with lack of inversion symmetry, acoustic phonons can induce the deformation of electrical field and cause the scattering. The mobility can be calculated by [23]:

$$\mu_{pie} = \frac{16\sqrt{2\pi}\varepsilon\hbar^2}{3eP^2\sqrt{m^{*3}}KT} \tag{1.8}$$

where P is piezoelectric coupling coefficient, $P = 0.21$ for ZnO material [42].

This mobility is proportional to $T^{-1/2}$, at around room temperature, it is much smaller than other scattering mechanisms. Therefore, electron mobility at room temperature is almost limited by polar optical phonon scattering.

- **Ionized impurity scattering**: The transportation of charge carrier was deflected by Coulomb potential of charged impurities and defects. It is more pronounced in degenerated semiconductor with high doping concentration. For degenerated semiconductors, mobility can be estimated by[23]:

$$\mu_{ii} = \frac{128\sqrt{2\pi}(\varepsilon_r\epsilon_0)^2(KT)^{3/2}}{N_I Z^2 e^3\sqrt{m^*}\left[\ln(1+y) - \frac{y}{1+y}\right]} \tag{1.9}$$

where $y = 24\varepsilon_r\epsilon_0(KT)^2 m^*/\hbar^2 e^2 n$, ε_r is relative dielectric permittivity, ε_0 is vacuum permittivity, N_I is ionized impurities concentration, $N_I = n + 2N_A$ with N_A is acceptor density, Z is the charge of the ionized impurity.

- **Grain boundary (GB) scattering**: In polycrystalline, GBs are discontinuities of crystalline domains, which consist of dangling bonds and defects, resulting in formation of a potential barrier which prevent the transportation of charge carrier. In almost case, transportation though GBs is thermionic emission, and the mobility was proposed by[42, 43]:

$$\mu_{GB} = Le\left(\frac{1}{2m^*\pi KT}\right)^{1/2} exp\left(\frac{-E_B}{KT}\right) \tag{1.10}$$

where L is grain size, E_B is GB potential barrier.

If the GBs are narrow, and charge carriers gain enough energy, they can pass though the GBs by tunneling or field emission.

In addition to the above-mentioned scatterings, other factors can affect the transportation of charge carrier such as neutral impurities scattering, dipole scattering, dislocation scattering, or alloy scattering.

While GBs scattering occurs at the GBs, other scattering mechanisms almost occur inside the crystal domain. Therefore, the total mobility at equation 1.4 can be rewritten as [18]:

$$\mu = 1/\sum_i \frac{1}{\mu_i} = \left(\frac{1}{\mu_{IG}} + \frac{1}{\mu_{GB}}\right)^{-1} \tag{1.11}$$

where μ_{IG} is the mobility of free-carrier inside the crystalline grain, which was normally considered as mobility of free carrier μ_{opt} derived using Drude's model for the optical absorption of free-carriers in degenerated semiconductors.

1.3.2. Optical properties

Optical properties of a semiconductor are related to the transitions of electrons between energy levels, therefore, they depends on the defect states and band structure of the materials.

For ZnO materials, the conduction band was found to consist of s-like state, while the valence band is p-like state, which is split into three bands due to influence of crystal field and spin-orbit interaction, and are usually denoted by A, B, and C from highest to lowest band, with the energy separations are ΔE_{AB}= 8 meV and ΔE_{BC} = 59.8 meV [44]. The direct band gap energy was calculated by the difference of energy from the bottom of CB at Γ point to the top of valence band A is ~ 3.43 eV at low temperature (4.7K) and 3.37 eV at room temperature [2]. The near band edge absorption and emissions are dominated by transitions via three valence bands. The related free-exciton transitions between conduction band and three valence bands have been observed using absorption spectra [45] and low temperature photoluminescence [2]. The A-free-exciton binding energy was observed to be 60 meV which is much higher than thermal energy at room temperature (~ 26 meV), thus allows the room temperature lazing. In addition to the free-exciton transitions, the near band edge emissions (NBEs) of ZnO also consist of transitions related to shallow donor bound excitons and shallow acceptor bound excitons, accompanied with their electron satellites and longitudinal phonon replicas at energy separation of ~ 71-73 meV, which is longitudinal phonon energy of ZnO [2]. The transitions between shallow donor-acceptor pairs have also been supposed to appear in NBEs.

The existence of various defects and their complexes causes the emissions in the Vis range, from the green (~2.4 eV) to red (~1.8 eV) region. Assignment of the emission peaks, so far, is controversial. The green emission (GE) was commonly observed in almost ZnO samples, regardless of preparation methods. The GE was attributed to Cu_{Zn} defects [46]. However, V_O and V_{Zn} defects have also been considered as origins of this emission [47]. Vanheusden et al. [48] observed the correlation between density of singly charged V_O^+ investigated using electron paramagnetic spectroscopy (EPS) with emission intensity of green band and ascribed it to the transitions via V_O^+. Čížek et al. [49] reported that emission at 2.3 eV originated from transition through V_{Zn} associated with H which was supported by positron annihilation spectroscopy

(PAS) and change in photoluminescence (PL) spectra after annealing in Zn vapor, while emission at 2.47 eV related with transition via V_O. The assignment of GE for V_{Zn} was also suggested by theoretical studies of Janotti et al. [25] and Fabbri et al [50], which showed energy transition level of V_{Zn} is ~0.9 eV above the VBM. Ji et al [51] observed the decrease of GE after annealing in O_2 gas, but found the increase in GE after annealing in H_2 gas, both before or after annealing with O_2. Accordingly, they ascribed the GE for both V_O and H-decorated V_{Zn}. Yellow emission peak at ~ 2.1 eV was attributed to O_i [52], but some arguments assigned it to the Li_{Zn}, especially in Li-doped ZnO film [53]. On the other hand, Gonzále et al. [54] argued that the yellow emission should be related to Zn_i and this emission was suppressed after annealed in Ar and O_2 gas. The orange-red emission centered at ~ 1.8 – 1.9 eV was known rarely observed compared to green and yellow emissions. This emission band was also proposed to the transitions related to the excess oxygen [55] or Zn_i [54]. Evidently, though many studies on deep level emissions band of ZnO have been done in literature, the agreement has not been obtained. The confusion might be owing to the broad band and high asymmetry features of the DLEs, which may originate in numerous transitions with close energies.

Beside radiative defects, there are several types of non-radiative defects, such as O adsorbates [47], surface defects and grain boundaries states [56], extended defects (dislocations and stacking faults) [57], V_{Zn} complexes [58], or Zn_i complexes [57]. Due to optical transitions via defects levels lying in the forbidden gap, the NBEs of ZnO are suppressed. The dense concentration of defect levels inside the band gap also are reasons for the absorption tail, or absorption peak in the Vis range [59], lowering the transmittance of ZnO film. Great enhancements in NBEs were observed in ZnO sample which was treated by annealing in H_2 gas or by H_2 plasma [60, 61], accompanied with the decrease in the DLEs. Improvement in PL could be obtained by deposition of ZnO in H_2 gas environment [62]. The effects were attributed to the passivation effect of H on some defects such as Li_{Zn} and Cu_{Zn} [60], V_O [60], V_{Zn} [60].

Enhancements in PL were also attained using AlO_x or TiO_2 capping layer, which were attributed to the passivation of some surface defects and reduce the surface band bending [63]. Surface plasmonic resonance coupling was also employed to improve PL characteristic of ZnO, for example, Al metal film, Au or Ag nanoparticles [64, 65]. Annealing in inert gas at high temperature somehow improved the NBEs of ZnO material [66].

1.4. Applications of ZnO based thin films in optoelectronic devices and challenges

While ZnO nanostructures are favored in applications which require high surface/volume ratio such as gas sensors, bio-sensors and photocatalysts, ZnO based thin films gained most attentions on applications in large scale opto-electronics devices including LEDs, photodetectors, transistors, transparent electrodes, etc. Owing to the difficulties in fabricating p-type ZnO, most of application of ZnO in LEDs are based on structures of metal-insulator-semiconductor (MIS) and p-n heterojunction [67-69]. Recently, several studies on LEDs made of p-n homojunction of ZnO films have been reported [70, 71]. Strong UV-blue emissions were observed at ~ 380-390 nm owing to excitonic transition in ZnO film [5, 67]. Nevertheless, there were emission peaks in green–red region which did not stem from the energy band gap of ZnO, but from defects levels of ZnO [68, 69]. ZnO thin films have also been realized in lasing devices [6, 72, 73]. Ryu et al. [6] reported the lasing actions at room temperature by both optical and electrical pumping of ZnO/BeZnO multi-quantum-wells-based devices. Transparent thin film transistor (TTFT) is another promising application of ZnO thin films [4, 15, 74, 75]. Dong et al [74] successfully fabricated TFTs based on Al-doped ZnO (AZO) thin films which had high on off ratios of $\sim 10^8$ with low subthreshold swing (SS) of 0.71 V/decade and adequate field effect mobility of 1.12 cm^2/Vs. Using bi-layer channel of AZO/AZO, Li et al. [76] obtained transistor with on/off ratio of $\sim 10^7$ and low SS of 0.23 V/decade. Carcia et al. [77] reported ZnO TFT with a high mobility of 17.6 cm^2/Vs, whereas TFTs based on amorphous Si, polycrystalline Si or organic TFT commonly showed mobility smaller than 1 cm^2/Vs [75]. Amorphous oxides based

TFTs were intensively developed, with significantly high mobility, for instance, ~34 cm^2/Vs in indium zinc tin oxide (IZTO) transistor [78], or ~15.67 cm^2/Vs in indium-gallium-zinc oxide (IGZO) transistor [79]. Although noticeable improvements have been obtained in ZnO thin films based TFTs, one needs to care about the degradation of the transistor under stress bias, which was usually attributed to the defects at the interfaces and GBs [14].

The most promising application of ZnO thin films is transparent electrodes (TEs) [4, 13, 36, 80-82]. Because of high conductivity accompanied with high transparency, non-toxicity, and variety of fabrication methods, ZnO based TEs are expected to replace for the tin doped indium oxide (ITO) and fluorine doped tin oxide (FTO). Enormous studies have focused on investigating and improving electrical properties of ZnO based thin films in order to achieve highly conductive electrodes. The low resistivity of ~10^{-4} Ωcm was commonly obtained by doping with Al, Ga and In [18, 31, 36, 83-85]. Agura et al. [86] even reported a significantly low resistivity of ~8.5×10^{-5} Ωcm in Al-doped ZnO (AZO) (2 wt %) film deposited using pulsed laser deposition (PLD) method, while attained high transparency in visible (Vis) range. Extremely low resistivity of 5.1×10^{-5} Ωcm was also obtained in Ga-doped ZnO (GZO) (0.75 at %) deposited on (0001) sapphire substrate by high temperature buffer assisted pulsed laser deposition [87]. The electrical properties of ZnO films doped with other metals including B, Si Ti, Sn, Sr, Hf, so far, are not attractive as the results obtained with Al and Ga dopants, but quite promising, with resistivity almost reached 10^{-4} Ωcm [32, 36, 88, 89]. ZnO films co-doped with two cations such as Al-Ga, Al-Sm, Al-B, Al-Sn, Ti-Al, Ga-In, Ga-Ti [36, 90-94] or co-doped with cation-anion pairs of Al-F, B-F, Ga-F [95-98] showed better conductivity than single doped ZnO films, opening new choices for TEs. H helped to improve electrical properties of doped ZnO films, by introducing H_2 into forming gas or plasma treatment [28, 99]. Doped ZnO films have been widely used as TEs in optoelectronic devices including LED, solar cell, electrochromic devices, and their performances were comparable to ITO or FTO [81, 97, 100, 101].

The opto-electrical properties of ZnO material were shown sensitive to the crystalline perfections and defects states, therefore, in order to obtain novel device performance, it is better to fabricate high quality films and interfaces with minimal defects and disorders. Using single crystal ZnO film might help to achieve novel device performance, due to its perfect crystallinity. However, single crystal manufacturing processes, including vapor transport [102], hydrothermal [103], and molecular beam epitaxy [104], are not scalable and commercialized. Moreover, the growing of epitaxial films on single crystalline substrate meets some obstacles of contaminations from mechanical polishing on the surface, and impurities from substrate holder and ion sources [105], which reduce the quality of the epitaxial ZnO films. Therefore, the growing of single crystal ZnO film needs careful controlling and complicated equipment. Consequently, studies on polycrystalline ZnO films dominated, because of simple and scalable fabrications. Although enormous progresses have been done on ZnO thin films, the issues on defects, crystallinity, grain boundaries and their correlations with opto-electrical properties have not been fully elucidated. Conducting mechanisms are controversial, formation of defects is unclear, causing confusions and difficulties in growing the qualified ZnO films for specific applications.

Another issue on ZnO thin films is stability. Beside degradation in acidic environment, electrical properties of ZnO thin films were known unstable under heating, not only in air but also in vacuum and inert gas [106, 107]. This drawback restrained applications of ZnO films. To date, the mechanism behind the degradation of electrical properties of ZnO thin films were unsolved. Some studies attributed to the Zn desorption and O migration [107, 108] while others ascribed the degradation to the inactivation of metal ions by forming metal oxide bondings at grain boundaries [109]. Moreover, efforts to prevent the degradation of electrical properties of ZnO did not gain expected results [110, 111].

1.5. Motivation and scope of the thesis

In efforts to improve optoelectrical properties of ZnO based films for application in TCOs and LEDs, lots of methods have been employed such as deposition in forming gases, varying the depositions conditions, annealing in various environments, plasma treatment and implantation [37, 58, 68, 83, 99, 112]. Among them, post-plasma treatment is simple and used widely, not affect to the growing process of material. For ZnO material, H_2 plasma treatment shown interesting effects on opto-electrical properties [29, 60, 99]. Unfortunately, the risk of explosion when working with H_2 gas make this treatment non-favored. Other plasma like O_2, Ar, N_2O, N_2, He were usually performed on electronic devices to improve device's performance [113-115], even though the explanations are vague. There was not much studies on singly ZnO film to investigate the influence of plasma on properties of ZnO film.

Annealing has been considered as potential method to improve crystallinity and therefore, properties of many materials. High temperature deposition and treatment are also required in many device fabrication processes. Unfortunately, ZnO films showed the degradation of electrical properties under post-heating treatment. For the point of application as TEs, which are possibly used as substrate for other components in devices, ZnO films should have high conductivity, and good thermal stability to broaden its usages.

In order to increase electrical and optical properties of polycrystalline ZnO based thin films deposited by magnetron sputtering, and get insight into the correlation between defect states and optoelectrical properties of ZnO based thin films, we employed simple Ar plasma treatment. In addition to the motivation of improving electrical properties of ZnO-based thin films, we aimed to improve the thermal stability of their electrical properties, for application as transparent electrode. For this purpose, we employed thin Al film as a capping layer to protect the bottom AZO thin films, which is most exciting ZnO based TEs, under annealing. The defects passivation by plasma treatment as well as by capping layer was studied to get understanding on the correlation between defects and opto-electrical properties of ZnO-based thin films.

Therefore, this thesis consists of:

- Brief introduction on ZnO material including its basic opto-electrical properties and its perspectives has been presented in chapter 1.
- Description on experimental techniques and their usages to prepare and characterize properties of samples will be described in chapter 2.
- Chapter 3 including the discussions on effect of plasma treatment on opto-electrical properties of ZnO and AZO films. The correlation between defects, defects passivation with enhancement in optoelectrical properties, as well as cause of the enhancement obtained by Ar plasma in low vacuum chamber will be discussed.
- Chapter 4 including the discussions on improvements in electrical properties of AZO films and their thermal stability under annealing in N_2 gas obtained with assistance of an ultrathin Al capping layer. Effect of crystallinity on electrical properties and thermal stability, and defects passivation by Al capping layer under annealing will be discussed.
- Chapter 5 describing the passivation effect of Al thin film on thermal stability of electrical properties of AZO film under annealing in air. The influence of interaction and interdiffusion between Al metal capping layer and bottom AZO layer on optical and electrical properties of Al/AZO samples will be discussed. Ar plasma was found to decelerate the interaction and interdiffusion between Al and AZO, prolonging the retention of low resistance of the capped sample.
- Chapter 6 summarizing our findings through the study with their potential applications. The future studies were also recommended.

Main part of our study in chapter 3 related to effect of plasma treatment on optoelectrical properties of ZnO polycrystalline has been published in Materials Science in Semiconductor Processing (*Hoa T. Dao, Hisao Makino, Materials Science in Semiconductor Processing, 96 (2019) 46–52*). Parts of chapter 4 and chapter 5, related to thermal stability of electrical properties of AZO films under different annealing environments and its improvement using ultrathin Al capping layer have been published in Solar Energy Materials and Solar Cells (*Hoa T. Dao, Hisao Makino, Solar Energy Materials and Solar Cells 203 (2019) 110159*).

Reference

[1]. C. Klingshirn, Chem. Phys. Chem., 8 (2007) 782-803.

[2]. Ü. Özgür, Y. I. Alivov, C. Liu, A. Teke, M. A. Reshchikov, S. Doğan, V. Avrutin, S.-J. Cho, H. Morkoç, J. Appl. Phys. , 98 (2005) 041301.

[3]. A. Baltakesmez, S. Tekmen, P. Köç, S. Tüzemen, K. Meral, Y. Onganer, AIP advances, 3 (2013) 032125.

[4]. Ü. Özgür, D. Hofstetter, H. Morkoc, Proc. IEEE, 98 (2010).

[5]. H. Ohta, M. Orita, M. Hirano, H. Hosono, J. Appl. Phys., 89 (2001) 5720.

[6]. Y. R. Ryu, J. A. Lubguban, T. S. Lee, H. W. White, T. S. Jeong, C. J. Youn, B. J. Kim, Appl. phys. Lett., 90 (2007) 131115.

[7]. F. Rahman, Opt. Eng., 58 (2019) 010901.

[8]. L. Wang, S. Liu, X. Feng, Q. Xu, S. Bai, L. Zhu, L. Chen, Y. Qin, Z. L. Wang, ACS nano, 11 (2017) 4859-4865.

[9]. Y. Q. Fu, J. K. Luo, X. Y. Du, A. J. Flewitt, Y. Li, G. H. Markx, A. J. Walton, W. I. Milne, Sens. Actuator B, 143 (2010) 606-619.

[10]. M. A. Borysiewicz, Crystals, 9 (2019) 505.

[11]. L. Zhu, W. Zeng, Sens. Actuator A-Phys., 267 (2017) 242-261.

[12]. A. Kolodziejczak-Radzimska, T. Jesionowski, Materials, 7 (2014) 2833-2881.

[13]. T. Minami, Thin Solid Films, 516 (2008) 5822-5828.

[14]. C. H. Ahn, B. H. Kong, H. Kim, H. K. Cho, J. Electrochem. Soc, 158 (2011) H170-H173.

[15]. H. Frenzel, A. Lajn, H.V. Wenckstern, M. Lorenz, F. Schein, Z. Zhang, M. Grundmann, Adv. Mater., 22 (2010) 5332-5349.

[16]. F. M. Simanjuntak, O. K. Prasad, D. Panda, C. A. Lin, T. L. Tsai, K. H. Wei, T. Y. Tseng, Appl. Phys. Lett., 108 (2016) 183506.

[17]. N. Fujimura, T. Nishihara, S. Goto, F. Xu, T. Ito, J. Cryst. Growth, 130 (1993) 269-279.

[18]. J. Nomoto, H. Makino, T. Yamamoto, J. Appl. Phys., 117 (2015) 045304.

[19]. S. Joshi, M. M. Nayak, K. Rajanna, Appl. Surf. Sci., 296 (2014) 169-176.

[20]. J. Zúñiga-Pérez, V. Consonni, L. Lymperakis, X. Kong, A. Trampert, S. Fernández-Garrido, O. Brandt, H. Renevier, S. Keller, K. Hestroffer, M.R. Wagner, J.S. Reparaz, F. Akyol, S. Rajan, S. Rennesson, T. Palacios, G. Feuillet, Appl. Phys. Rev., 3 (2016) 041303.

[21]. S. Akhter, K. Lui, H.H. Kung, J. Phys. Chem., 89 (1985) 1958-1964.

[22]. A. J. Ramadan, L. A. Rochford, M. P. Ryan, T. S. Jones, S. Heutz, RSC Adv., 5 (2015) 65949.

[23]. D. C. Look, Wiley New York, USA, 1989.

[24]. M. D. McCluskey, S. J. Jokela, J. Appl. Phys. , 106 (2009) 071101.

[25]. A. Janotti, C.G. Van de Walle, Phys. Rev. B, 76 (2007) 165202.

[26]. C.G.Van de Walle, Phys. Rev. Lett, 85 (2000) 1012-1015.

[27]. A. Janotti, C.G. Van de Walle, Rep. Prog. Phys., 72 (2009) 126501.

[28]. Y. Wang, J. Song, W. Zheng, H. Pei, X. Wang, D. Wang, G. Niu, Q. Song, F. Yang, J. Nan, Ceram. Int., 43 (2017) 5396-5402.

[29]. P. F. Cai, J. B. You, X. W. Zhang, J. J. Dong, X. L. Yang, Z. G. Yin, N. F. Chen, J. Appl. Phys., 105 (2009) 083713.

[30]. M. Wu, T. Huang, C. Jin, L. Zhuge, Q. Han, X. Wu, IEEE Trans. Plasma Sci., 42 (2014) 3687-3690.

[31]. A. Singh, S. Chaudhary, D. K. Pandya, Acta Mater., 111 (2016) 1-9.

[32]. H. Sato, T. Minami, S. Takata, J. Vac. Sci. Technol. A 11 (1993) 2975.

[33]. Y. J. Choi, K. M. Kang, H. S. Lee, H. H. Park, J. Mater. Chem. C, 3 (2015) 8336-8343.

[34]. A. Slassi, Y. Ziat, Z. Zarhri, M. Abdellaoui, A.F. Lamrani, Phys. Scr., 90 (2015) 085801.

[35]. A. Slassi, Optik, 126 (2015) 4751-4756.

[36]. A. Mallick, D. Basak, Prog. Mater. Sci., 96 (2018) 86-110.

[37]. S. Y. Tsai, M. H. Hon, Y. M. Lu, J. Cryst. Growth, 326 (2011) 85-89.

[38]. S. Khosravi-Gandomani, R. Yousefi, F. Jamali-Sheini, N.M. Huang, Ceram. Int., 40 (2014) 7957 -7963.

[39]. C. H. Park, S. B. Zhang, S. H. Wei, Phys. Rev. B, 66 (2002) 073202.

[40]. J. L. Lyons, A. Janotti, C. G. Van de Walle, Appl. Phys. Lett, 95 (2009) 252105.

[41]. E. C. Lee, Y. S. Kim, Y. G. Jin, K. J. Chang, Phys. Rev. B, 64 (2001) 085120.

[42]. K. Ellmer, A. Klein, B. Rech, Springer, Berlin, Heidelberg, 2007, pp. 43-61.

[43]. J. Y. F. Seto, J. Appl. Phys., 46 (1975) 5427.

[44]. T. S. Kim, C. J. Youn, T. S. Jeong, J. Korean. Phys. Soc., 38 (2001) 42-46.

[45]. J. F. Muth, R. M. Kolbas, A. K. Sharma, S. Oktyabrsky, J. Narayan, J. Appl. Phys., 85 (1999) 7884.

[46]. D. C. Agarwal, U. B. Singh, S. Gupta, R. Sighhal, P. K. Kulriya, F. Singh, A. Tripathi,

J. Singh, U.S. Joshi, D.K. Avasthi, Sci. Rep., 9 (2018) 6675.

[47]. I. K. Akopyan, M. E. Labzovskaya, A. A. Lisachenko, B. V. Novikov, A. Y. Serov, V. V. Titov, N. G. Filosofov, Phys. Solid State, 58 (2016) 1767-1771.

[48]. K. Vanheusden, W. L. Warren, C. H. Seager, D. R. Tallant, J. A. Voigt, B. E. Gnade, J. Appl. Phys., 79 (1996) 7983.

[49]. J. Čížek, J. Valenta, P. Hruška, O. Melikhova, I. Procházka, M. Novotný, J. Bulíř, Appl. Phys. Lett, 106 (2015) 251902.

[50]. F. Fabbri, M. Villani, A. Catellani, A. Calzolari, G. Cicero, D. Calestani, G. Calestani, A. Zappettini, B. Dierre, T. Sekiguchi, G. Salviati, Sci. Rep., 4 (2014) 5158.

[51]. J. Ji, A. M. Colosimo, W. Anwand, L. A. Boatner, A. Wagner, P.S. Stepanov, T. T. Trinh, M. O. Liedke, R. Krause-Rehberg, T.E. Cowan, F.A. Selim, Sci. Rep., 6 (2016) 31238.

[52]. G. Bajpai, T. Srivastava, S. Kumar, P. Shirage, S. Sen, Structure, Conf. Ser.: Mater. Sci. Eng, 149 (2016) 012186.

[53]. N. Ohashi, N. Ebisawa, T. Sekiguchi, I. Sakaguchi, Y. Wada, T. Takenaka, H. Haneda, Appl. Phys. Lett, 86 (2005) 091902.

[54]. A. González, M. Herrera-Zaldívar, J. Valenzuela, A. Escobedo-Morales, U. Pal, Superlattices Microstruct., 45 (2009) 421-428.

[55]. A.B. Djurišić, Y. H. Leung, K. H. Tam, L. Ding, W. K. Ge, H. Y. Chen, S. Gwo, Appl. Phys. Lett, 88 (2006) 103107.

[56]. T. Matsumoto, H. Kato, K. Miyamoto, M. Sano, T. Yao, Appl. Phys. Lett, 81 (2002) 1231.

[57]. D. Montenegro, V. Hortelano, O. Martínez, M. C. Martínez-Tomas, V. Sallet, V. Muñoz, J. Jiménez, Mater. Res. Soc. Symp. Proc., 1538 (2013) 317-322.

[58]. S. F. Chichibu, T. Onuma, M. Kubota, A. Uedono, T. Sota, A. Tsukazaki, A. Ohtomo, M. Kawasaki, J. Appl. Phys., 99 (2006) 093505.

[59]. S. Dutta, S. Chattophadhyay, M. Sutradhar, A. Sarkar, M. Chakrabarti, D. Sanyal, D. Jana, J. Phys.: Condens. Matter 19 (2007) 236218.

[60]. N. Ohashi, T. Ishigaki, N. Okada, H. Taguchi, I. Sakaguchi, S. Hishita, T. Sekiguchi, H. Haneda, J. Appl. Phys., 93 (2003) 6386.

[61]. L. N. Tong, Y. C. Wang, X. M. He, H. B. Han, A. L. Xia, J. L. Hu, J. Magn. Magn. Mater., 324 (2012) 1795-1799.

[62]. D. Gaspar, L. Pereira, K. Gehrke, B. Galler, E. Fortunato, R. Martins, Sol. Energy

Mater Sol. Cells, 163 (2017) 255-262.

[63]. K. C. Hui, H. C. Ong, P. F. Lee, J. Y. Dai, Appl. Phys. Lett, 86 (2005) 152116.

[64]. S. Dellis, N. Kalfagiannis, S. Kassavetis, C. Bazioti, G.P. Dimitrakopulos, D.C. Koutsogeorgis, P. Patsalas, J. Appl. Phys., 121 (2017) 103014.

[65]. T. C. Chiang, C. Y. Chiu, T. F. Dai, Y. J. Hung, H. C. Hsu, Opt. Mater. Express 7(2017) 313-319.

[66]. D. Thapa, J. Huso, J. L. Morrison, C. D. Corolewski, M. D. McCluskey, L. Bergnam, Optic. Mater, 58 (2016) 382-389.

[67]. Y. I. Alivov, E. V. Kalinina, A. E. Cherenkoe, D.C . Look, B. M. Ataev, B. M. Omaev, A. K. Chukichev, M. Bagnall, Appl. Phys. Lett, 83 (2003) 4719.

[68]. D. K. Hwang, J. H. Lim, S. J. Park, J. Phys. D: Appl. Phys, 40 (2007) R387-R412.

[69]. C. Chen, T. Wang, Y. Xu, Z. Ai, Appl. Phys. Express, 10 (2017) 011202.

[70]. J. Yoo, T. Ahmed, W. Tang, Y. J. Kim, Y. J. Hong, C. H. Lee, G. C. Yi, Nanotechnology, 28 (2017) 394001.

[71]. S. J. Jiao, Z. Z. Zhang, Y. M. Lu, Y. M. Shen, B. Yao, J. Y. Zhang, B. H. Li, D. X. Zhao, X. W. Fan, Z. K. Tang, Appl. Phys. Lett., 88 (2006) 031911.

[72]. C. Cachoncinlle, C. Hebert, J. Perrière, M. Nistor, A. Petit, E. Millon, Appl. Surf. Sci., 336 (2015) 103-107.

[73]. S. F. Yu, C. Yuen, S. P. Lau, H. W. Lee, Appl. Phys. Lett, 84 (2004) 3244.

[74]. J. Dong, D. Han, H. Li, W. Yu, S. Zhang, X. Zhang, Y. Wang, Appl. Surf. Sci., 433 (2018) 836-839.

[75]. K. Kandpal, N. Gupta, Bulletin of Electrical Engineering and Informatics, 5 (2016) 205-212.

[76]. H. Li, D. Han, L. Liu, J. Dong, G. Cui, S. Zhang, X. Zhang, Y. Wang, Nanoscale Res. Lett., 12 (2017) 223.

[77]. P. F. Carcia, R. S. Mclean, M. H. Reilly, Appl. phys. Lett., 88 (2006) 123509.

[78]. I. Noviyana, A. D. Lestari, M. Putri, M. S. Won, J. S. Bae, Y. W. Heo, H. Y. Lee, Materials, 10 (2017) 702.

[79]. Y. Kumaresan, Y. Pak, N. Lim, Y. S. Kim, M. J. Park, S. M. Yoon, H. M. Youn, H. Lee, B. H. Lee, G. Y. Jung, Sci. Rep., 6 (2016) 37764.

[80]. R. A. Afre, N. Sharma, M. Sharon, M. Sharon, Rev.Adv. Mater. Sci. , 53 (2018) 79-89.

[81]. J. -P. Niemelä, B. Macco, L. Barraud, A. Descoeudres, N. Badel, M. Despeisse, G. Christmann, S. Nicolay, C. Ballif, W.M. Kessels, Sol. Energy Mater Sol. Cells, 200

(2019) 109953.

[82]. H. L. Tulzo, N. Schneider, D. Lincot, F. Donsanti, Sol. Energy Mater Sol. Cells, 200 (2019) 109965.

[83]. L. Nulhakim, H. Makino, J. Appl. Phys., 119 (2016) 235302.

[84]. M. Asemi, M. Ahmadi, M. Ghanaatshoar, Ceram.Int., 44 (2018) 12862-12868.

[85]. S. Ghosh, A. Mallick, B. Dou, M. F. A. M. van Hest, S. M. Garner, D. Basak, Sol. Energy, 174 (2018) 815-825.

[86]. H. Agura, A. Suzuki, T. Matsushita, T. Aoki, M. Okuda, Thin solid films, 445 (2003) 263-267.

[87]. R. S. Ajimsha, A. K. Das, P. Misra, M. P. Joshi, L. M. Kukreja, R. Kumar, T. K. Sharma, S. M. Oak, J. Alloy. Comp., 638 (2015) 55-58.

[88]. X. Zeng, X. Wen, X. Sun, W. Liao, Y. Wen, Thin Solid Films, 605 (2016) 257-262.

[89]. V. L. Kuznetsov, A. T. Vai, M. A. Mamouri, J. S. Abell, M. Pepper, P. P. Edwards, Appl. Phys. Lett., 107 (2015) 232103.

[90]. D. B. Potter, M. J. Powell, I. P. Parkin, C. J. Carmalt, J. Mater. Chem. C, 6 (2018) 588-597.

[91]. V. Anand, A. Sakthivelu, K. D. A. Kumar, S. Valanarasu, V. Ganesh, M. Shkir, A. Kathalingam, S. AlFaify, Superlattices Microstruct., 123 (2018) 311-322.

[92]. V. Anand, A. Sakthivelu, K. D. A. Kumar, S. Valanarasu, A. Kathalingam, V. Ganesh, M. Shkir, S. AlFaify, I. Yahia, Ceram. Int., 44 (2018) 6730-6738.

[93]. W. S. Liu, W. T. Hsieh, S. Y. Chen, C. S. Huang, Sol. Energy, 174 (2018) 83-96.

[94]. J. C. Lin, M. C. Huang, T. H. Wang, J. N. Wu, Y. T. Tseng, K. C. Peng, Mater. Express., 5 (2015) 153-158.

[95]. Q. Li, L. Zhu, Y. Li, X. zhang, W. Niu, Y. Guo, Z. Ye, J. Alloy. Comp., 697 (2017) 156-160.

[96]. K. M. Kang, Y. Wang, M. Kim, H. H. Park, Thin Solid Films, 660 (2018) 913-919.

[97]. X. Ji, J. Song, T. Wu, Y. Tian, B. Han, X. Liu, H. Wang, Y. Gui, Y. Ding, Y. Wang, Sol. Materi. Sol. Cells, 190 (2019) 6-11.

[98]. Y. Wang, J. Song, W. Song, Y. Tian, B. Han, X. Meng, F. Yang, Y. Ding, J. Li, Sol. Energy, 186 (2019) 126-135.

[99]. F. H. Wang, H. P. Chang, J. C. Chao, Thin Solid Films, 519 (2011) 5178-5182.

[100]. X. Jiang, F.L. Wong, M.K. Fung, S.T. Lee, Appl. Phys. Lett., 83 (2003) 1875

[101]. E. G. Berasategui, C. Zubizarreta, L. Mendizabal, J. Barriga, A. Vinuales, J.

Palenzuela, Y. Alesanco, B. Herbig, U. Posset, Vacuum, 151 (2018) 108-115.

[102]. D. C. Look, D. C. Reynolds, J. R. Sizelove, R. L. Jones, C. W. Litton, G. Cantwell, W. C. Harsch, Solid State Commun., 105 (1998) 399-401.

[103]. K. Maeda, M. Sato, I. Niikura, T. Fukuda, Semicond. Sci. Technol, 20 (2005) S49.

[104]. H. B. Kang, K. Nakamura, K. Yoshida, K. Ishikawa, Jpn. J. Appl. Phys., 36 (1997) L933-L935.

[105]. Y. Kozuka, A. Tsukazaki, M. Kawasaki, Appl. Phys. Rev., 1 (2014) 011303.

[106]. H. Tong, Z. Deng, Z. Liu, C. Huang, J. Huang, H. Lan, C. Wang, Y. Cao, Appl. Surf. Sci., 257 (2011) 4906-4911.

[107]. T. Koida, T. Kaneko, H. Shibata, Materials, 10 (2017) 141.

[108]. T. Dimopoulos, G. Z. Radnoczi, Z. E. Horváth, H. Brückl, Thin Solid Films, 520 (2012) 5222-5226.

[109]. W. Wang, Z. Wu, Z. Liu, A. Pang, Y. L. Tu, Z. C. Feng, Thin Solid Films, 519 (2010) 31-36.

[110]. J. Montero, C. Guillén, J. Herrero, Thin Solid Films, 519 (2011) 7564-7567.

[111]. I. H. Kim, D. Y. Ku, J. H. Ko, D. Kim, K. S. Lee, J. -H. Jeong, T. S. Lee, B. Cheong, Y. -J. Baik, W. M. Kim, J Electroceram, 17 (2006) 241-245.

[112]. R. F. Allah, T. Ben, D. González, V. Hortelano, O. Martínez, J. L. Plaza, Nanoscale Res. Lett., 8 (2013) 162.

[113]. J. -S. Park, J. K. Jeong, Y. -G. Mo, H. D. Kim, S. -I. Kim, Appl. Phys. Lett., 90 (2007) 262106.

[114]. J. S. Kim, M. K. Joo, M. X. Piao, S. E. Ahn, Y. H. Choi, H. K. Jang, G. T. Kim, J. Appl. Phys., 115 (2014) 114503.

[115]. K. Remashan, D. K. Hwang, S. D. Park, J. W. Bae, G. Y. Yeom, S. J. Park, J. H. Jang, Electrochem. Solid-State Lett., 11 (2008) H55-H59.

Chapter 2. Fabrication and Characterization methods

2.1. Magnetron sputtering

ZnO thin films can be deposited using a variety of methods, both chemical and physical depositions. The ZnO films deposited by physical methods including magnetron sputtering (MS), pulsed laser deposition and molecular beam expitaxy mostly exhibited better opto-electrical properties with better crystallinity compared to chemical methods. Nowadays, MS are scaled up for industrial deposition. This is a plasma vapor deposition process in which plasma state is created and positive charged ions are accelerated by an electrical field to the cathode. A target containing source materials is placed on the cathode. The bombardment of positive charged ions with high kinetic energy on the surface of target can dislodge and sputter atoms from the target. The sputtered atoms will condense on all the surfaces inside the chamber, including substrate. Before deposition, the deposition chamber needs to be evacuated to a vacuum level of $10^{-4} – 10^{-5}$ Pa to avoid the contamination from residual gas. The working gas (normally inert gas, Ar), sometime including forming gases such as O_2, N_2, H_2, H_2O vapor, F_2, etc.[1-5], which depend on the purpose, will be introduced during deposition process. The pressure should be in order of ~ 1 Pa, which is not to low and not too high, to maintain the discharge. In MS, a magnetic field was applied at the cathode to trap electrons, enhancing the efficiency of ionization and erosion rate. Compared to other deposition methods, MS has advantages of high deposition rate, large scale uniformity, good structural films and high reproducibility. It allows films to be deposited at low temperature, and in forming gas. Therefore, it is one of the most used methods for ZnO thin film fabrication.

The working principle of a magnetron sputtering can be illustrated in Fig. 2.1. After evacuation of the chamber and introducing working gas, firstly a high voltage of ~ kV is applied between anode and cathode to ignite the glow discharge. Then the positive ions are accelerated to the cathode and eject target atoms. Secondary electrons, created from bombardment and collisions between ions and target atoms, are accelerated away from cathode, collide with gas atoms and ionize them, thereby sustaining the discharge. The power supply is controlled after plasma ignition. A magnet is engaged under the target to create a magnetic field oriented radially and directly above the target surface. The electromagnetic field drifts ions and electrons in a circular path along the target surface, thereby resulting in a high plasma density region and then enhancing the efficiency of sputtering process. The bombardment of the ions causes a heating of the target. Therefore, cooling system, which normally circulated cooling water, needs to be included. The substrate is located on the chamber wall as a part of anode, facing to the cathode, and can be connected with a heater which allows deposition at high temperature. The deposition at high temperature normally resulted in better crystalline film [6], owing to higher energy of atoms which benefit for atom migration and arrangement.

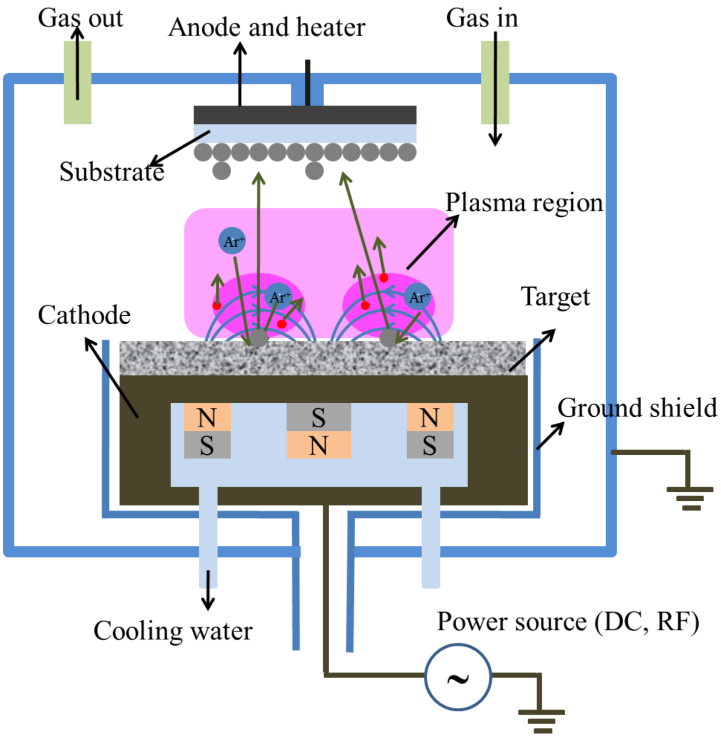

Fig. 2. 1. Schematic view of a magnetron sputtering.

There are three types of power source in MS, direct-current (DC), radio frequency (RF) and RF superimposed DC. DC MS is only used for deposition of conductive materials. This have high deposition rate but high voltage may increase damages on film. RF MS with moderate ions energy results in film with better crystallinity, but lower deposition rate compared to DC MS. Using of superimposed DC and RF MS can help to improve both film crystallinity and deposition rate [7]. The film growth can be controlled by varying the supply power, gas ambience, working pressure and substrate temperatures. Due to high reproducibility, thickness of the film can be controlled through the deposition time with a given deposition rate.

2.2. Plasma treatment

Plasma treatment is a well-known method used to clean and modify the surface properties of samples put inside the plasma ambience. The creation of plasma and its usage are similar with the description in the section 2.1. The samples are placed near or on the cathode, and the ions created from the gas will be accelerated to hit the surface of the sample. Thereby, the weakly bond atoms or molecules on the surface will be knock out. The effect of plasma was widely ascribed to this bombardment. In reactive plasma treatment, active gases (like O_2, N_2, CH_4, ect.) are introduced together with the inert gas, to create the high energy active gas atoms to modify the surface chemical bonding. High kinetic energy ions from plasma ambience may also implant into sample and thereby modulating the properties of the samples, as in our studies.

2.3. Hall effect measurement – electrical characterization

Hall effect measurement is a well-known technique used to characterize the electrical properties of semiconductor. This technique, based on Hall effects, allows us to extract the concentration of major charge carrier, and their mobility. Hall effect can be observed when a magnetic field is applied perpendicular to an electric current, which applied along the conductive sample. Due to Lorentz force, charge carriers are pushed to one side of the sample. The accumulation of charges at the side of the sample caused a voltage between two sides and the transverse electric field acts on the charge carriers in opposite direction with force of the magnetic field. These two forces are balance at a steady state because no current flows in this direction. The induced voltage between two sides of the sample is called Hall voltage, this is proportional to the carrier concentration. The Hall effect can be illustrated in the Fig. 2.2.

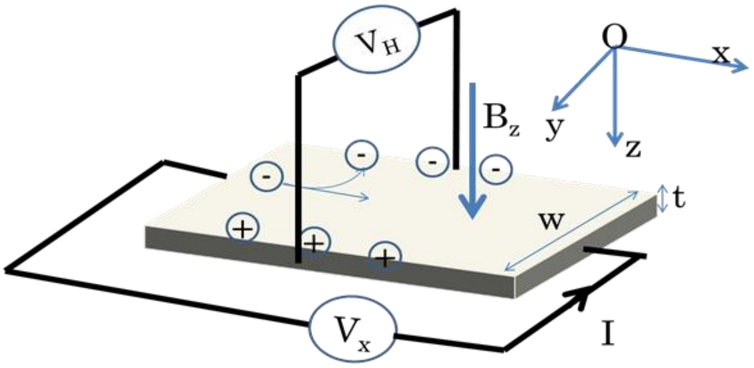

Fig. 2. 2. Schematic of Hall effect.

Applying current I, charge q moves in the x direction with velocity $\overrightarrow{v_x}$. The accumulation of charges at the sides of sample caused an electric field $\overrightarrow{E_y}$. In steady state, the total force acting on the charge in y direction must be rezo.

$$\vec{F} = q(\overrightarrow{E_y} + \overrightarrow{v_x} \times \overrightarrow{B_z}) = 0 \tag{2.1}$$

Or on y direction,

$$q\ (E_y - v_x B_z) = 0 \tag{2.2}$$

Therefore,

$$E_y = v_x B_z = \frac{V_H}{w} \tag{2.3}$$

From the current $I_x = v_x qnwt$, we have

$$v_x = \frac{I_x}{qnwt} \tag{2.4}$$

$$\text{So, } \frac{V_H}{w} = \frac{I_x B_z}{qnwt} \text{ and } V_H = \frac{I_x B_z}{qnt} \tag{2.5}$$

The Hall coefficient is defined as

$$R_H = \frac{V_H t}{I_x B_z} = \frac{1}{qn} \tag{2.6}$$

where, q is carrier charge, n is charge carrier concentration, t is the thickness and w is the width of the sample, I_x, B_z, E_y, V_H are current in x direction, magnetic field in z direction, induced electric field and Hall voltage in y direction, respectively.

The Hall coefficient R_H give information on the major charge carrier, it is negative if the charge carriers are electrons, positive if the charge carriers are holes.

To investigate electrical properties of a thin film, Hall effects is measured with van der Pauw configuration for resistivity measurement. The current is applied and Hall voltage is measured through four small contacts on the circumference of a uniform sample. The common configuration is contacts on four corners of a square sample (Fig. 2.3).

The sheet resistance of the sample can be derived from eight measurements on the four electrodes, without applying magnetic field as follows [8]:

$$R_{Sh} = \frac{1}{8}\frac{\pi}{\ln(2)}\left[f_A\left(\frac{V_{34}}{I_{12}} - \frac{V_{34}}{I_{21}} + \frac{V_{41}}{I_{23}} - \frac{V_{41}}{I_{32}}\right) + f_B\left(\frac{V_{12}}{I_{34}} - \frac{V_{12}}{I_{43}} + \frac{V_{23}}{I_{41}} - \frac{V_{23}}{I_{14}}\right)\right] \quad (2.7)$$

where f_A, f_B are geometrical symmetry, they are related to two resistance ratios Q_A and Q_B, according to this equation:

$$\frac{Q-1}{Q+1} = \frac{f}{\ln(2)} arc \; cosh\left(\frac{1}{2} exp\left(\frac{\ln(2)}{f}\right)\right) \quad (2.8)$$

where,

$$Q_A = \frac{\frac{V_{34}}{I_{12}} - \frac{V_{34}}{I_{21}}}{\frac{V_{41}}{I_{23}} - \frac{V_{41}}{I_{32}}} \quad \text{and} \quad Q_B = \frac{\frac{V_{12}}{I_{34}} - \frac{V_{12}}{I_{43}}}{\frac{V_{23}}{I_{41}} - \frac{V_{23}}{I_{14}}} \quad (2.9)$$

For sample with perfect symmetry, $f_A = f_B = 1$

The resistivity of the sample is calculated by: $\rho = R_{sh}t$, with *t* is the thickness of the sample.

The Hall coefficient is calculated by using the average of measured Hall voltages with opposite magnetic fields and currents, as following:

$$R_H = \frac{t}{IB}\frac{1}{8}\big(V_{24}(B_+I_+) + V_{24}(B_+I_-) - V_{24}(B_-I_+) - V_{24}(B_-I_-) + V_{13}(B_+I_+) + V_{13}(B_+I_-) - V_{13}(B_-I_+) - V_{13}(B_-I_-)\big) \quad (2.10)$$

where $B_{+,-}$ and $I_{+,-}$ imply the directions of the magnetic field and applied current.

The carrier concentration is calculated through the *R_H*, according to equation:

$$n = \frac{1}{qR_H} \tag{2.11}$$

And Hall mobility can be derived as:

$$\mu_{Hall} = \frac{1}{nq\rho} \tag{2.12}$$

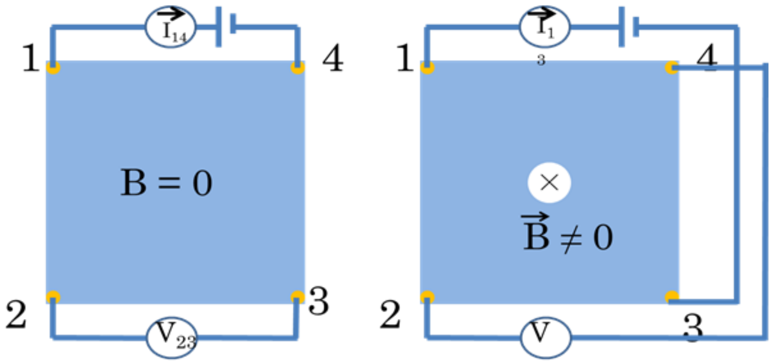

Fig. 2. 3. Hall effect measurement with Van der Pauw configuration for electrical properties characterization of thin film.

In our study, electrical properties were characterized using HL5500PC Hall Effect Measurement System with HL5580 Buffer Amplifier. The magnetic field is 0.505 T.

2.4. Optical spectroscopy

Optical properties of the sample including transmission and reflection spectra were characterized using a Hitachi U-4100 spectrophotometer, in the wavelength range of 200-2500 nm. The spectrophotometer consists of a light source, spectroscope, mirrors and sample cell, and light detector. For the range from UV to NIR, the light source contains two lamps, a deuterium for light emissions in the ultraviolet range and a tungsten halogen lamp for light emissions in the visible and near-infrared ranges. The spectroscope is used to produce the monochromatic light, it can be light filter, prism or diffraction grating. In Hitachi U-4100, diffraction gratings are used. The lens and mirror set are used to focus and direct light beam for transmission or reflection measurement. The light detector consists of a photomultiplier for UV-Vis light and a cooled PbS photoconductive detector for NIR light.

In our study, the transmission and reflection spectra of ZnO thin films were measured with an angle of incident light of 5°. Due to small angle, the reflectance does not change significantly compared to reflectance at 0°. Before measurement, a base line was taken in transmission configuration without sample. The configurations for optical measurements are presented in Fig. 2.4. The transmittance and reflection are determined by $T(\lambda) = I_T(\lambda)/I_0(\lambda)$ and $R(\lambda) = I_R(\lambda)/I_0(\lambda)$, where T(λ) and $R(\lambda)$ are transmittance and reflectance at wavelength λ, respectively. $I_T(\lambda)$, $I_R(\lambda)$ and $I_0(\lambda)$ are intensities of transmitted, reflected and incident lights at wavelength λ, respectively.

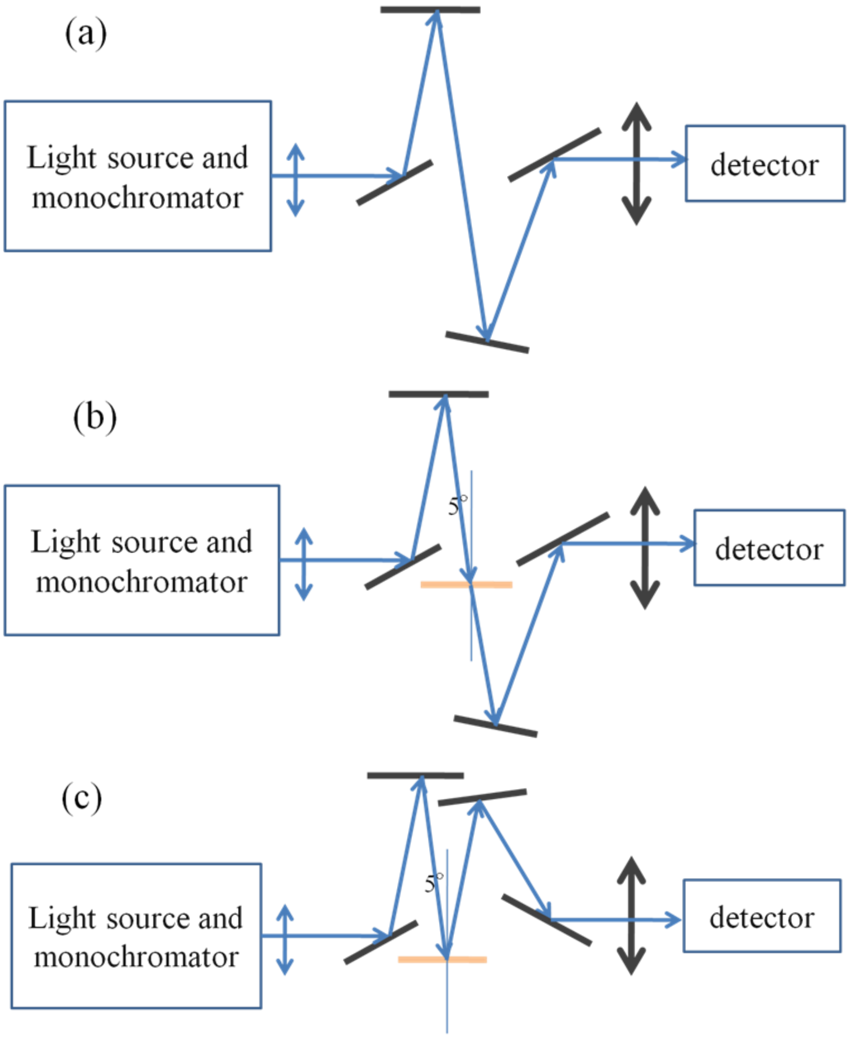

Fig. 2. 4. Schematic view of optical characterization using photospectrometer: baseline (a), transmission (b), and reflection (c) measurements.

The absorption spectra, can be extracted from the transmission and reflection spectra, as follow:

$$A(\lambda) = 1 - T(\lambda) - R(\lambda) \tag{2.13}$$

where $A(\lambda)$ is the absorbance of sample at light wavelength λ.

The absorption coefficient, can be calculated from the transmittance and reflectance.

Assuming that $\cos(5°) \approx \cos(0°) = 1$, and there is no effect of glass substrate on the transmittance spectra, due to the refractive index of glass is quite similar to the refractive index of ZnO, according to Beer-Lambert law, we have:

$$I_0 T = I_0(1 - R)\exp(-\alpha t) \tag{2.16}$$

where α is absorption coefficient, t is the thickness of the film.

So, the absorption spectra can be calculated as:

$$\alpha = \frac{1}{t}\ln\left(\frac{1-R}{T}\right) \tag{2.15}$$

2.5. Photoluminescence spectroscopy

2.5.1. Photoluminescence

Photoluminescence is an optically radiative relaxation process occurs after a material is excited by photon energy. When material is illuminated by an excitation light with photon energy equal or higher the energy gap, electrons at the ground states in valence band absorb photons energy and are excited to a higher energy levels, the excited states, usually in conduction band, and leave holes in valence band. The excited states are not stable, excited electrons relax back to its ground states and recombine with holes. The relaxation of excited electrons can be non-radiative transitions through vibration, or radiative transitions. The radiative transitions releases energy in form of photon energy and called photoluminescence. This process normally occurs between conduction band and valence band of a semiconductor. A basic illustration of photoluminescence process is shown in Fig. 2.5**.** This also possibly occurs between energy band and impurity states or between impurities state themselves (donor –

acceptor pair). There are several basic radiative transitions [9], including:

- Band to band transition: is the radiative recombination between free-electrons in conduction band and holes in valence band, occurs in direct band gap materials.
- Free-exciton transition: Due to Coulomb attraction between negative electrons and positive holes, electrons can orbit about the holes as if they were H like atoms. The binding energy of an exciton is $E_{xn} = \frac{m_r^* e^4}{2h\varepsilon^2}\frac{1}{n^2}$, where m_r^* is reduced mass of e-h pair, h is Plank constant, ε is dielectric constant, and n is exciton state (quantum number). When e-h pairs in excitons recombine, the emitted phonon energy is simply given by:

$$h\nu = E_g - E_{xn} \tag{2.16}$$

- Phonon-assisted recombination: Due to coupling of excitons with photons (polaritons), and coupling of excitons with phonons, the recombination of excitons may occur with emission of phonons, especially longitudinal optical (LO) phonons. Therefore, the emission energy is lower than free-excitonic emission energy, with the different energy equal to LO – phonon energy, and a low energy tail of emission peak appears due to polariton emission [9, 10].
- Bound excitons transitions: Due to Colomb interaction, excitons can be bound with other excitons or one electron can be bound with more than one hole and vice versa, causing the lowering of excitonic energy. In the presence of impurity, excitons are also bound with donor states or acceptor states. These recombination of these bound excitons lead to emissions at lower energy compared to free-exciton emission.
- Transitions between band and impurities state – deep level emission: When the impurities states appear deep inside the band gap, the transition between deep level defects and intrinsic band energy can occur. In excited state, e in the conduction band can relax to the deep acceptor level and electron of donor can combine with the hole in valence band. These processes leading to the emissions with significantly lower energy

compared to band-edge emission.

- Transistion between donor-acceptor pairs: Under optical pumping, electrons and holes are created and may bound with ionized donor (D^+) and ionized acceptor (A^-), to neutralize donor and acceptor centers. These states of donors and acceptors can promote the recombination of e in donors with h in acceptors, irradiate photons ($D_0 + A_0 \rightarrow h\nu + D^+ + A^-$).

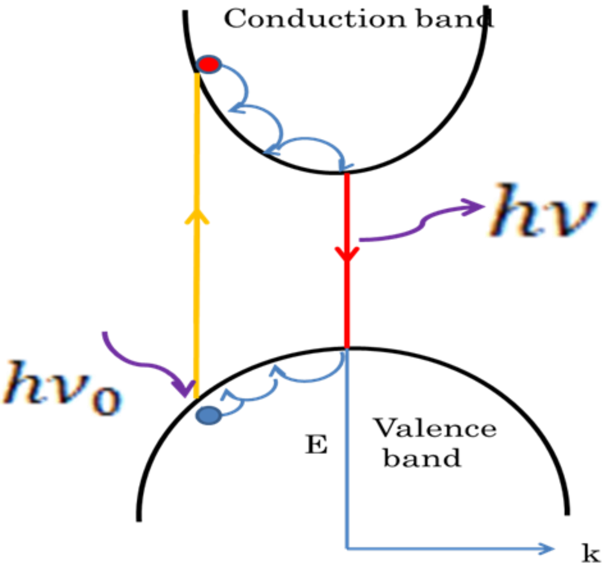

Fig. 2. 5. A schematic of excitation and photoluminescence processes.

Beside radiative transitions which give emission in photoluminescence spectra, there exist several types of non-radiative transitions, for instance, via phonon emission, recombination at surface defects, dislocations, etc. The studies on the non-radiative defects are now still controversial, but obviously, they reduce the photoluminescence yield. Study of photoluminescence can help to investigate the defect states in the material.

2.5.2. Photoluminescence spectroscopy

The photoluminescence spectroscopy consists of a laser source, optics for light grating, collimation and focusing, and the spectrometer. The spectrometer includes a monochromator and a photodetector. Our study employed a spectrometer of Princeton Instruments, SP-2500, which is equipped with a charge coupled device detector (CCD) (PIXIS 256E). The CCD resolution is 0.09 nm and the grating accuracy is 0.2 nm [11]. A He-Cd laser (λ = 325 nm) was used as excitation source. A band pass filter ($\lambda > 480$ nm) was place before the detector to cut off the stray light of laser when measuring the photoluminescence in Vis and NIR range. A focal lens was used to focus laser on to the sample surface. The slit size is controlled in the range of 0.1 – 0.25 mm depends on the photoluminescence intensity. If slit is too narrow, the noise/signal ratio will increase. If the slit is too wide, the resolution of spectra will be decreased. The basic optics arrangement for this measurement is presented in Fig. 2.6. The photoluminescence of our samples was measured at room temperature. For PL at low temperature, cryogenic equipment needs to be used, but it is out of our scope.

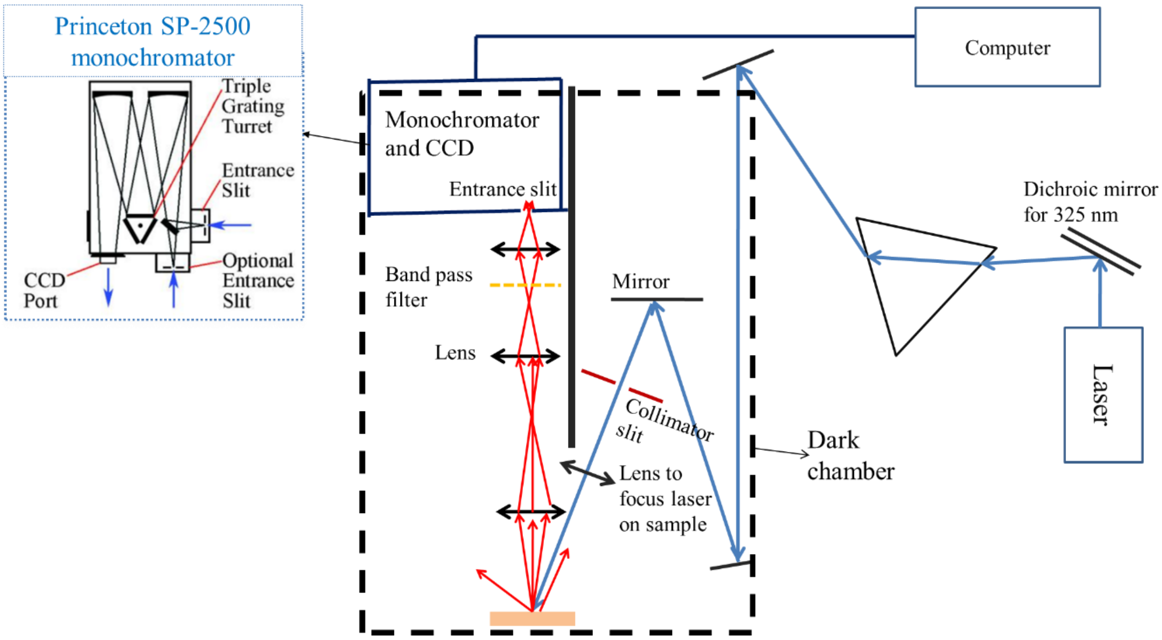

Fig. 2. 6. Illustration of a photoluminescence spectroscopy – optics arrangement.

2.6. X-ray diffraction

X-ray diffraction is a powerful technique used to characterize the crystal structure of the materials, in which the formation of structure phase, grain size, dominated orientation of crystal domains and the alignment quality, microstrain can be estimated. The basic principle of X-ray diffraction on a crystal structure can be illustrated in Fig. 2.7.

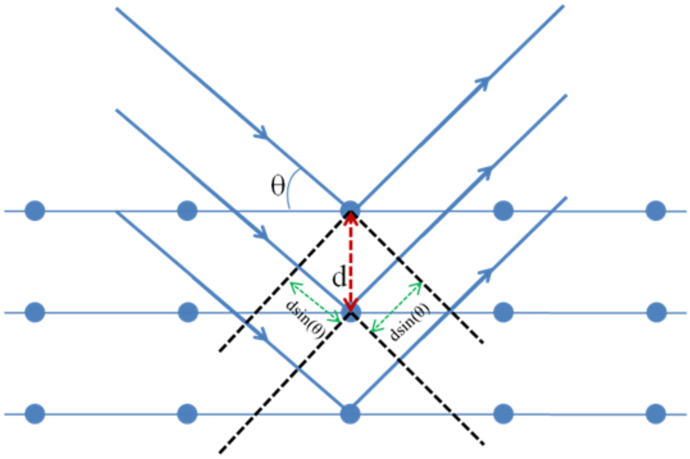

Fig. 2. 7. Principle of X-ray diffraction.

When X-rays were irradiated onto a crystal lattice with regularly periodic arrangement of atoms, X-rays were reflected in the same direction from parallel atomic planes and interfere together. The reflected waves from the periodically arranged atoms on two adjacent planes have a path length difference of $\Delta l = 2dsin(\theta)$. If the path difference is equal to an integer number of wavelength, the waves have the same phase and their interference is constructive, giving a diffraction peak. The condition for constructive interference, known as Bragg's law, is given by:

$$\Delta l = 2dsin(\theta) = \ n\lambda \tag{2.17}$$

Accordingly, if X-rays strike on the multiple planes of atoms with high periodicity, at a given diffraction angle corresponding to their interplanar distance, the diffraction intensity will be built up and strong. Better crystallinity, as well as longer range of periodicity (larger crystal domains) will result in stronger and narrower diffraction peaks. If the periodicity of atoms is bad (small grains, dislocations, stacking faults, point defects), the diffraction peaks are low, and broad. In amorphous sample, no diffraction peak can be observed.

There are several XRD measurements such as out-of plane (2θ-ω), in-plane (2θχ-φ), rocking curve (ω scan), and pole. In our study, we employed out-of-plane, in-plane and rocking curve measurement to investigate the crystalline structure, and the alignment of crystalline domains in ZnO thin films.

Out-of-plane XRD is diffraction method that collects the diffracted X-rays from the crystal lattice planes that are parallel to the sample surface. This method was used widely to investigate the crystal structure of samples. The geometry for out-of-plane diffraction is illustrated in Fig. 2.8 (a). The X-rays is irradiated to the sample under the incident angle of θ (sometime called ω) with respect to sample surface, where the detector will move at the angle of 2θ with respect to the direction of incident X-rays.

The degree of alignment of crystal domains strongly affect to the properties of materials. While the out of plane measurement are symmetrical reflection, giving information on crystalline structure with preferred orientation, the degree of the orientation can be determined using rocking-curve measurement. In this method, the detector is kept at a fixed 2θ angle at which the diffraction peak of preferred orientation was obtained while incident angle ω is varied. The tilting of the crystalline domains along the preferred orientation can be estimated from the full width at half maximum of the rocking curve. The rocking-curve can also be measured by fixing incident angle at ω and scan 2θ. The geometry for rocking curve is presented in Fig. 2.8 (b).

In-plane XRD is the technique used to measuring the diffraction from lattice planes which are normal to the sample surface. The sample and the detector are rotated in the angles of φ and 2θχ, respectively, in the plane parallel to sample surface. Its geometry is shown in Fig. 2.8 (c). In-plane XRD allows for structure depth-analysis by varying the incident angle ω (angle between incident X-rays with sample surface).

In our study, Cu anode was used as X-rays source. Before arriving on the sample, X - rays beam was monochromized by a parallel beam graded multilayer X-ray monochromator and collimated by slits to obtain parallel Cu Kα (λ = 1.5418 Å) X-rays beam. For in-plane measurement, a soller slit should be used to decrease the vertical divergence of X-rays beam.

The reflected X-rays are collimated before reaching to the detector. Ni filter is used to cut off Cu Kβ rays.

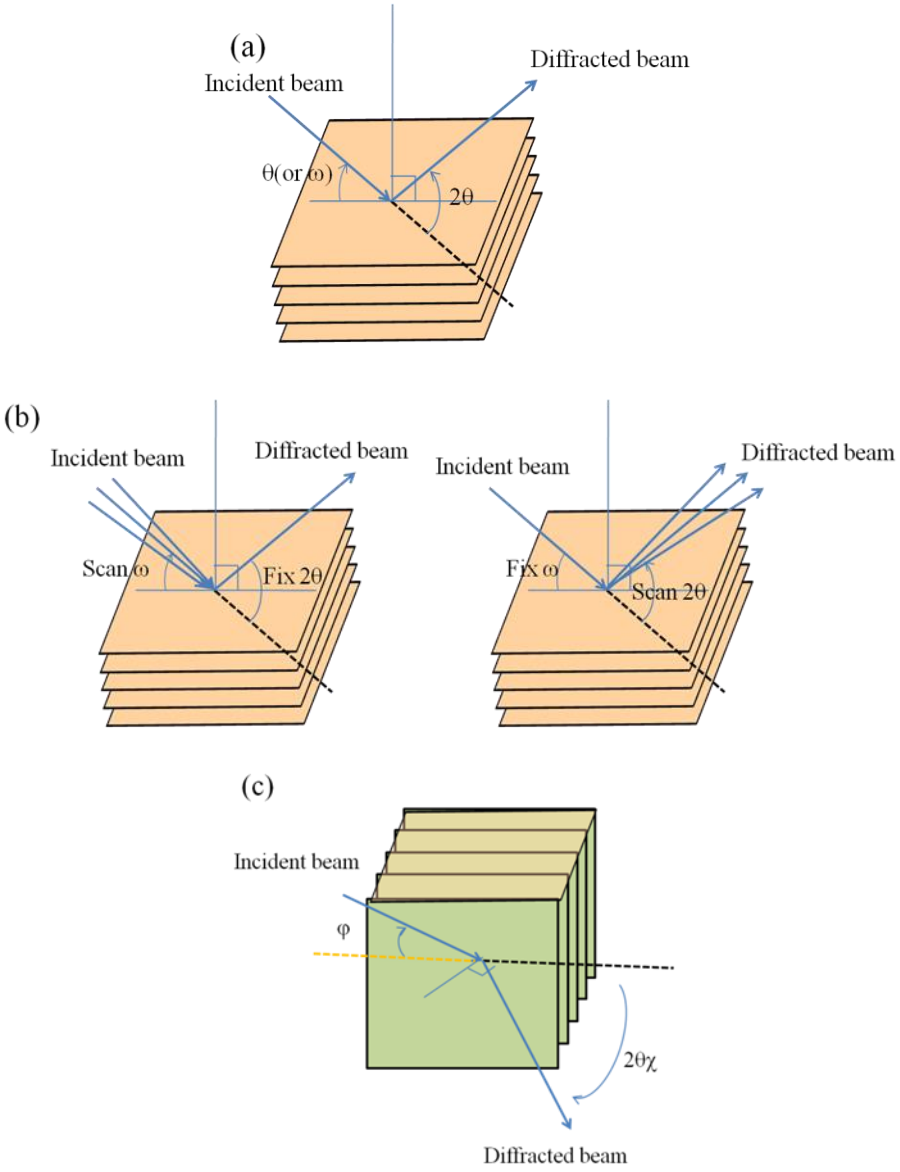

Fig. 2. 8. Geometries of out-of-plane (a), rocking-curve (b) and in-plane (c) XRD measurements.

2.7. X-ray photoelectron spectroscopy

X-ray photoelectron spectroscopy (XPS) is a technique used to investigate the surface and near surface chemistry, including elemental composition, chemical states, and electronic states of elements within a material. This method was established based on the photoelectric effect. When a beam of X-rays was irradiated on the sample surface, electrons can absorb energy of X-rays. If the acquired energy is sufficient, electrons will be ejected from atoms. A schematic view of this effect is shown in Fig. 2.9. The XPS spectra are obtained by irradiating X-rays beam on material surface while simultaneously measuring the kinetic energy of emitted electrons. The kinetic energy of electron is given by [12]:

$$E_{KE} = h\nu - \ E_B - \phi \tag{2. 18}$$

where E_{KE} is kinetic energy of emitted electron, $h\nu$ is phonon energy of X-ray, E_B is binding energy of electron in atom, with respect to Fermi energy level, and ϕ is work function of material.

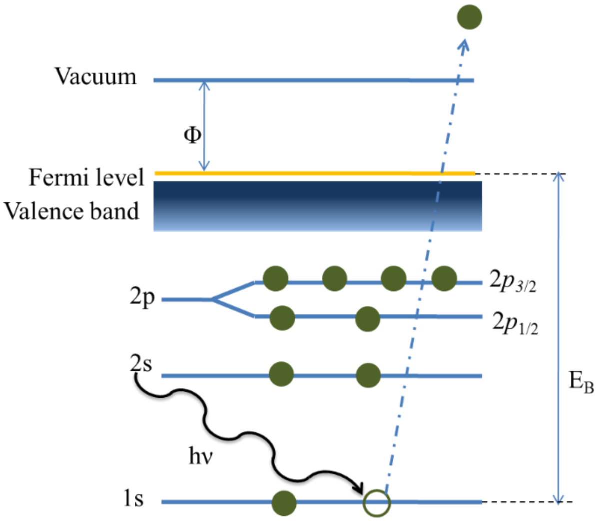

Fig. 2. 9. Illustration of photoemission process.

Binding energy of electron describes the bonding energy of electrons with atoms inside material. Electrons are bound to atoms through the electromagnetic force between them and nuclei. Therefore, the electron binding energy depends on: (1) the atomic number of element (number of protons in the nucleus), (2) the distance between core electrons and their nuclei (electron structure – the electron orbital), (3) the density of neighbouring electrons (chemical bonding states), (4) electron-electron interactions (repelling and shielding from attraction force of nuclei). Consequently, XPS spectra reflect the elemental composition and their chemical bonding states.

An XPS normally consists of X-ray sources (monochromated source), extraction optics and energy filter (energy analyzer), and a detector. The measurement needs to be operated in high vacuum chamber (~10^{-7} - 10^{-8} Pa), to acquire effectively and precisely kinetic energy of electrons (owing to less collisions), as well as to avoid other effects (gas adsorption, gas ionization).

Our studies employed a custom-made XPS system equipped with two monochromatic X-rays sources, an Al Kα (photon energy of 1486.6 eV) source and a Cr Kα (photon energy of 5414.9 eV) X-ray source (ULVAC-PHI), and a wide acceptance angle electron analyzer (Scienta Omicron, EW4000). During XPS measurements, charging on the surface was neutralized simultaneously by irradiation of a low-energy electron beam and a low-energy Ar ion beam (ULVAC-PHI). While the measurement with Al Kα X-rays source is surface sensitive, the measurement using Cr Kα X-rays source reflects information from deeper part beneath the surface, owing to higher kinetic energy of electrons.

2.8. Thermal desorption spectroscopy

Thermal desorption spectroscopy (TDS) is technique used to monitor desorption kinetic of chemical species from the solid surface under heating. The partial pressures of desorbed atoms and molecules are measured while controlling heating rate. This process needs to be performed in a continuously pumped ultrahigh vacuum chamber. When the pumping speed is sufficiently large compared to the pressure change in the chamber caused by desorbed gas, the change in partial pressure of the desorbed gas component is proportional to the desorption rate. The partial pressure of gas is monitored using a mass spectrometer. In mass spectrometer, the desorbed gases are ionized by accelerated electrons emitted from a filament of the mass spectrometer, and then are separated according to their specific mass-to charge ratio when they pass through the analyser in mass spectrometer and are detected and recorded by an ions detector. The ion currents is proportional to the partial pressures, or in other words, it is proportional to the desorption rates of specific species [13]. A schematic view of TDS can be found in Fig. 2.10.

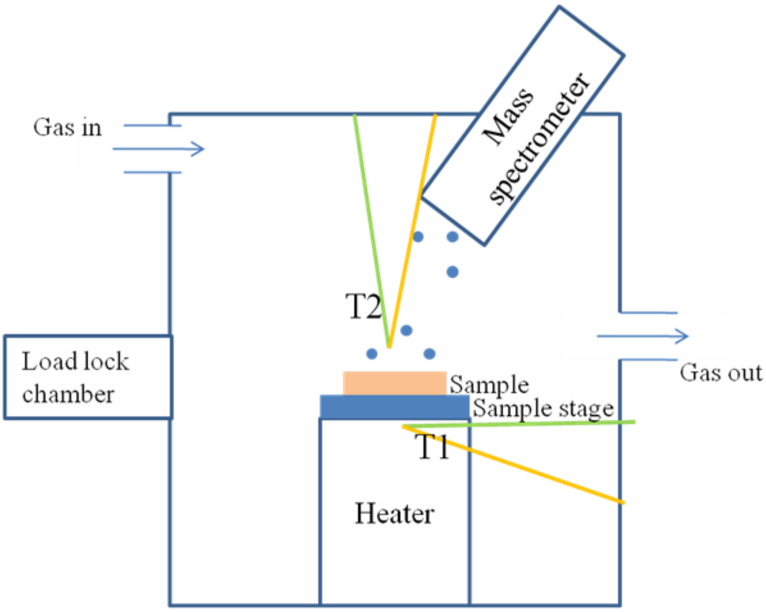

Fig. 2. 10. Schematic view of a TDS.

Our studies were performed with Esco TDS 1200 II which is equipped with a quadrupole mass spectrometer. The working chamber was vacuumed to below 5×10^{-7} Pa before starting heating. The heating was monitored and controlled using a thermocouple under the sample stage. For sample grown on glass substrate, a SiC sample stage was utilized to assure the heating. The temperature on the surface of sample can be monitored using a thermocouple. For our studies, a heating rate of 20 °C/min was used.

2.9. Secondary ion mass spectroscopy

Secondary ion mass spectroscopy (SIMS) is a technique used to investigate the surface composition of a material, based on the emission of secondary ions ejected from a sample surface when bombarded by a primary ion beam of heavy particles, with energy of several keV [14]. The secondary ions ejected from sample surface will be focused into entrance slit of a spectrometer and then separated and detected using mass spectrometer. This technique should be used in a high vacuum chamber. An illustration for SIMS is presented in Fig. 2.11. For depth profiling, which presents the variation of composition with depth below the surface, dynamic

SIMS with constant ion beam bombardment rate (sputtering rate) is used. The secondary ions are recorded during continuous bombardment. The depth was calculated using sputtering rate. In this thesis, the SIMS measurement was performed using a PHI ADEPT 1010 with Cs^+ irradiation and acceleration voltage of 5.0 kV.

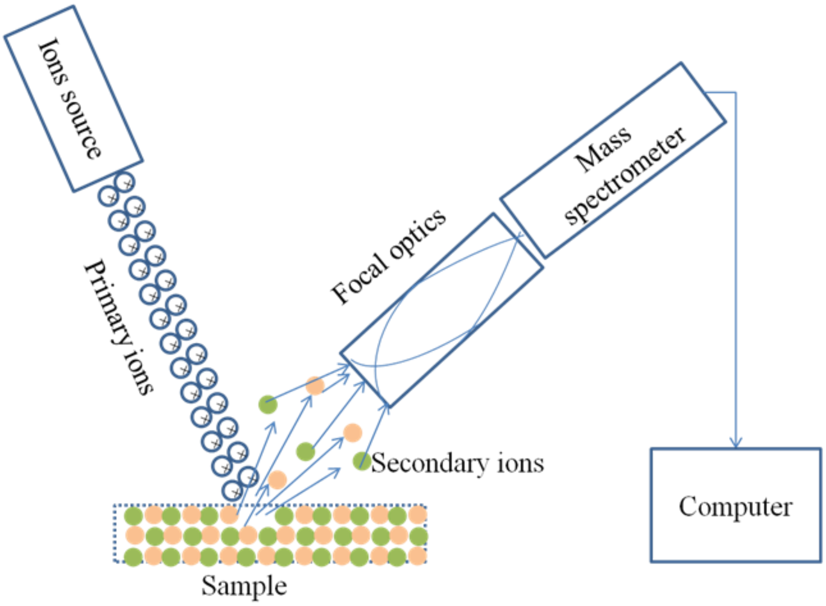

Fig. 2. 11. Illustration of SIMS measurement.

2.10. Surface morphology characterization – atomic force microscopy (AFM) and fied emission scanning electron microscopy (FE-SEM)

2.10.1. AFM

AFM is a scanning microscope which reflects the topographical image of the sample surface based on the atomic interactions between atoms of the tip and atoms on sample surface at a very short distance. The tip is supported by a flexible cantilever which has low spring constant, allowing the cantilever to bend with small force. A laser beam is bounced off the back of cantilever and reflects the change in cantilever position onto a position sensitive photodiode detector. This deflection of the cantilever is proportional to the force acting on the tip, described by Hook’s law. The deflection of the cantilever is then magnified and transferred into a feedback loop, to control the Z scanner movement (height) or control the oscillation of cantilever. The working principle of an AFM can be illustrated in Fig. 2.12.

There are two modes of AFM, they are contact and non-contact modes [15]. In contact mode, the deflection of cantilever is used to control the Z scale of the scanner, or in other words, to control distance between tip and sample surface, to keep the deflection of cantilever constant. The surface topography is mapped by Z scanner movement, while scanning X, Y. Another way to map the surface topography in contact mode is using directly the deflection of cantilever without controlling the Z scanner. The contact mode is sensitive to the depth, but it is strongly influenced by surface adsorbates, lateral force (forces from adjacent area) and fiction force. The lateral resolution of this mode is not very high. To overcome the lateral and fiction forces, and reduce strong damages of tip and sample surface, non-contact mode is used. This mode operates in the attractive force regime with the distance between tip and sample is higher than in contact mode (using repulsive force regime). The cantilever is oscillated at or near its resonance frequency and the change in its oscillation (both in amplitude and frequency) is monitored, depending on the tip-sample interaction. There are two ways to monitor changes, one is using amplitude of oscillation as the feedback signal (AM mode), the other is using oscillation frequency as the feedback signal (FM mode). The feedback loops then control the Z scanner to maintain the distance between tip-sample and the movement of the Z scanner is monitored as surface morphology. To operate in this mode, the response of Z scanner needs to be fast enough to track the changes to prevent the tip from contacting to the sample surface. The tapping mode is employed to overcome this difficulty. In this mode, the cantilever is oscillated with large vibration amplitude, the tip strikes at and detaches from the sample surface in each cycle of vibration. Therefore, this method enhances the lateral resolution of the image and reduces the damage of the tip and sample. It can work in the range between repulsive and attractive regime (Fig. 2.13).

In this thesis, a scanning probe microscopy (JEOL) was used to map the surface morphology of our sample, using non-contact AFM mode.

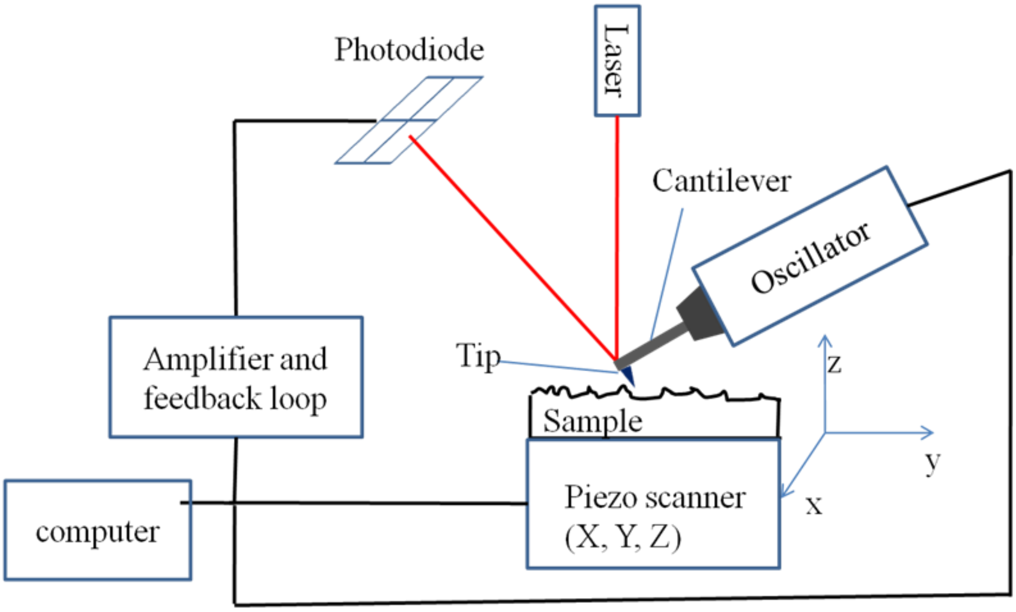

Fig. 2. 12. Working principle of AFM.

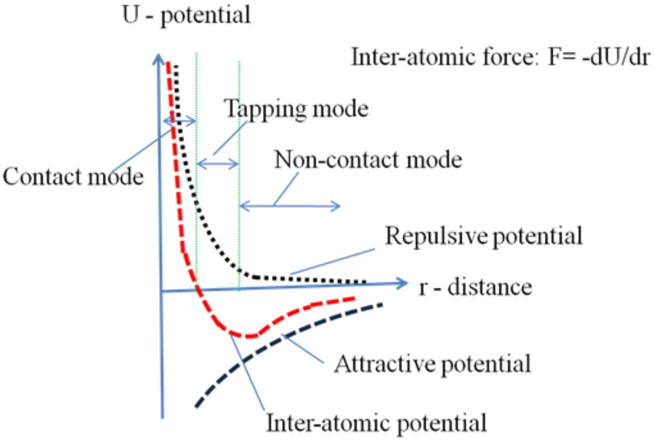

Fig. 2. 13. Diagram of **i**nter-atomic potential as a function of inter-atomic distance and the working regions for AFM modes.

2.10.2. FE-SEM

Scanning electron microscopy (SEM) is an electron microscope used to produce surface topography of sample by scanning an electron beam on the surface of sample. The electrons interact with atoms in the sample and eject secondary electrons out of atoms in the specimen. The secondary electrons are detected by electron detector. The signal intensity is proportional to the number of detected secondary electrons which is depends on specimen topography. The secondary electrons have small energy, therefore, those generated at a deep region under the surface is quickly reabsorbed by the specimen and can not escape out. Moreover, when the electron beam is irradiated perpendicular to the sample surface, the number of scattered electrons from the inclined part is larger than number of scattered electrons from flat part. Therefore, the secondary electrons are very sensitive to the surface topography. Combining with the scanning of the electron beam, the signal of secondary electrons construct the surface topography of sample. In additions to the secondary electrons, there are backscattered electrons which are incident electrons scattered backward. They have high energy, thus they can reflect information from a relatively deep region. They are also sensitive to the composition of the specimen, as well as crystal orientation.

An SEM basically consists of an electron gun, electron optics (condenser lens, objective lens aperture, objective lens, scan coils and stigmator coils), sample stage and electron detector [16]. The electron gun is used to produce an electron beam. For FE-SEM, electron gun is field emission gun, which consists of a metal needle (normally is single crystal tungsten tip) as a emitter, and two anodes, one biased at few kV for electron emission, and the other anode for accelerating electrons. An electro-magnetic condenser lens and an objective aperture are used to control the electron beam diameter and beam current. The objective lens was place before sample stage to focus electron beam on the sample surface. The scan coils are used to move electron beam for scanning process. The stigmator coils are used to correct the irregularities in x, y deflection of electron beam, in order to obtain perfectly round-shaped electron beam. The sample stage can tilt, rotate, and move in horizontal direction (X, Y) for area selection or vertical direction (Z) for change the depth of focus and image resolution. Scattered electrons are attracted by a high voltage applied before detector and hit the detector tip (normally coated by scintillator substance), produce signal. A basic illustration of an FE-SEM is presented in Fig. 2.14.

Our studies used a FE-SEM (Hitachi SU 8020), with upper secondary electron detector to mapping the surface morphology of AZO thin film and the coverage of Al on AZO surface.

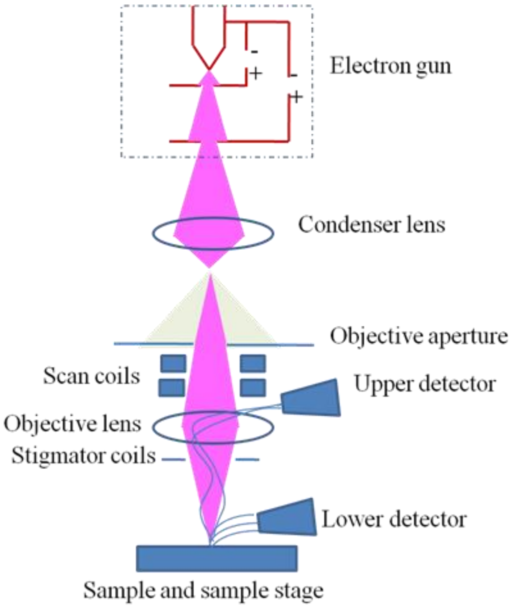

Fig. 2. 14. Basic construction of FE-SEM.

Reference

[1]. D. Gaspar, L. Pereira, K. Gehrke, B. Galler, E. Fortunato, R. Martins, Sol. Energy Mater Sol. Cells., 163 (2017) 255-262.

[2]. X. Noirfalise, T. Godfroid, G. Guisbiers, R. Snyders, Acta Mater., 59 (2011) 7521-7529.

[3]. T. Nakada, Y. Ohkubo, A. Kunioka, Jpn. J. Appl. Phys, 30 (1991) 3344.

[4]. H. T. Chang, G. J. Chen, Thin Solid Films, 618 (2016) 84-89.

[5]. A. Singh, S. Chaudhary, D. K. Pandya, Acta Mater., 111 (2016) 1-9.

[6]. F.H. Wang, C.L. Chang, Appl. Surf. Sci., 370 (2016) 83-91.

[7]. J. Nomoto, H. Makino, T. Yamamoto, J. Appl. Phys., 117 (2015) 045304.

[8]. E. N. Kaufmann, Characterization of materials, Wiley, Hoboken, New Jersey, USA, 2003, pp. 411-413.

[9]. J. I. Pankove, Optical process in semiconductor, Dover publications Inc., 180 Varick street, Newyork, 1975, pp. 114-169.

[10]. B. Segall, G.D. Mahan, Phys. Rev., 171 (1968) 935-948.

[11]. Princeton Instruments, Operating Instructions Acton Series SP-2500i, https://www.princetoninstruments.com

[12]. P. van der Heide, X-ray photoelectron spectroscopy, Wiley, Hoboken, New Jersey, USA, 2012.

[13]. http://www.thermo-riko.co.uk/TDS1200-ESCO.

[14]. P. van der Heide, Secondary ion mass spectrometry An introduction to principles and practices, Wiley, Hoboken, New Jersey, USA, 2014.

[15]. Nanotechnology Solutions Partner, Basic Contact AFM & Dynamic Force Microscope (DFM) Basic Topographic Imaging, https://www.parksystems.com/images/spmmodes/standard/2_Basic-Contact-AFM-and-Dynamic-Force-Microscopy-(DFM).pdf

[16]. S. K. Sharma, Handbook of Materials Characterization, Springer Nature, Cham, Switzerland, 2018, pp. 113-144.

Chapter 3. Enhancement in opto-electrical properties of ZnO and Al-doped ZnO thin films using Ar plasma treatment

As mentioned in chapter 1, in ZnO materials, there native defects such as V_O, Zn_i, O_i, V_{Zn}, antisites O_{Zn} and Zn_O, as well as their complexes exist. Even though the influence of these defects on opto-electrical properties of ZnO-based materials are still controversial so far, they have been considered as recombination centers. Some of them act as non-radiative recombination centers, and others act as radiative recombination centers which induce deep-level emissions (DLEs) in the visible wavelength region [1-3]. The transition of e-h pairs through these recombination centers leads to weak near-band-edge emissions (NBEs), which are attributed to the band-to-band emissions, free-excitonic and donor-bound excitonic emissions and their longitudinal phonon replicas [1]. Such defects also significantly affect the carrier transport in ZnO materials.

In literature, post-annealing in H_2 gas [4], or H_2 plasma treatment [5-7] have been employed to improve optical and electrical properties of ZnO based materials. The results were attributed to the incorporation of H into the ZnO materials at the interstitial sites (H_i), in complexes with oxygen vacancies (H_O) or in complexes with Zn vacancies (H_{Zn}). In these positions, H can act as shallow donors and also passivate the defects which H forms complexes with [5, 8-11]. However, researchers also argued that H interacts with O and remove weakly bonded O atoms from ZnO, therefore improve electrical conductivity of ZnO materials [12, 13]. Other plasma treatments using N_2 gas [14] and Ar gas [15, 16] were found to enhance the photoluminescence of ZnO nanowires and nanorods, similar to effect of hydrogen plasma. Dev et al. [15] and Baratto et al.[16] suspected the effects may originated from H. Ar plasma and He plasma have been used to improve the electrical conductivity of ZnO-based materials [17-19]. The effects were mostly attributed to the etching effect of plasma, which caused the dissociation of O atoms on the sample surface, resulting in the formation of donors such as V_O and Zn dangling bonds [19-21].

Although plasma treatments using inert gas such as Ar and He have been reported to improve electrical properties of ZnO based thin films, the mechanism of the improvement has not been fully understood. There was no study investigated simultaneously effects of such plasma on electrical properties and photoluminescence properties of ZnO film films. In this chapter, we aim to investigate simultaneously the effects of Ar plasma treatment on both electrical properties and photoluminescence properties of ZnO based thin films, in order to understand about the mechanism of the improvements obtained using plasma treatment.

ZnO and Al-doped ZnO (AZO) films with different thickness (50 – 500 nm) were prepared using RF magnetron sputtering in Ar (99.9999%) gas at a substrate temperature of 250°C on alkali free glass substrate (Corning glass) and synthetic silica glass substrate (Ichikawa glass). The working pressure was controlled by Ar flowing rate at 37.5 sccm to maintain a working pressure of 1 Pa. The RF power was 150 W. A sintered ZnO target (99.99%) was used for deposition of ZnO films, and another ZnO target containing 2 wt % Al_2O_3 was used for deposition of Al-doped ZnO films. The base pressure before deposition was ~ 4×10^{-5} Pa. The deposited ZnO and Al-doped ZnO films were then cut into 1 cm^2 pieces and treated with Ar plasma in a low vacuum chamber (Yamato Scientific, Pipi system) which has base pressure of 5 Pa and an RF power source. To understand the effect of plasma treatment, the evolutions of electrical and optical properties, as well as crystalline structure have been studied using a Hall effect measurement (Nanometrics, HL5500PC) with the Van der Pauw method, a spectrophotometer (Hitachi, U-4100) with spectral range of 200 - 2500 nm, and X-ray diffraction (XRD) measurements with Cu Kα radiation (Rigaku ATX-G diffractometer), respectively. To understand the effect of plasma on optoelectrical properties of ZnO thin film, we studied the evolution of PL spectra with plasma treatment time using a spectrometer (Princeton Instruments, SP2500) equipped with a charge-coupled device detector (PIXIS256E).

A He–Cd laser (λ = 325 nm) was used for excitation. The laser light was cut by a sharp cut filter in front of the spectrometer to avoid influence of stray light. He and O_2 plasma treatments in low vacuum chamber, as well as Ar plasma treatment in a high vacuum chamber (base pressure of 5×10^{-5} Pa) have been done on ZnO films for comparison with Ar plasma in low vacuum chamber. Surface morphologies of the samples was investigated using an atomic force microscopy (AFM) (JEOL, SPM). The thicknesses of the films were measured using a surface profiler (KLA-Tencor, Alpha-Step IQ). A secondary-ion mass spectroscopy (SIMS) (PHI ADEPT 1010), with Cs+ irradiation and acceleration voltage of 5.0 kV, has been employed to study the depth distribution of elements inside plasma treated sample.

3.1. Improvement of electrical conductivity of ZnO-based thin films using Ar plasma treatment

ZnO thin films have been treated using Ar plasma in low vacuum chamber. Fig. 3.1 shows the variation of electrical properties of 180 nm-thick-ZnO thin film grown on alkali free glass substrate by Ar plasma treatment in 4 min with different Ar flowing rate under the RF power of 9W. The corresponding of pressure with Ar flowing rate was also included. These results show that after using plasma treatment, both carrier concentration and Hall mobility were increased, leading to the reduction of resistivity. There was a slight dependence of electrical properties on Ar flowing rate. This can be explained by the increase in working pressure, or in other words, plasma density with the increment of Ar flowing rate.

Fig. 3.2 shows the electrical properties of ZnO thin film treated by Ar plasma for 4 min with a moderate Ar flowing rate of 6 ml/min, corresponding to a pressure of ~ 11 Pa, and different RF power. The results show that the Hall mobility was increased, but with higher powers, 40-100W, the Hall mobility was reduced compared to Hall mobility of sample treated with lower power. Meanwhile, the carrier concentration was increased with plasma power. These results imply the different evolution of Hall mobility and carrier concentration. The slight decrease of Hall mobility with high plasma power can be explained by etching on the surface caused by bombardment of high kinetic energy ions, as revealed by AFM images in Fig. 3.3. The continuous increase of carrier concentration may be attributed to the deeper and stronger effect of plasma treatment inside ZnO film. It is also explained by the etching on the surface which removed the O atoms and caused the formation of Zn dangling bonds and V_O [19]. However, this possibility might be not dominated, according to following studies.

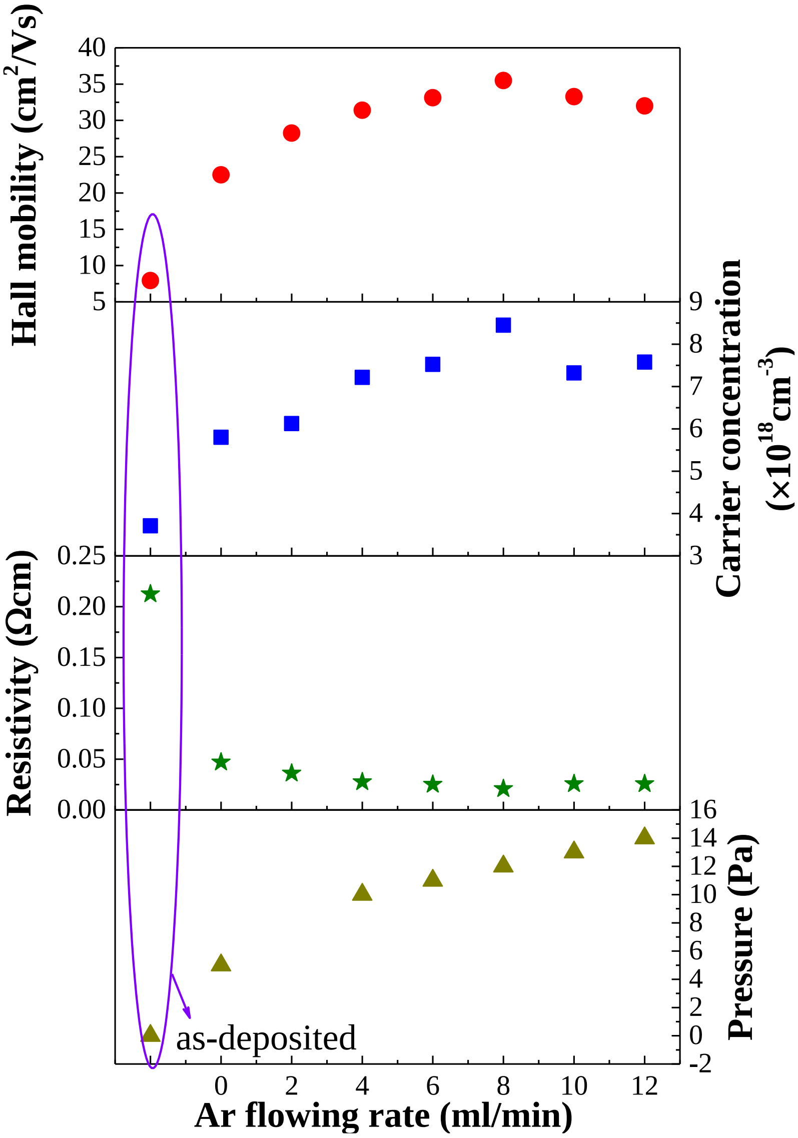

Fig. 3. 1. Electrical properties of 180 nm-thick-ZnO thin film before and after treated by Ar plasma for 4 min at an RF power of 9 W with different Ar flowing rates, corresponding to different working pressures.

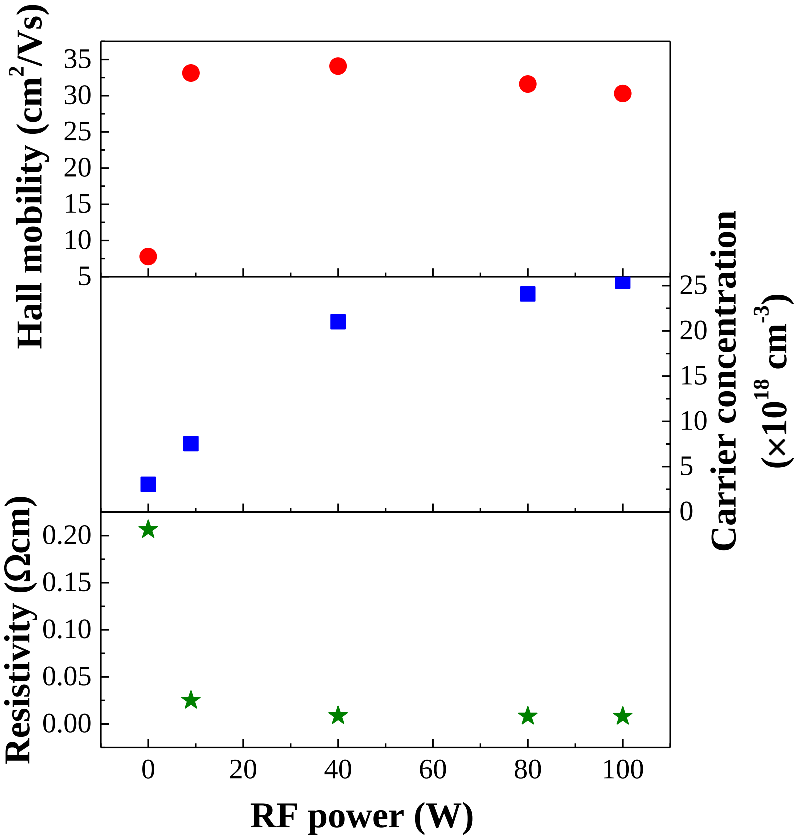

Fig. 3. 2. Evolution of electrical properties of 180 nm-thick ZnO film under Ar plasma treatment for 4 min at an Ar flowing rate of 6 ml/min with different RF power.

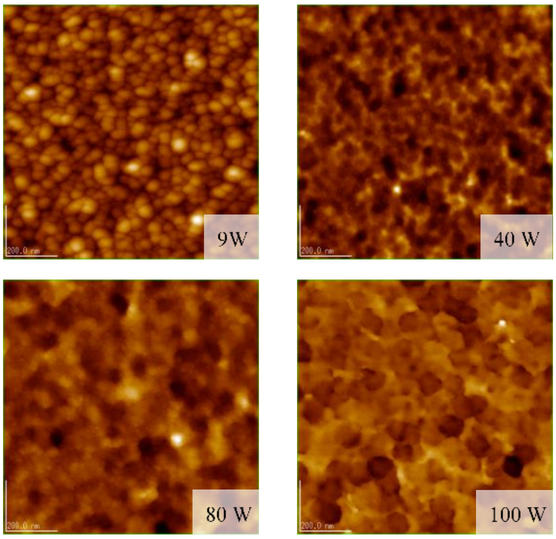

Fig. 3. 3. AFM images of 180 nm-thick-ZnO thin films treated by Ar plasma for 4 min, with different RF powers.

To closely investigate the influence of Ar plasma, we studied the evolution of electrical properties with plasma treatment time at a low RF power of 9 W and a moderate Ar flowing rate, and this evolution was presented in Fig. 3.4. This figure clearly shows the difference in the evolution of Hall mobility and carrier concentration. The Hall mobility significantly increased after a short time of exposure to the plasma and became saturated after 5 – 10 min treatment. For further plasma treatment time, above 15 min, a slight decrease in Hall mobility was observed. This degradation in Hall mobility can be explained by etching on the surface as shown in Fig. 3.5, similar to the results obtained using high plasma power. Carrier concentration was increased continuously with plasma treatment time, regardless of the reduction of Hall mobility. As a result, the electrical resistivity of ZnO thin film drastically decreased at first, but then gradually decreased and saturated with further treatment time.

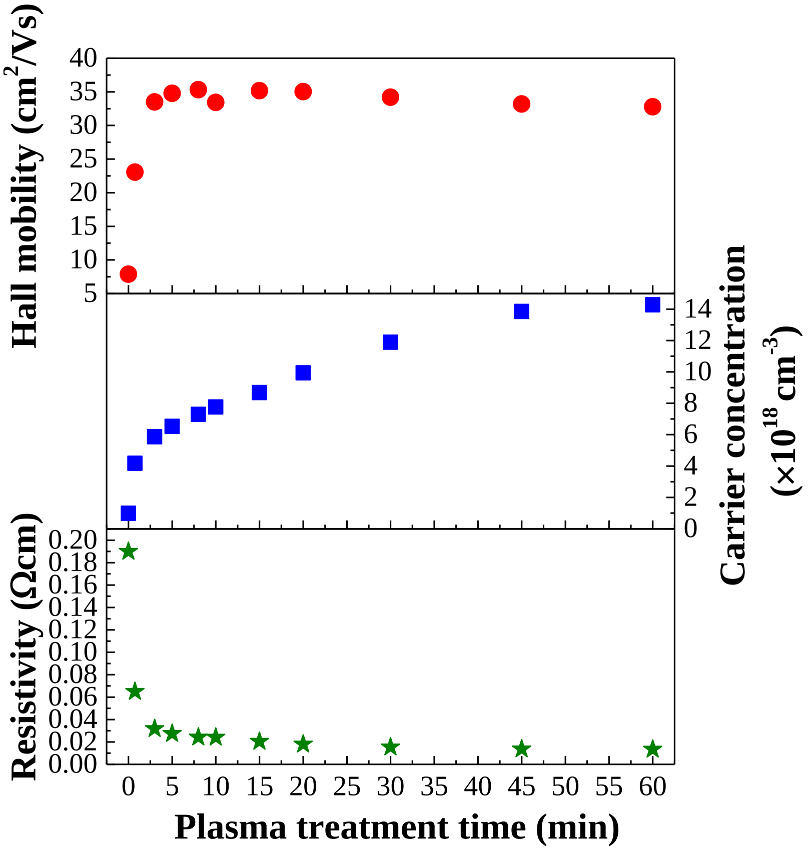

Fig. 3. 4. Evolution of electrical properties of 180 nm-thick-ZnO thin film with plasma treatment time.

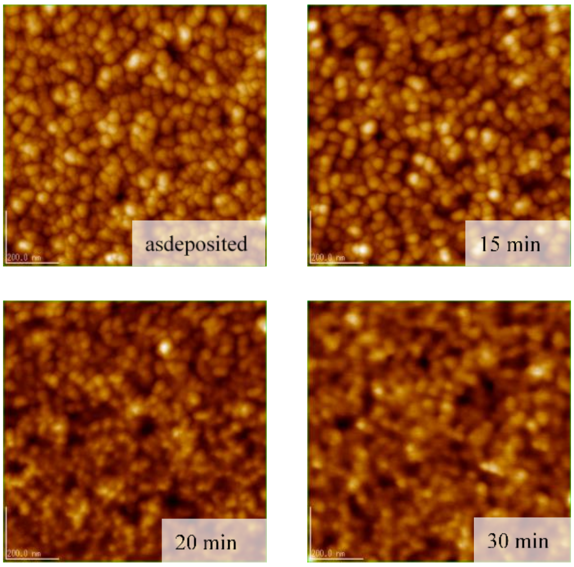

Fig. 3. 5. AFM images of ZnO sample before and after Ar plasma treatment at a power of 9W and Ar flowing rate of 6 ml/min.

Similar effects were obtained on different ZnO films grown on other substrate as well as different thickness. We also investigated the effect of Ar plasma on Al-doped ZnO (2 wt %) (AZO) thin films. Hall mobility and carrier concentration were increased (Fig. 3.6), leading to reduction of resistivity. However, because the as-deposited AZO sample exhibited low resistivity due to its high carrier concentration, the improvement obtained using Ar plasma was not so impressive. The increase in Hall mobility was not as strong as that in ZnO thin films. However, the different evolutions of Hall mobility and carrier concentration in both Al-doped ZnO and ZnO films implies the different influences on carrier concentration and Hall mobility. Following studies can get close insights into the mechanism of improvement obtained in Hall mobility and carrier concentration of ZnO-based thin films obtained using Ar plasma.

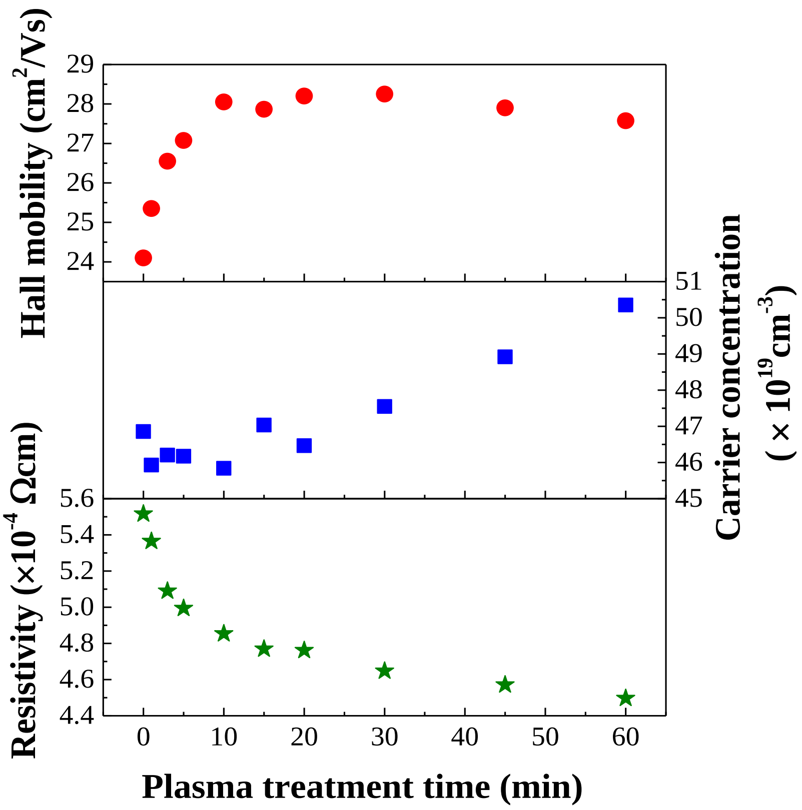

Fig. 3. 6. Evolutions of electrical properties of Al-doped ZnO film (2 wt.% Al_2O_3) with Ar plasma treatment time.

3.2. Passivation effect of plasma treatment – correlation between PL and electrical properties of ZnO thin film.

To get insight into the effect of plasma treatment and how it can lead to the increases in Hall mobility and carrier concentration, we deposited ZnO films on a synthetic silica glass substrate to investigate the evolution of PL spectra. Fig. 3.7 shows the PL spectra of 50 nm-thick ZnO film before and after plasma treatment. The as-deposited ZnO film showed the typical PL of polycrystalline ZnO which normally consists of an NBE band in the ultraviolet range and a broad DLE band in the Vis range. The broad DLE band can be de-convoluted into green emissions around 2.4 eV, yellow-orange emissions around 2.1 eV and red emissions around 1.8 eV, which were attributed to the radiative recombination through the deep level defects of V_O [22-24] or V_{Zn} [25, 26], O_i [2], and V_{Zn} [27], respectively. The relatively intense yellow-orange and red emissions suggest the existence of acceptor-type defects related to O_i and V_{Zn}. In the PL of as-deposited ZnO film, the intensity of NBEs and DLEs were comparable. After plasma treatment, the NBEs intensity significantly increased while DLEs intensity decreased. The decrease in DLEs implies that the deep level radiative defects were passivated. Once the deep level defects were passivated, the transitions through them was suppressed and therefore, the NBEs intensity would increase. However, the increase in NBEs could also stem from other factors. The integrated intensities of DLEs (multiplied by 30), NBEs and total PL integrated intensity of ZnO films were presented in Fig. 3.8 (a) as functions of plasma treatment time. According to the Fig.3.8 (a), the intensity of total PL was continuously increased with plasma treatment time, and the total PL intensity was nearly identical to the intensity of the NBEs. This implies that the increase in NBEs after the plasma treatment was significantly larger than the decrease in DLEs. Therefore, the plasma treatment, beside passivated the radiative defects, also passivated the non-radiative defects. It is worth noting that the intensity of DLEs decreased sharply after short plasma duration and almost saturated for longer treatment time, while the intensity of NBEs continuously increased with plasma treatment time. These evolutions were similar to evolutions of Hall mobility and carrier concentration, respectively (Fig. 3.8). These similarities might imply the strong correlation between PL and electrical properties.

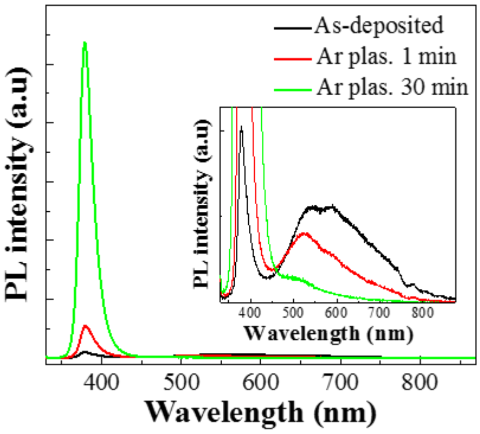

Fig. 3. 7. Photoluminescence spectra of 50 nm-thick-ZnO film before and after Ar plasma treatment.

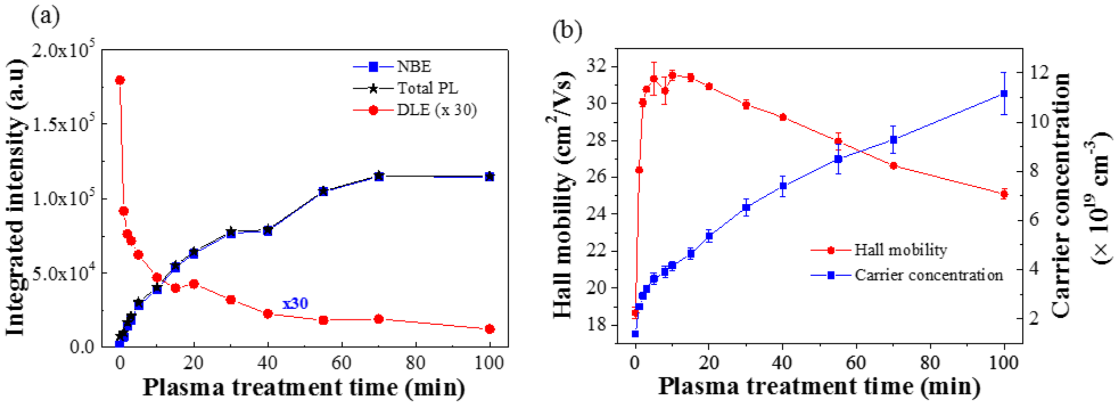

Fig. 3. 8. Evolutions of NBEs, DLEs and total PL integrated intensities (a), evolutions of Hall mobility and carrier concentration (b) of 50 nm-thick ZnO film with plasma treatment time.

The correlation between PL characteristics and electrical properties can be reflected through the evolution of electrical properties and PL of two different ZnO samples with two differently initial states. A ZnO film was deposited by RF magnetron sputtering on a 30 nm-thick Zn-polar ZnO buffer layer which was prepared by ion-plating [28]. This sample exhibited Zn-polar, while ZnO sample deposited directly on silica glass substrate exhibited O-polar, as reported elsewhere [28]. These two samples showed different PL spectra as well as different electrical properties. As shown in Fig. 3.9 (a), as-deposited 250 nm-thick Zn-polar ZnO film had a dominant NBE with a significantly weaker DLE, in comparison with 190 nm-thick O-polar ZnO film. This difference suggested that the density of deep-level defects in the Zn-polar ZnO film was lower than that in the O-polar ZnO film. As a result, Hall mobility and carrier concentration of the Zn-polar ZnO film were higher than those of the O-polar film, which were 29.8 cm^2/Vs and 9.2 × 10^{18} cm^{-3} compared to 19 cm^2/Vs and 3.7×10^{18} cm^{-3}. Fig. 3.9 (b) shows the enhancements of electrical properties of Zn-polar ZnO film in comparison with O-polar ZnO film as functions of Ar plasma treatment time. As shown in Fig. 3.9 (b), the increases in carrier concentration of these two samples were similar, and they continuously increased with plasma treatment time. However, the enhancements in Hall mobility were different. We did not observe a steep increase in Hall mobility of Zn-polar sample at the early stage of the plasma treatment as observed in O-polar sample. This can be attributed to the difference in the number of passivated defects. These evolutions strongly suggested the correlation between NBEs and carrier concentration, and the correlation between Hall mobility and DLEs.

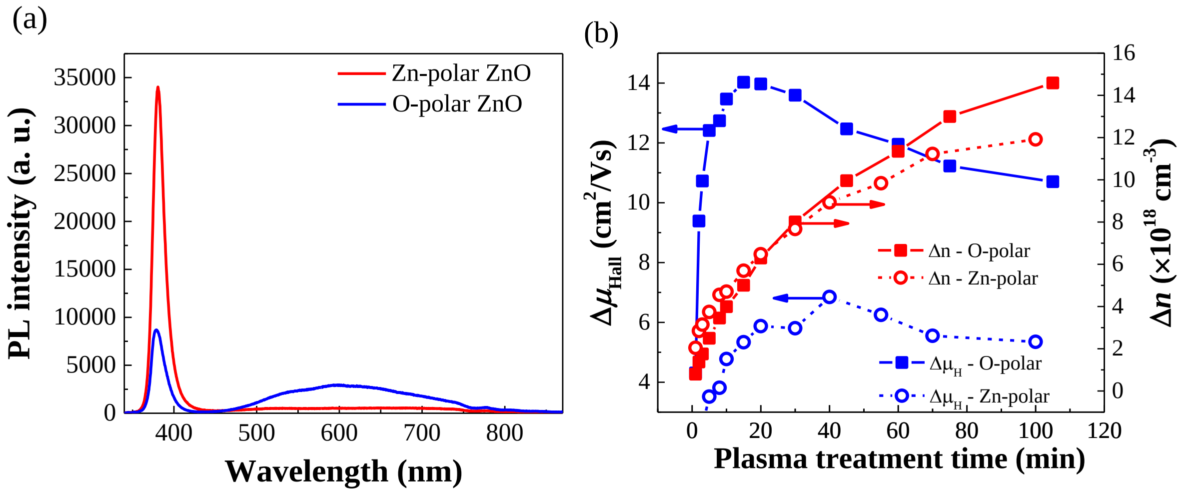

Fig. 3. 9. Photoluminescence spectra of as-deposited 250 nm-thick Zn-polar ZnO film, in comparison with 190 nm-thick O-polar ZnO film (a), and the enhancement in Hall mobility (Δμ_H) and carrier concentration (Δn) of these two films with the plasma treatment time.

3.3. Incorporation of hydrogen atoms from plasma environment – possible reason for the improvement in the optoelectrical properties obtained using Ar plasma treatment

The effect of plasma on electrical properties was normally ascribed to the etching on the surface [21, 29]. However, in our case, it was shown that when surface was etched, the Hall mobility was somehow decreased. To get insight to the deep influence of plasma treatment, we investigated the crystalline structure and optical spectra of the ZnO films. Fig. 3.10 shows the effect of Ar plasma treatment on the optical absorption of 50 nm-thick ZnO. The absorption coefficient was derived from the transmission and reflection spectra of ZnO film according to the equation (2.15), with the actual thicknesses after plasma treatment. The result shown that after plasma treatment, the absorption band edge shifted to a shorter wavelength, corresponding to a higher energy. The blue-shift of absorption band edge was attributed to the increase in the carrier concentration, which was described as Burstein-Moss shift [30]. Particularly, the excitonic peak in the absorption spectrum, which was ascribed to the absorption of the excitons [31, 32], was suppressed. This suppression could be attributed to the increase in charge carrier concentration in the ZnO film, owing to the screening effect on the Coulombic interaction of excitons. This obvious decrease in the excitonic peak of the ZnO film could reveal the bulk effect of the plasma treatment. This implies that the plasma treatment was not only effective on the surface, but also affected deeper into the bulk of the ZnO film. Plasma treatment did not result in any noticeable increase in absorption coefficient in the visible range, or any strange absorption peak, implying that no sub-gap state was formed by plasma treatment. The transparency of ZnO film was retained.

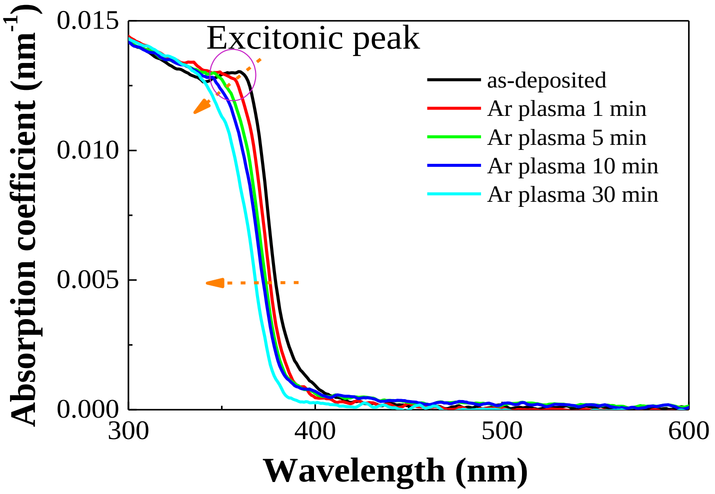

Fig. 3. 10. Absorption spectra of ZnO film before and after plasma treatment.

The deep effect of plasma treatment was also observed by the changes in the crystalline lattice parameters, which were evaluated using both in-plane 2θχ-φ scan and out-of-plane 2θ-ω scan, in XRD measurements. The XRD profiles of 50 nm-thick ZnO films were presented in Fig. 3.11, with the magnified view of two typical peaks 002 and 100. The intense 002 peak in out-of-plane XRD profile implies a wurzite structure with a preferred *c*- axis orientation, which is perpendicular to the substrate surface. As shown in Fig. 3.11(c) and (d), the plasma treatment led to the decrease in the diffraction intensity, accompanied with the broadening of the peaks. These results suggested that the plasma treatment deteriorated the crystalline structure of ZnO film. Moreover, the out-of-plane 002 peak shifted to a lower angle while in-plane 100 peak shifted to a higher angle, corresponding to an increase in the lattice constant *c* and a decrease in lattice constant *a*, respectively. The variations of lattice constants *c* and *a*, and therefore, the variation of unit cell volume *V* were presented in Fig. 3.12. The change in the unit cell volume was not substantial. These results imply that the lattice cell in the grain was distorted and might bear a stress owing to an incorporation of new ions or atoms at the grain boundaries by the plasma treatment.

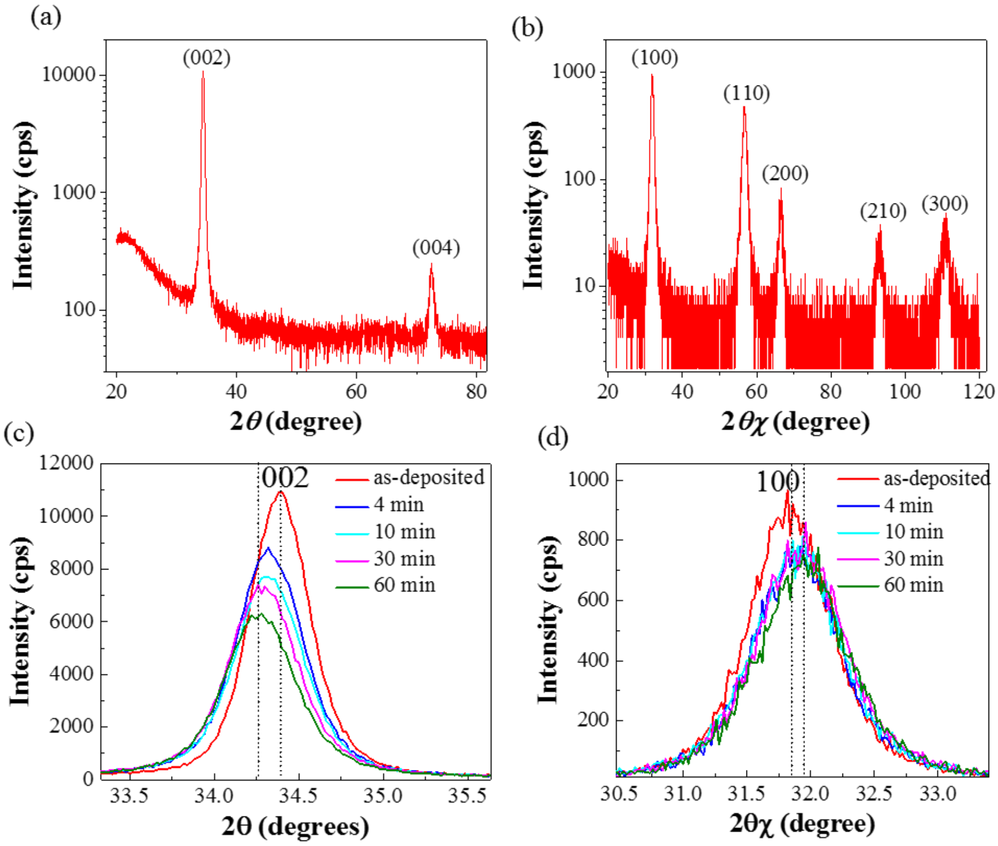

Fig. 3. 11. Out-of-plane XRD (a) and in-plane (b) of as-deposited 50 nm-thick ZnO film and the magnification of 002 peak (c) and 100 peak (d) before and after plasma treatment.

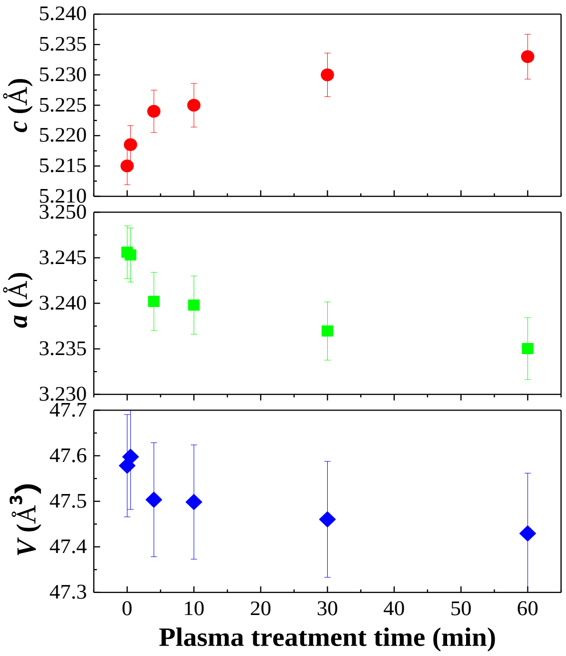

Fig. 3. 12. Evolutions of lattice constant *c, a*, and unit cell volume *V* of ZnO film with Ar plasma treatment time.

It is necessary to mention that the effects we obtained by Ar plasma treatment using low vacuum chamber were also obtained using He plasma treatment in this apparatus. However, O_2 plasma treatment using this apparatus could not result in such improvements. In other words, O_2 plasma treatment did not have influences on optoelectrical properties of ZnO film. Other Ar plasma treatment using high vacuum chamber (with base pressure of 5×10^{-5} Pa) could not improve optoelectrical properties of ZnO films, too, even with long duration (as shown in Fig. 3.13). This difference suggested that the effects obtained using Ar plasma treatment in low vacuum chamber might not be attributed to the bombardment of Ar ions on the surface of ZnO film, but other ions which come from the residual gases such as H_2, H_2O or hydrocarbons. Because H has been reported as a passivant and shallow donor in ZnO material [15, 33], and H ions can react with O ions to nullify the effect of H in case of O plasma, we speculated that the obtained effects using Ar plasma in low vacuum chamber could be attributed to the H ions created by collisions of Ar ions and electrons with the residual gases. To prove this speculation, we employed SIMS to detect the depth distribution of H in the ZnO film. It was studied that migration energy of H in ZnO is quite low, and therefore, H can easily to migrate into ZnO. The penetration depth of implanted H ions can reach to 25 μm [34]. Therefore, a thicker ZnO film, 430 nm, was used to investigate the depth profile of H. As shown in Fig. 3. 14, H atoms naturally existed in the ZnO film, that might be due to the synthesis process [35, 36]. The sample treated using Ar plasma in low vacuum chamber showed the higher H concentration in the first ~100 nm under the surface, in comparison with as-deposited film. This penetration depth, ~100 nm, is reasonably large to effectively change the bulk properties of 50 nm-thick-ZnO film. This result suggested that the incorporation of H atoms might account for the enhancement in optoelectrical properties of ZnO film, as well as the distortion of the crystal lattice. H atoms might be incorporated into the vacant positions, stuck with some dangling bonds or lodged themselves into the interstitial sites, leading to disorder in the lattice [8, 13, 37].

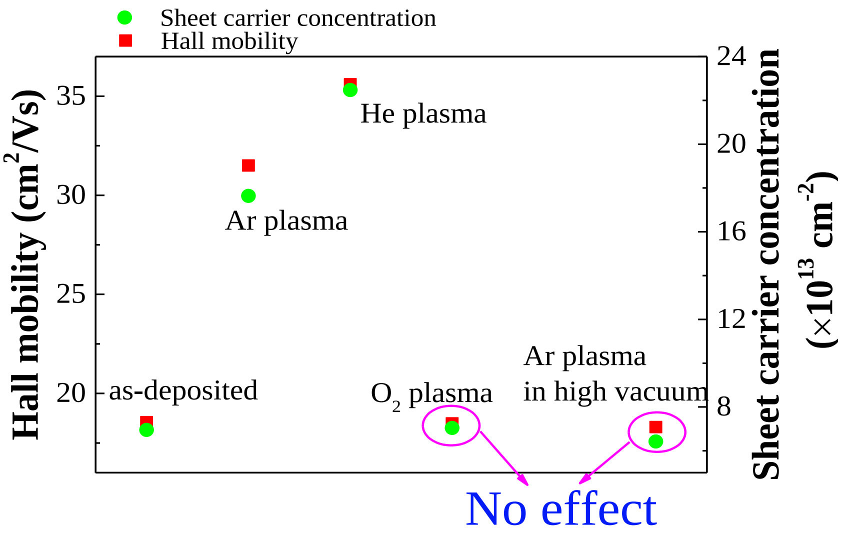

Fig. 3. 13. Comparison effects of different plasma treatments on Hall mobility and sheet carrier concentration of ZnO thin film. All Ar, He and O_2 plasma were operated at same conditions with power of 9 W, flowing rate of 6 ml/min for 5 min. Ar plasma in high vacuum chamber was operated for 1 h with RF power of 10 W, working pressure of 6 Pa.

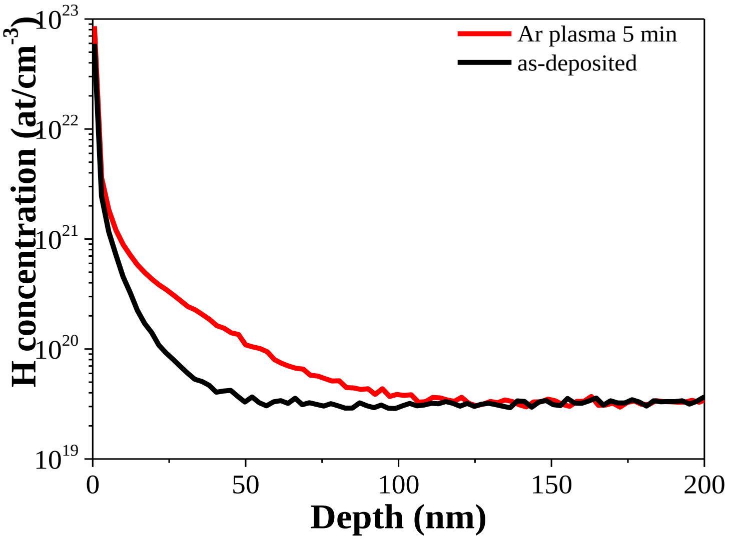

Fig. 3. 14. Depth profile of H concentration in ZnO films characterized using SIMS.

As mentioned in previous section, the steep increase in Hall mobility and reduction in DLEs might imply the passivation on defect sites. The broad yellow-red DLEs in as-deposited film could be attributed to the existence of acceptors-like defects O_i and V_{Zn}, which can trap and scatter electrons, leading to the low Hall mobility and carrier concentration. Once H atoms migrated into ZnO film, they reacted with these defects and passivated them. The passivation can be tentatively described as follows, for instance:

$$V_{Zn}^{-} + H \to H_{Zn} + e$$

$$O_i^{-} + H \to H - O_i + e$$

The passivation of these defects can release the trapped electrons, resulted in the increase in carrier concentration and Hall mobility. Moreover, transitions through these deep level defects were passivated, and the DLEs became weaker. Therefore, the NBEs were enhanced.

However, the difference between evolution of NBEs and DLEs implies other roles of H. Significant increase in total PL intensity suggests that H might also passivate non-radiative defects in ZnO, leading to the significantly larger enhancement in NBEs compared to the reduction in DLEs. Moreover, H might occupy the interstitial positions or V_O positions and acts as shallow donors which contributed to the enhancement in carrier concentration [8], and enhancement in NBEs by increase in number of transitions through the H donors such as donor bound excitonic emission and donor states to band emission [6, 15].

The distortion of the lattice, represented by changing of lattice constants, suggests that H possibly migrated and located at GBs, leading to the in-plane compressive strain after plasma treatment. The GBs are discontinuities of the crystalline structure, therefore, large number of dangling bonds and defects exist, creating a space charge region and a potential barrier at GBs. This space charge region can scatter electrons and reduce NBE transitions. When H migrated into ZnO film, and passivated these dangling bonds and defects, space charge region was narrowing, contributing to the enhancement of NBEs, carrier concentration and Hall mobility.

We should mention here that the Hall mobility was somehow decreased at long plasma exposure time. One possible explanation for the reduction in Hall mobility is the increase in ionized impurity scattering when the concentration of H becomes sufficiently high [38, 39]. For ZnO polycrystalline films, ionized impurity scattering became significant for carrier concentration above 10^{20} cm^{-3} [40-41]. However, carrier concentration of undoped ZnO films were in order of $10^{18} – 10^{19}$, not sufficiently high enough for Hall mobility to be dominated by ionized impurity scattering. Another possible factor for the reduction of Hall mobility is the damage of the sample surface caused by ion bombardment. The reduction in our samples was observed simultaneously with the etching on the surface. The reduction in Hall mobility in thinner ZnO films was stronger than reduction in thicker ZnO films, although the increasing rate in carrier concentration was comparable, suggesting stronger influence of surface scattering to Hall mobility in thinner film. In addition, carrier concentration was significantly stronger increased using He plasma treatment, while higher Hall mobility was obtained, compared with Ar plasma. Therefore, the reduction of Hall mobility with long plasma treatment may be dominated by the damage of the sample surface caused by the ion bombardment. As mentioned above, the etching effects were observed with plasma treatment time of longer than 15 min. By the etching, defects such as dangling bonds and V_O [42, 43], which can trap or scatter electrons, could be created near the surface region. Such the defects and deterioration of crystal lattice by the bombardment resulted in the decrease in Hall mobility at the longer plasma treatment time, in competition with the passivation effect of hydrogen.

3.4. Conclusions

This chapter demonstrated that Ar plasma treatment in low vacuum chamber can significantly improve the electrical properties of ZnO-based thin film, simultaneously increase the NBEs. The enhancements were ascribed to the passivation effect of the plasma, on both radiative defects and nonradiative defects. The influences of the plasma were not only on the surface but also in the bulk of the film, which was demonstrated by the reduced excitonic absorption peak and changes in lattice constants. The evolutions of electrical properties and PL intensity suggested the correlation between the deep-level defects and Hall mobility and that between the carrier concentration and NBE. The results obtained by SIMS strongly suggested the incorporation of H atoms into ZnO film. This might account for the enhancement in electrical and PL properties of the ZnO film. H atoms passivated the defects, and also acted as shallow donors, contributing to continuous increases in NBE and carrier concentrations with plasma treatment time. This treatment is a convenient method to improve the Hall mobility of ZnO-based thin film, applied for the electronic devices. The passivation of the defects and increase in NBEs are benefits for application in LED or lasing devices. However, what kind of passivated defects still be a challenge to study.

References

[1]. Ü. Özgür, Y. I. Alivov, C. Liu, A. Teke, M. A. Reshchikov, S. Doğan, V. Avrutin, S. -J. Cho, H. Morkoç, J. Appl. Phys. , 98 (2005) 041301.

[2]. N. H. Alvi, K. U. Hasan, O. Nur, M. Willander, Nanoscale Res. Lett., 6 (2011) 130.

[3]. D. Montenegro, V. Hortelano, O. Martínez, M.C. Martínez-Tomas, V. Sallet, V. Muñoz, J. Jiménez, , Mater. Res. Soc. Symp. Proc., 1538 (2013) 317-322.

[4]. R. Xie, D. Li, D. Yang, T. Sekiguchi, M. Jiang, Nanotechnology, 17 (2006) 2789.

[5]. P. F. Cai, J. B. You, X. W. Zhang, J. J. Dong, X. L. Yang, Z. G. Yin, N. F. Chen J. Appl. Phys., 105 (2009) 083713.

[6]. J. J. Dong, X. W. Zhang, J. B. You, P. F. Cai, Z. G. Yin, Q. An, X. B. Ma, P. Jin, Z.G. Wang, P. K. Chu, ACS Appl. Mater. Interfaces, 2 (2010) 1780-1784.

[7]. N. Ohashi, T. Ishigaki, N. Okada, H. Taguchi, I. Sakaguchi, S. Hishita, T. Sekiguchi, H. Haneda, J. Appl. Phys., 93 (2003) 6386.

[8]. C. G. Van de Walle, Phys. Rev. Lett., 85 (2000) 1012.

[9]. E. Lavrov, J. Weber, F. Börrnert, C. G. Van de Walle, R. Helbig, Phys. Rev. B, 66 (2002) 165205.

[10]. F. Selim, M. Weber, D. Solodovnikov, K. Lynn, Phys. Rev. Lett., 99 (2007) 085502.

[11]. W. Chen, L. Zhu, Y. Li, L. Hu, Y. Guo, H. Xu, Z. Ye, Phys. Chem. Chem. Phys., 15 (2013) 17763-17766.

[12]. H. P. Chang, F. H. Wang, J. Y. Wu, C. Y. Kung, H. W. Liu, Thin Solid Films, 518 (2010) 7445-7449.

[13]. M. Wu, T. Huang, C. Jin, L. Zhuge, Q. Han, X. Wu, IEEE Trans. Plasma Sci., 42 (2014) 3687-3690.

[14]. J. Rodrigues, T. Holz, R. F. Allah, D. Gonzalez, T. Ben, M. R. Correia, T. Monteiro, F.M. Costa, Sci. Rep., 5 (2015) 10783.

[15]. A. Dev, R. Niepelt, J. P. Richters, C. Ronning, T. Voss, Nanotechnology, 21 (2010) 065709.

[16]. C. Baratto, E. Comini, M. Ferroni, G. Faglia, G. Sberveglieri, CrystEngComm, 15 (2013) 7981-7986.

[17]. H. Akazawa, J. Vac. Sci. Technol. A, 29 (2011) 031304.

[18]. F. -H. Wang, J. -C. Chao, H. -W. Liu, F. -J. Liu, Vacuum, 140 (2017) 155-160.

[19]. J. K. Yao, S. Chen, X. W. Sun, H. S. Kwok, Appl. Surf. Sci., 355 (2015) 702-705.

[20]. J. -M. Lee, K. -K. Kim, S. -J. Park, W. -K. Choi, Appl. Phys. Lett., 78 (2001) 3842.

[21]. H. Akazawa, Appl. Phys. Express, 2 (2009) 081601.

[22]. I. K. Akopyan, M. E. Labzovskaya, A. A. Lisachenko, B. V. Novikov, A. Y. Serov, V. V. Titov, N. G. Filosofov, Phys. Solid State, 58 (2016) 1767-1771.

[23]. K. Vanheusden, W. L. Warren, C. H. Seager, D. R. Tallant, J. A. Voigt, B. E. Gnade, J. Appl. Phys., 79 (1996) 7983.

[24]. A. Janotti, C. G. Van de Walle, Appl. Phys. Lett., 87 (2005) 122102.

[25]. F. Fabbri, M. Villani, A. Catellani, A. Calzolari, G. Cicero, D. Calestani, G. Calestani, A. Zappettini, B. Dierre, T. Sekiguchi, G. Salviati, Sci. Rep., 4 (2014) 5158.

[26]. A. Janotti, C. G. Van de Walle, Phys. Rev. B, 76 (2007) 165202.

[27]. J. Zhong, A. H. Kitai, P. Mascher, W. Puff, J. Electrochem. Soc., 140 (1993) 3644-3649.

[28]. H. Makino, H. Shimizu, Appl. Surf. Sci., 439 (2018) 839-844.

[29]. J. -S. Park, J. K. Jeong, Y. -G. Mo, H. D. Kim, S. -I. Kim, Appl. Phys. Lett., 90 (2007) 262106.

[30]. E. Burstein, Phys. Rev., 93 (1954) 632.

[31]. R. C. Rai, M. Guminiak, S. Wilser, B. Cai, M. L. Nakarmi, J. Appl. Phys., 111 (2012) 073511.

[32]. J. F. Muth, R. M. Kolbas, A. K. Sharma, S. Oktyabrsky, J. Narayan, J. Appl. Phys., 85 (1999) 7884.

[33]. N. Ohashi, Y. -G. Wang, T. Ishigaki, Y. Wada, H. Taguchi, I. Sakaguchi, T. Ohgaki, Y. Adachi, H. Haneda, J. Cryst. Growth, 306 (2007) 316-320.

[34]. K. Ip, M. E. Overberg, Y. W. Heo, D. P. Norton, S. J. Pearton, C. E. Stutz, B. Luo, F. Ren, D. C. Look, J. M. Zavada, Appl. Phys. Lett., 82 (2003) 385-387.

[35]. D. Gaspar, L. Pereira, K. Gehrke, B. Galler, E. Fortunato, R. Martins, Sol. Energy Mater Sol. Cells, 163 (2017) 255-262.

[36]. M. Morales-Masis, L. Ding, F. Dauzou, Q. Jeangros, A. Hessler-Wyser, S. Nicolay, C. Ballif, APL Mater., 2 (2014) 096113.

[37]. W. F. Liu, G. T. Du, Y. F. Sun, J. M. Bian, Y. Cheng, T. P. Yang, Y. C. Chang, Y. B. Xu, Appl. Surf. Sci., 253 (2007) 2999-3003.

[38]. I. Takahashi, Y. Hayashi, Jpn. J. Appl. Phys., 54 (2014) 01AD07.

[39]. W. M. Kim, Y. H. Kim, J. S. Kim, J. Jeong, Y. -J. Baik, J. -K. Park, K. S. Lee, T. -Y. Seong, J. Phys. D: Appl. Phys., 43 (2010) 365406.

[40]. S. Cornelius, M. Vinnichenko, N. Shevchenko, A. Rogozin, A. Kolitsch, W. Möller,

Appl. Phys. Lett., 94 (2009) 042103.

[41]. D. H. Zhang, H. L. Ma, Appl. Phys. A, 62 (1996) 487-492.

[42]. W. Kim, J. -H. Bang, H. -S. Uhm, S. -H. Lee, J. -S. Park, Thin Solid Films, 519 (2010) 1573-1577.

[43]. H. -R. Kim, G. -H. Lee, D. -H. Kim, J. Phys. D: Appl. Phys., 44 (2011) 185203.

Chapter 4. Improvement of electrical properties and their thermal stability of Al-doped ZnO thin film under annealing in N_2 gas using Al capping layer

One of the most important applications of ZnO thin films is transparent electrode (TE). In optoelectronic devices, it is necessary to employ the transparent electrodes which simultaneously possess high electrical conductivity and transparency. Therefore, the convention metal electrodes are not applicable in these devices, due to their high absorption and reflection in Vis range. Transparent conductive oxides (TCOs), which can be achieved by doping on wide band-gap semiconductors, are good choice for these applications. So far, two most used transparent conductive oxide are tin doped In_2O_3 (ITO) and fluorine doped SnO_2 (FTO). However, their high production cost, toxicity and limited source on earth crust raised demands on finding other TCO candidates. ZnO material, with its nontoxicity and abundance, its modifiable properties, have become a promising candidate for application of TEs. To modify its electrical properties, ZnO was normally doped with metals in group III such as Al, Ga, B, In and group IV such as Ti, Sn, Si, Zr [1-6]. Among of them, AZO have several advantages including high conductivity with small doping amount [7], low cost and non-toxicity. It has been employed in solar cell instead of ITO and FTO and have shown advantages such as higher fill factor (FF) and higher open circuit voltage (V_{OC}) in comparison with ITO and FTO [8-10].

High electrical conductivity of the materials can be achieved by increase in carrier concentration or increase in Hall mobility. For TEs application, to meet dual requirements of high conductivity and high transparency in Vis and NIR, the increase in Hall mobility is preferred than increase in carrier concentration because the increase in carrier concentration can lead to the reduction of transmittance in NIR range [11-13]. The preferred carrier concentration should be around 10^{20} cm^{-3}. According to the theoretical calculation, the limit of Hall mobility of polycrystalline AZO for this carrier concentration is approximately ~55 cm^2/Vs [14, 15].

Significant efforts have been done to improve the electrical conductivity of AZO films such as employing buffer layer to control crystallinity of AZO film [13], annealing in reduce gases such as Zn metal vapor and H_2 at a high temperature up to 600 °C [16-18], or co-doping [19-22]. Although lots of methods have been employed, it remained difficult to obtain such a high Hall mobility. A comparison of reported electrical and optical properties of doped ZnO films was listed in the table 4.1.

Table 4. 1. Electrical properties and average transmittance in 400 nm - 1200 nm range of reported doped ZnO thin films

Sample	**Fabrication method and treatment**	**ρ (× 10^{-4} Ω cm)**	**μ_H (cm^2/V s)**	**n (× 10^{20} cm^{-3})**	**T (%)**	**Reference**
1.9 wt% Al doped ZnO (350 nm)	RF MS at T_S = 500 ºC Blanket post-annealing with Zn film (80 nm) in H_2 at 550 ºC for 1h	3.1	15.8	13	~ 90	Gosh et al. (2018) [17]
2 wt % Al doped ZnO	RF MS on quartz glass substrate at T_S = 400 ºC, followed by annealing in H_2 at temperature of 300 ºC for 30 min	3.5	27.3	6.4	> 80	Tong et al. (2011) [16]
2 wt% Al doped ZnO	RF MS from vacuum heated target.	7.3	37.2	2.3	~ 80	Asemi et al. (2018) [12]
2 w% Al doped ZnO	DC MS at T_S = 320 ºC Post annealing in vacuum at 10^{-3} Pa, 400 ºC for 2h	1.5	33.3	12.6	~ 80	Fang et al. (2003) [23]
0.5 wt% Al doped ZnO (490 nm)	Grown on 10 nm Ga-doped ZnO buffer layer with well-defined (0001) orientation by DC MS	4.89	50.1	2.55	~ 83	Nomoto et al. (2016) [24]
2 wt% Al doped ZnO	Superimposed DC+ RF MS on Corning glass substrate	39.5	6.3	2.5	-	Kumar et al. (2018) [25]
Al doped ZnO	Deposited using MS in oxygen active gas Post annealing in a sealed quartz tube with Zn metal pellet at 600 ºC for 30 min	1.4	36.8	12	-	Zhan et al. (2011) [18]
2 wt% Al doped ZnO	RF MS at T_S = 500 ºC on fused silica glass substrate	4	19	10	~ 80	Mickan et al. (2018) [26]
Al doped ZnO	ALD on SiO_2/Si substrate at T_S = 200 ºC	16	25	1.6	-	Niemelä et al.

						(2019) [27]
Al and Ga co-doped ZnO	Aerosol assisted CVD	130	7.9	1	~ 75	Potter et al. (2018) [28]
Al and In co-doped ZnO		160	6.8	0.8	~ 68	
1.5 at% Sm^{+3} and 3 at% Al co-doped ZnO	Spray pyrolysis at T_S = 450 ºC	9.86	20.25	3.12	~ 82	Anand et al. (2018) [19]
1 wt% F and 1wt% Al co-doped ZnO	RF MS at T_S = 320 ºC	3.53	39.33	4.5	~ 80	Ji et al. (2019) [10]
1 wt% Ga and 1 wt% Al co-doped ZnO	DC MS on glass substrate at T_S = 350 ºC	3	42	5	~ 80	Zhu et al. (2015) [29]
0.975 wt% F and 0.5 wt % Al co-doped ZnO	RF magnetron co-sputtering from 1.3 wt% F and 2 wt% A doped ZnO targets with volume fraction 3:1 on glass substrate Post-annealing in vacuum with pressure below 10^{-6} Pa at 300 ºC for 2 h	6	42	2.5	-	Choi et al. (2005) [22]
2 wt% Sn and 1 wt% Al co-doped ZnO	Sol-gel dip coating Post annealing at 500 ºC	40	40	0.5	> 80 (400 nm-800 nm)	Pan et al. (2013) [30]
2 wt% B and 2 wt % Al co-doped ZnO	DC MS on glass substrate at room temperature Post annealing in vacuum at 600 ºC for 2 min	7.9	8.6	9.1	> 80 (400 nm-800 nm)	Gupta et al. (2014) [31]
2 wt% Ga and 2 wt % Al co-doped ZnO		4.4	11.8	12	> 80 (400 nm-800 nm)	
5 wt% Mg and 3 wt% Ga co-doped ZnO	RF MS at room temperature	1.4	20.3	21.7	~ 70	Kim et al. (2019) [11]

$Ga_{0.4}Zn_{0.96}O$(50nm) /$In_{0.024}Cd_{0.976}O$ (30 nm) /$Ga_{0.4}Zn_{0.96}O$(50nm)	RF MS at room temperature on quartz	0.75	~40	21	~ 90	Le et al. (2019) [32]
8 at % Ga doped ZnO	Atmospheric pressure plasma jet on glass substrate at T_S = 200ºC	8.7	8.3	8.7	~ 85 (400 nm-900 nm)	Chen et al. (2019) [33]
3 wt% AZO(40nm) /Ag NPs (10 nm) /3 wt% AZO(40nm)	Al-doped ZnO films were deposited using RF MS on glass Ag NPs film was deposited using supersonic cluster beam deposition	0.1	-	-	< 75	Torrisi et al. (2019) [34]

It has been reported that annealing at high temperature can improve the crystallinity of semiconductor films [35, 36]. Moreover, annealing was employed to activate the semiconductor component in optoelectronic devices. Once the TEs was used as substrate for other component in the devices, they might undergo a heating process [37, 38]. Unfortunately, ZnO, AZO and other doped-ZnO films do not have a good thermal stability. In other words, their electrical properties were degraded under annealing. Several capping layers have been employed to improve the thermal stability of AZO films such as antimony-doped tin oxide (ATO), zinc-stannate (ZTO), TiO_x, and NiO_x, Al_2O_3, SiO_2 and Si [39-44]. Au and Cu thin films also have been stacked between AZO in order to improve thermal stability of AZO films [45]. However, there have not been significant improvements in the thermal stability, even annealing in N_2 gas with thick capping layer, over 100 nm [43].

Nevertheless, some studies found that electrical properties of doped ZnO films can be improved by annealing in oxygen lacking environment, with protection of thick capping layer, for instance, 50 nm-thick amorphous Si capped AZO films annealed in N_2 gas [44, 46], or 100 nm-thick SiO_2 capped GZO films annealed in vacuum [47]. Although the resistivity was reduced, the capping layers were too thick. Moreover, the mechanism behind the improvement has not been well elucidated. There was lack of study on impact of crystallinity of the as-deposited films as well as the fabrication methods on the thermal stability of the capped and uncapped ZnO based thin films. These factors may account for the different results obtained on the same materials with similar thickness. Therefore, in this chapter, we investigated the thermal stability of AZO film under N_2 environment. The effect of crystallinity, which was controlled using substrate temperature (T_S), on the thermal stability of AZO films will be studied. Thin Al capping layers were employed to prevent the degradation of electrical properties of AZO films and simultaneously increase their electrical conductivities by annealing in O-lacking environment. Our results showed that the substrate temperature, or crystallinity, strongly affected to the thermal stability of the AZO samples. The ultrathin Al capping layer can effectively passivate the degradation of electrical properties of AZO sample, and resulted in very good thermal stability of the AZO sample, up to 600 °C in N_2 ambience. Moreover, an improvement in electrical conductivity was obtained using Al capping layer. The increase in Hall mobility was obtained only by annealing at 400 °C. High conductivity, especially high mobility of ~49.1 cm^2/Vs, can be obtained simultaneously with high transparency. In this study, the mechanisms of the degradation and mechanism of the improvement of electrical conductivity of AZO films obtained using Al metal capping layer will be explained.

In this studies, 250-nm-thick AZO films were deposited on alkaline-free glass substrates (Corning, Eagle XG) at different substrate temperatures (T_S) of 200 – 300 °C using superimposed magnetron sputtering, with an RF power of 150 W and a DC power of 25 W in pure Ar gas ambience (ULVAC, CS-L). A ceramic ZnO target containing 0.5 wt % of Al_2O_3 was used. The pressure was controlled to be 1 Pa with Ar flowing at a rate of 37.5 sccm during deposition. Prior to the deposition process, the glass substrate was treated with Ar plasma in the sputtering chamber under a power of 15 W and a pressure of 6 Pa at room temperature for 10 min. After the treatment, the substrate was heated up to 300 °C and the sputtering chamber was evacuated to a base pressure of 8×10^{-5} Pa. After deposition, the AZO films were kept inside the sputtering chamber to allow for cooling to room temperature. Then, Al thin films were deposited directly on the AZO films at room temperature using superimposed magnetron sputtering with RF power of 25 W and DC power of 50 W in pure Ar gas and a pressure of 1 Pa, using an Al metal target.

Thicknesses of all the films were measured using a surface profiler (KLA-Tencor, Alpha-Step IQ). With respect to the estimation of the Al film thickness, a thick Al film was initially deposited on the AZO film to evaluate the deposition rate. Then, the thickness of the Al film was controlled according to the deposition time. In our study, an ultrathin Al film of 2.2 nm was deposited on different AZO films to investigate the effect of ultrathin Al film on the thermal stability of the electrical properties of the AZO films. Thicker Al films (4.4 – 10.8 nm) have been deposited on AZO films to investigate the effect of Al film thickness on the thermal stability of AZO film.

The thermal stability of the AZO and Al/AZO samples was studied by annealing in flowing N_2 gas at different temperatures of 300 – 600 °C, for 1 hour. The heating rate was controlled at 20 °C/min. To investigate long term thermal stability, AZO and Al (2.2 nm)/AZO samples were annealed in N_2 gas ambience at 400 °C for different time durations. The electrical properties of the as-deposited and annealed samples were characterized using Hall effect measurement based on the Van der Pauw method (Nanometrics, HL5500PC). The optical properties of the samples were investigated using a spectrophotometer (Hitachi, U-4100) with a spectral range of 200–2500 nm. The optical spectra was then employed to deduce the optical mobility of coated and uncoated AZO samples based on Drude model, in order to evaluate the effect of grain boundaries on thermal degradation of electrical properties. The thermal desorption of atoms from the samples was monitored using thermal desorption spectroscopy

(Esco, TDS 1200 II). The oxidation state of the Al overlayer was examined via both hard X-ray photoelectron spectroscopy (HAXPES) using monochromatic Cr Kα radiation (5414.9 eV) and soft X-ray photoelectron spectroscopy (SXPS) using monochromatic Al Kα radiation (1486.6 eV). The coverage of Al on top of AZO sample was investigated using field effect scanning electron microscopy (FE-SEM) (Hitachi, SU 8020).

4.1. Thermal stability of AZO film under annealing in N_2 ambience – effect of crystallinity on thermal stability of AZO film

Different AZO films was deposited on alkali-free glass substrates at different T_S, 200-300°C. Their crystallinity was studied using out-of-plane 2θ-ω scan in XRD measurement and presented in Fig. 4.1 (a). All of the samples showed the dominated 002 and 004 peaks, implying that they have wurzite structure with preferred *c*-axis orientation. The AZO films deposited at higher temperatures showed higher diffraction intensities. Moreover, the diffraction peaks became narrower, and slightly shifted to higher angles when T_S increased. The 2θ diffraction angle of (002) plane located at 34.45°, 34.46° and 34.50°, with full width half maximum (FWHM) of (002) peak was 0.384, 0.349 and 0.334°, corresponding to T_S of 200, 250 and 300 °C. The slight narrowing of diffraction peak with increasing of T_S implies a slight increase in grain size, while the shift of diffraction peak to higher angles might be resulted from the reduction in the residual compressive stress [48]. However, the 2θ shift might also stem from the higher substitution of Al^{3+} for Zn^{2+} [49]. Sample deposited at T_S = 200°C also showed a shoulder peak at 36.23°, corresponding to the (101) plane which is not perpendicular to the *c*-axis. The degree of the orientation or the titling of the crystalline domains along the *c*-axis orientation was examined through the rocking curve scan of 002 peak, which was presented in Fig. 4.1 (b). As shown in this figure, with higher T_S, the rocking curve was narrower, implying a better *c*-axis orientation. These XRD results suggest an improvement in crystallinity of the film deposited at higher T_S, probably due to higher diffusion energy of constitution atoms, which enables the crystalline nucleation and growth [49-51]. The crystallinity generally has strong effects on optoelectrical properties of polycrystalline ZnO based thin films. The crystallographic defects such as dislocations, stacking faults and grain-boundaries (GBs) are charge scattering centers [52]. Dopant segregation at the GBs accompanied with zinc vacancies (V_{Zn}) in vicinity could cause the reduction in both carrier concentration and Hall mobility [53]. Chemisorbed oxygen at GBs was also believed to cause reduction of electrical conductivity [54, 55]. Therefore, the improvement in the crystallinity by increasing T_S would enhance the electrical properties of as-deposited AZO samples, as shown in Fig. 4. 2, probably due to reduction in crystallographic defects and narrower grain boundaries (GBs) [49, 56]. Higher T_S may also enhance the substitution of Al to Zn [48]. Accordingly, the Hall mobility and carrier concentration of as-deposited AZO films were increased with T_S, and the resistivity was decreased.

Thermal stability of electrical properties of AZO samples under annealing in N_2 gas was presented in Fig. 4.2. After annealing at 300 °C and 350 °C, carrier concentration and Hall mobility of AZO samples slightly increased, probably due to removal of adsorbates from the surface and GBs, except Hall mobility of AZO sample with T_S of 200 °C. Different from AZO samples deposited at T_S of 250 – 300 °C, Hall mobility of the AZO sample deposited at lower T_S of 200 °C already decreased with annealing temperature (T_A) of 300 – 350 °C. For higher T_A, 400 – 500 °C, all of the samples showed a strong reduction in Hall mobility. Simultaneously with decrease in Hall mobility, carrier concentration of all the AZO samples decreased with T_A from 400 °C. At T_A of 600 °C, Hall mobility of AZO samples deposited at 200 and 250 °C increased, probably due to the recrystallization by high temperature annealing. It can be seen from Fig. 4.2 that the reductions in carrier concentration in AZO samples were quite comparable and independent on T_S, while evolutions of the Hall mobility were obviously different and dependent on T_S. Sample deposited at lower T_S always showed lower Hall mobility, with higher reduction rate. As a result, the resistivity of all AZO samples was drastically increased with T_A from 400 °C. Due to large difference in Hall mobility of AZO samples, the resistivity of samples deposited at higher T_S was lower than that of sample deposited at lower T_S.

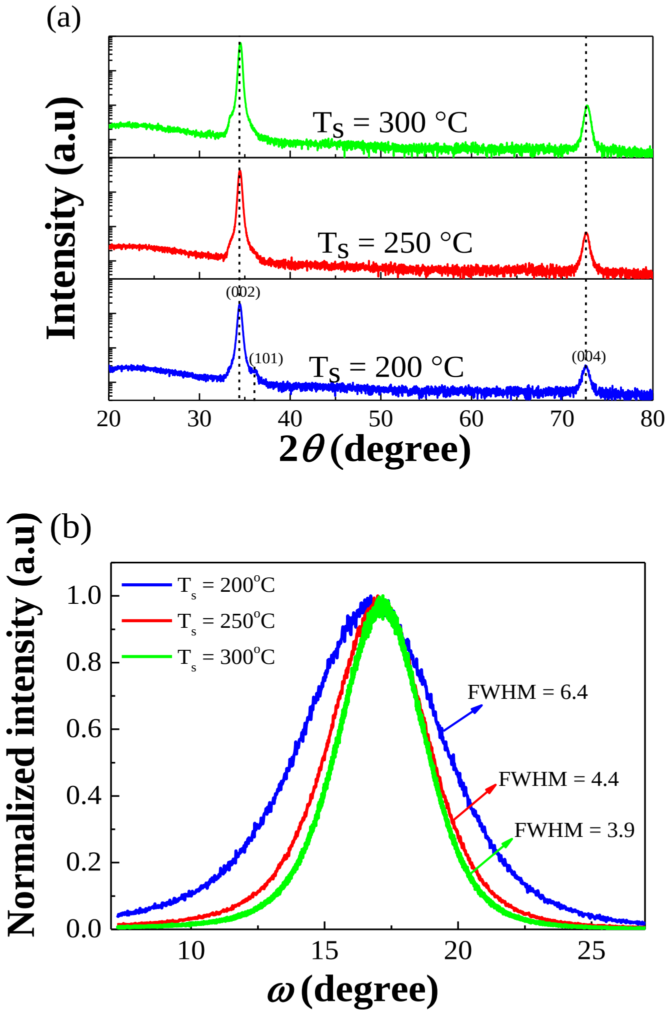

Fig. 4. 1. Out-of-plane XRD (a) and rocking curve of 002 peak (b) of AZO samples deposited at different substrate temperatures.

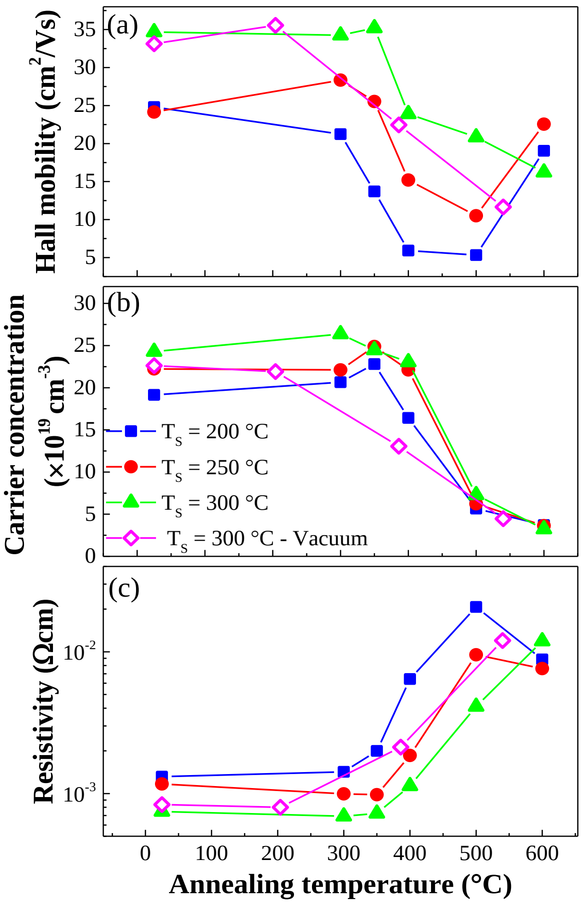

Fig. 4. 2. Evolution of Hall mobility (a), carrier concentration (b) and resistivity (c) of AZO samples deposited at different substrate temperatures with annealing temperature in N_2 gas (solid symbols). Electrical properties of AZO films (T_S = 300 °C) after heating in vacuum (via TDS) was included for comparison (open symbols).

Fig. 4.3 shows the evolution of transmission spectra of AZO (T_S = 200 – 300°C) samples with annealing temperature. As shown in this figure, all the as-deposited AZO samples had good transparency in the visible and NIR range, with average transparency of ~ 86% in the range from 375 nm to 1200 nm. For longer wavelength in the NIR range, the transmittance gradually decreased. The low transmittance in the NIR range was due to absorption and reflection of free-carriers. According to the Drude model, based on interaction of free carriers with an optical electric field, at a low frequency, corresponding to a long wavelength range, materials with a high free carrier concentration act as reflectors, like metals. The plasma frequency at which materials change from dielectric to metallic behavior is given by [57]:

$$\omega_p = \sqrt{\frac{ne^2}{m^* \varepsilon_0 \varepsilon_r}} \tag{1}$$

where ε_0 is the vacuum permittivity, ε_r is the relative permittivity of a material, n is the carrier concentration and m^* is the effective mass of an electron. When carrier concentration increases, the plasma frequency shifts to a higher frequency, corresponding to a shorter wavelength. And therefore, the transmittance is decreased. On the contrary, when carrier concentration decreases, plasma frequency shifts to a lower frequency, corresponding to a longer wavelength. We can see in Fig. 4.3 that after 1 h annealing in N_2 gas at temperature of 400 °C, the transmittance in the NIR range of all AZO samples slightly increased. For higher annealing temperatures, steep increase in transmittance of AZO samples in NIR range was observed. The increase in transmittance of AZO samples in NIR range was strongly consistent with decrease in their carrier concentration. Moreover, the fundamental absorption band edge, which was represented by the steep decrease in the transmittance in UV-Vis range, shifted to a longer wavelength. The red-shift of the absorption band edge can be explained by the Burstein-Moss shift [58], which is due to the reduction in the carrier concentration. These results agree well with the results of the electrical properties obtained using Hall measurements.

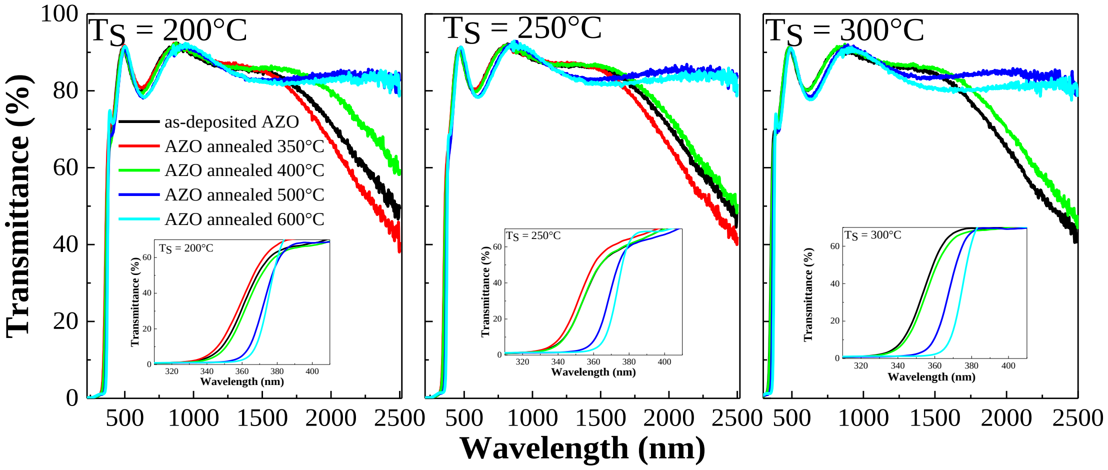

Fig. 4. 3. Transmission spectra of AZO samples before and after annealing in N_2 gas for 1 h. The insets are magnification of absorption band edge in transmission spectra.

The degradation of electrical properties of doped ZnO film under annealing in N_2 gas can be attributed to the desorption of Zn. The Zn desorption from ZnO has been reported using TDS spectra [59, 60]. The removal of Zn interstitial (Zn_i) or Zn atoms from lattice sites can result in the reduction of carrier concentration. Desorption of Zn from lattice sites may create the acceptor-like defects V_{Zn} which can compensate the carrier concentration and reduce Hall mobility. The Zn atoms along the GBs are more feasible to desorb, leading the increase in GBs potential barrier. Another possible reason for the degradation is the segregation of O and Al atoms along the GBs [61], which can enlarge the space-charged region and increase the potential barrier, preventing the charge transport. The difference in the thermal stability of AZO films deposited at different substrate temperatures also support for influence of GBs. For the samples deposited at higher temperatures, 250 °C and 300 °C, because of better crystallinity with better *c*-axis orientation, they have narrower GBs. Therefore, the number of dangling bonds and defect sites at the GBs are smaller than those in sample deposited at lower temperature, 200 °C, with poor *c*-axis orientation. Under annealing, more atoms can lodge themselves into the empty sites or form bonding with dangling bonds and defects at GBs, leading stronger segregation at the GBs in the sample deposited at low T_S. The GBs scattering was more increased, and then, the reduction in Hall mobility was stronger, as suggested in Fig. 4. 2 (a).

Other possible reasons for the difference in thermal stability of AZO samples deposited at different temperature are the contribution of the compactness of the AZO films [48], and the difference in stability of Zn_i due to different film growing temperatures. The loose surface morphology could cause strong chemisorption and diffusion of oxygen [48] or N_2 from annealing environment into the film. However, because of N_2 annealing, the effect of oxygen chemisorption and migration can be eliminated. The chemisorption of N_2 was supposed to occurred at surface and GBs, forming Al-N bonds and then, reducing density of donor-like defects and Al interstitials [16]. Nevertheless, the formation energy of AlN is sufficiently high, it is hard to form Al-N bonds at temperature of 400 – 600 °C [63]. Moreover, the strong reduction in electrical properties of AZO samples after heating in vacuum using TDS system, as also shown in Fig. 4.2, suggested N migrations and chemisorption were not primary reason. Although the effect of oxygen and N could be neglected, the differences in compactness and the difference in stability of Zn_i due to different T_S can lead to the difference in Zn desorption and result in the difference in thermal stability. To clear this issue, we studied the surface morphology of AZO samples and the TDS spectra of Zn from different AZO films. Fig. 4.4 shows the surface morphologies of AZO samples deposited at different substrate temperatures, measured using FE-SEM, accompanied with the average roughness measured using AFM. The figure shows the difference in the surface morphologies. It was likely that the sample deposited at higher temperature exhibited more uniform surface and finer grains than samples deposited at lower T_S, but the roughness was quite similar. The TDS spectra of Zn from these samples were presented in Fig.4.5. The desorption of Zn consists of two feature peaks. One small peak is approximately at 150 °C, which could be attributed to desorption of Zn from the surface [59]. Zn atoms from the surface where a large number of defects exist require a low excitation energy for desorption. This desorption does not have an influence on the electrical properties of AZO. Another desorption peak appeared at approximately 320 °C. This peak may represent the desorption of Zn interstitials (Zn_i) from bulk AZO or Zn atoms from the lattice sites [59]. The desorption of Zn from these positions leads to a reduction in the carrier concentration, and may also reduce Hall mobility. All the AZO samples showed the similar Zn desorption, regardless of different surface morphologies and T_S. These results suggested that the difference in the surface morphologies, or the compactness of the films, and the film growing temperature, did not affect to the Zn desorption in our samples. The similarity in Zn desorption was consistent with similarity in reduction of carrier concentration and steep decrease in Hall mobility of every AZO samples from T_A of 400 °C. Accordingly, Zn desorption might account for the reduction in carrier concentration, and stimulated the reduction in Hall mobility. However, the dependence of Hall mobility on substrate temperature in annealed AZO samples suggested other effects occurred at GBs.

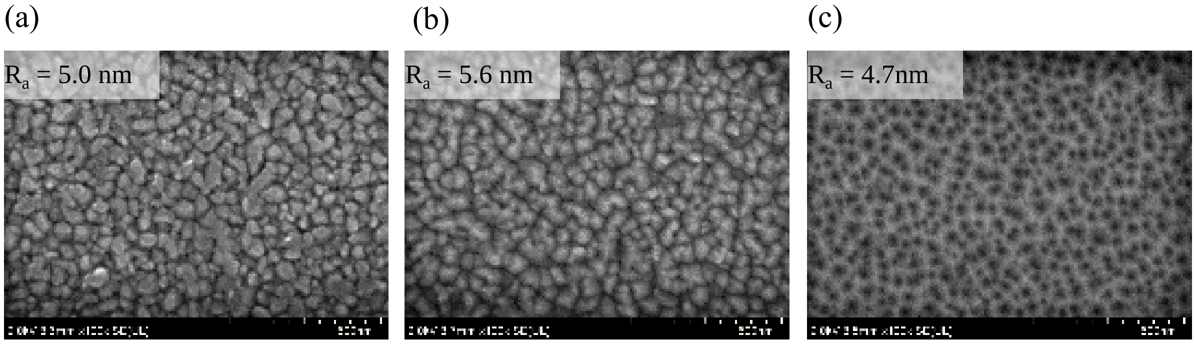

Fig. 4. 4. FE-SEM image of AZO samples deposited at T_S = 200 °C (a), T_S = 250 °C (b) and T_S = 300 °C (c), with average roughness (R_a) measured using AFM.

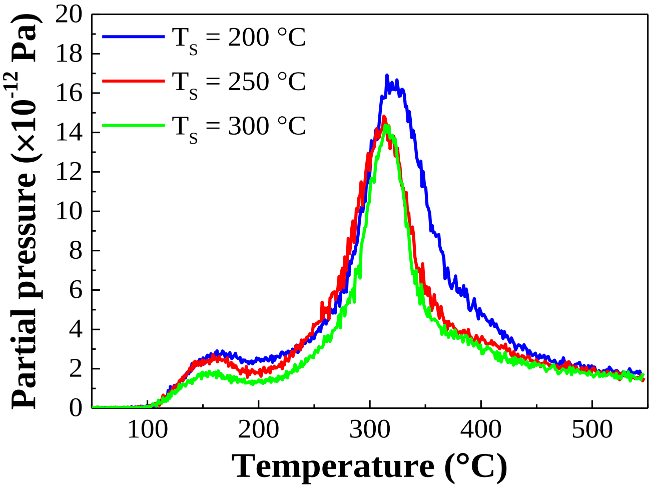

Fig. 4. 5. TDS spectra of Zn from AZO samples.

To evaluate the effect of GBs on the thermal stability of AZO films, we employed the optical spectra of AZO samples to deduce the contribution of mobility of free-charge carriers inside the grain and mobility through the GBs according to the Drude model. The dielectric function of the AZO can be expressed by [64]:

$$\varepsilon(E) = \epsilon_{TL}(E) + \epsilon_D(E) \tag{4.1}$$

where $\epsilon_{TL}(E)$ represents for the dielectric constant deduced from the Tauc-Lorentz model which accounts for the band gap transitions, and $\epsilon_D(E)$ represents for the contribution of free-charge carrier according to the Drude model. The $\epsilon_D(E)$ is given by:

$$\varepsilon_D(E) = -\frac{A_D}{E^2 - iE\Gamma_D} = \left(-\frac{A_D}{E^2+\Gamma_D^2}\right) - i\left(\frac{A_D\Gamma_D}{E^3+\Gamma_D^2 E}\right) \tag{4.2}$$

where $A_D = \frac{\hbar^2 n_{opt} e^2}{\varepsilon_0 m^*}$ is amplitude which proportional to the free carrier concentration n_{opt}, and $\Gamma_D = \hbar\gamma = \frac{\hbar e}{\mu_{opt} m^*}$ is broadening parameter, which is proportional to the damping coefficient γ, with $\hbar$, e, m^* are reduced Plank constant, electron charge, and electron effective mass, respectively.

Using this model, we can deduce the μ_{opt} from the optical spectra including transmittance (T), and reflection (R), or from the spectroscopic ellipsometry (SE) data. In this study, we employed T and R spectra in the range of 300 - 2500 nm to calculate the optical mobility of the AZO films. The optical carrier concentration was taken by Hall carrier concentration (n_{opt}= n), and effective mass m^* was derived from the A_D.The evolution of the μ_{opt} were presented in Fig. 4.6 (a). As shown in this figure, the optical mobility μ_{opt}, or ingrain mobility, of all as-deposited AZO samples are quite similar. This strongly implies that the difference in Hall mobility of as-deposited AZO samples deposited at different T_S was due to difference in the GBs scattering. The contribution of GBs scattering to the carrier transport can be evaluated via μ_{GB} or μ_{opt}/μ_{GB} ratio. High μ_{opt}/μ_{GB} ratio implies that the carrier mobility is dominated by GBs scattering while low μ_{opt}/μ_{GB} ratio, ~ 0, implies negligible contribution of GBs scattering. According to Fig. 4. 6 (b), the μ_{GB} of as-deposited AZO films with T_S of 300 °C was significantly high, accompanied with a small μ_{opt}/μ_{GB} ratio, ~ 0.3, implying that GBs scattering was negligible and carrier mobility in this sample was dominated by ingrain scattering. On the contrary, other two as-deposited AZO samples with lower T_S had lower μ_{GB} with μ_{opt}/μ_{GB} ~ 0.8 - 0.9, implying comparable contributions of GBs scattering and ingrain scattering. The higher GBs scattering in as-deposited AZO samples with lower T_S

was probably due to larger tilting of crystalline domains. After annealing, the μ_{opt} of all AZO samples increased, especially with T_A higher than 400 °C. This increment might be attributed to the annealing out of the defects inside the grains, such as the extinction of V_{Zn}, V_O, O_i or increase of substitution of Al to Zn [65]. Accordingly, the reduction in Hall mobility of AZO samples might be due to the increase in GBs scattering.

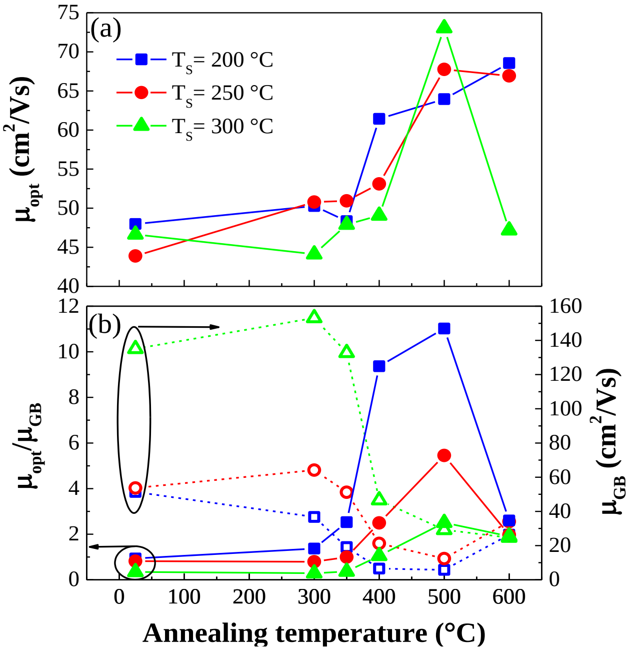

Fig. 4. 6. Calculated optical mobility μ_{opt} (a), and grain boundaries mobility μ_{GB} with μ_{opt}/μ_{GB} ratio (b) of AZO samples after annealing in N_2 ambience

Fig. 4.6 (b) shows that the μ_{GB} of samples deposited at T_S of 250-300 °C did not decrease with T_A of 300 – 350 °C, and obviously decreased after annealing at T_A of 400 °C. Correspondingly, the μ_{opt}/μ_{GB} ratios were nearly unchanged after annealing at T_A of 300 – 350 °C, and then drastically increased with higher T_A than 400 °C, at which the reduction in carrier concentration and Hall mobility were obviously observed. For AZO samples deposited at T_S of 200 °C, the μ_{GB} decreased and the μ_{opt}/μ_{GB} ratio increased after annealing from 300 °C. A steep increase in μ_{opt}/μ_{GB} was also obtained at T_A of 400 °C, similar to two other AZO samples. The decrease in μ_{GB} and the increase in μ_{opt}/μ_{GB} strongly imply the increase of GBs scattering. The steep increase of μ_{opt}/μ_{GB} in all AZO samples from T_A of 400 °C may be stimulated by desorption of Zn as aforementioned. Notably, the μ_{GB} and μ_{opt}/μ_{GB} of AZO samples obviously depended on the T_S. At any given T_A up to 500 °C, the sample deposited at higher T_S, always showed higher μ_{GB} and lower μ_{opt}/μ_{GB} than samples deposited at lower T_S. This imply a strong dependence of GBs scattering on crystallinity or alignment of crystalline domains. The contribution of crystallographic defects at GBs, due to mis-alignment of crystalline domains, might be maintained during annealing. Moreover, in AZO sample deposited at T_S of 200 °C, the μ_{opt}/μ_{GB} ratio increased at low T_A of 300 – 350 °C, while retained in other AZO samples deposited at higher T_S. This difference might suggest that, in AZO sample deposited at lower T_S, the segregation of defects at GBs occurred at lower T_A, compared to samples deposited at higher T_S.

The influence of crystalline domains alignments and the defects segregation to GBs during annealing on GBs potential barrier can be illustrated in the Fig. 4.7. Beside the contribution of crystallographic defects at GBs due to misalignment of crystalline domains (illustrated by red shapes), there are other defects segregated to GBs by annealing, including defects caused by Zn desorption (illustrated by green circles) and other segregation occurred in sample deposited at low T_S with poor crystallinity (illustrated by dark circles). The results deduced from optical properties confirmed the influence of the T_S, as well as film's crystallinity, on electrical conductivity and their thermal stability. Sample with better *c*-axis orientation will have higher Hall mobility and its mobility can be retained higher than mobility of sample with poor *c*-axis orientation under annealing.

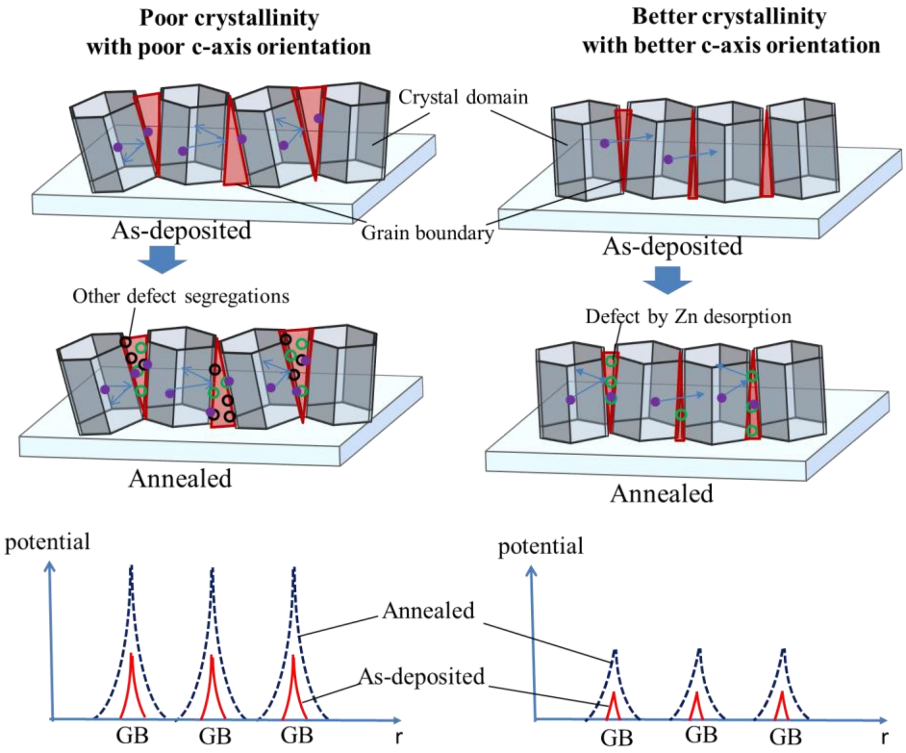

Fig. 4. 7. Illustration of effect of GBs on charge transportation in AZO film. The defects segregation at GBs caused increase in potential barrier, reduced the electrical conduction.

4.2. Improvement in electrical conductivity of AZO film and their thermal stability in N_2 gas by ultrathin Al capping layer.

Ultrathin Al films with thickness of 2.2 nm were deposited on top of AZO films. According to the SEM images in Fig. 4.8, Al was deposited uniformly over the AZO films. Effect of ultrathin Al film on electrical properties of AZO under annealing in N_2 gas was presented in Fig. 4.9. As shown in this figure, the as-deposited Al (2.2 nm)/AZO samples exhibited a slightly lower resistivity compared to that of as-deposited AZO samples. This slight reduction in resistivity might be due to the passivation of defects on the surface. Similar to the bare AZO films, electrical properties of Al (2.2 nm)/AZO films (T_S = 250 – 300 °C) slightly increased after annealing at 300 °C for 1 h in N_2. Their Hall mobility slightly increased, while Hall mobility of Al (2.2 nm)/AZO (T_S = 200 °C) already decreased from ~ 26.4 cm^2/Vs to ~

19.3 cm^2/Vs. For higher annealing temperatures, 350 - 500 °C, Hall mobility of Al/AZO (T_S = 200 °C) sample continuously decreased but remained higher than that of bare AZO sample. The minimum Hall mobility was still remained at a moderate value of ~ 14 cm^2/Vs, compared to ~ 6 cm^2/Vs of bare AZO sample. At annealing temperature of 600 °C, an increase in Hall mobility was obtained, probably due to improvement in crystallinity. Different from evolution of Hall mobility in Al (2.2 nm)/AZO (T_S = 200 °C) sample, Hall mobility of Al (2.2 nm)/AZO samples with AZO layer deposited at T_S = 250 °C and T_S = 300 °C increased by annealing. The Hall mobility of Al (2.2 nm)/AZO (T_S = 250 °C) sample firstly increased from ~ 27.4 cm^2/Vs to ~36.1 cm^2/Vs at annealing temperature of 350 °C, then slightly decreased for higher T_A, to ~ 34 cm^2/Vs at T_A of 400 °C – 500 °C, and raised to ~ 43.2 cm^2/Vs at annealing temperature of 600 °C. For Al (2.2 nm)/AZO (T_S = 300 °C) sample, the Hall mobility was much higher. It increased from ~ 38.5 cm^2/Vs to ~ 45 cm^2/Vs at annealing temperature of 350 °C, ~ 49.1 cm^2/Vs at annealing temperature of 400 °C, and ~ 54.4 cm^2/Vs at annealing temperature of 600 °C. This Hall mobility nearly reached to the theoretical limit. The difference in evolutions of Hall mobility of different Al/AZO samples implies that the evolution of Hall mobility of Al/AZO samples strongly depended on T_S, or in other words, depended on crystallinity of AZO layer.

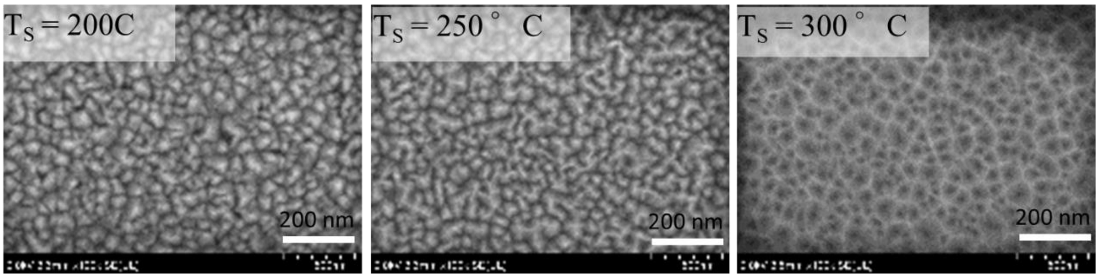

Fig. 4. 8. FE-SEM images of as-deposited Al (2.2 nm)/AZO (with T_S = 200 – 300 °C) samples.

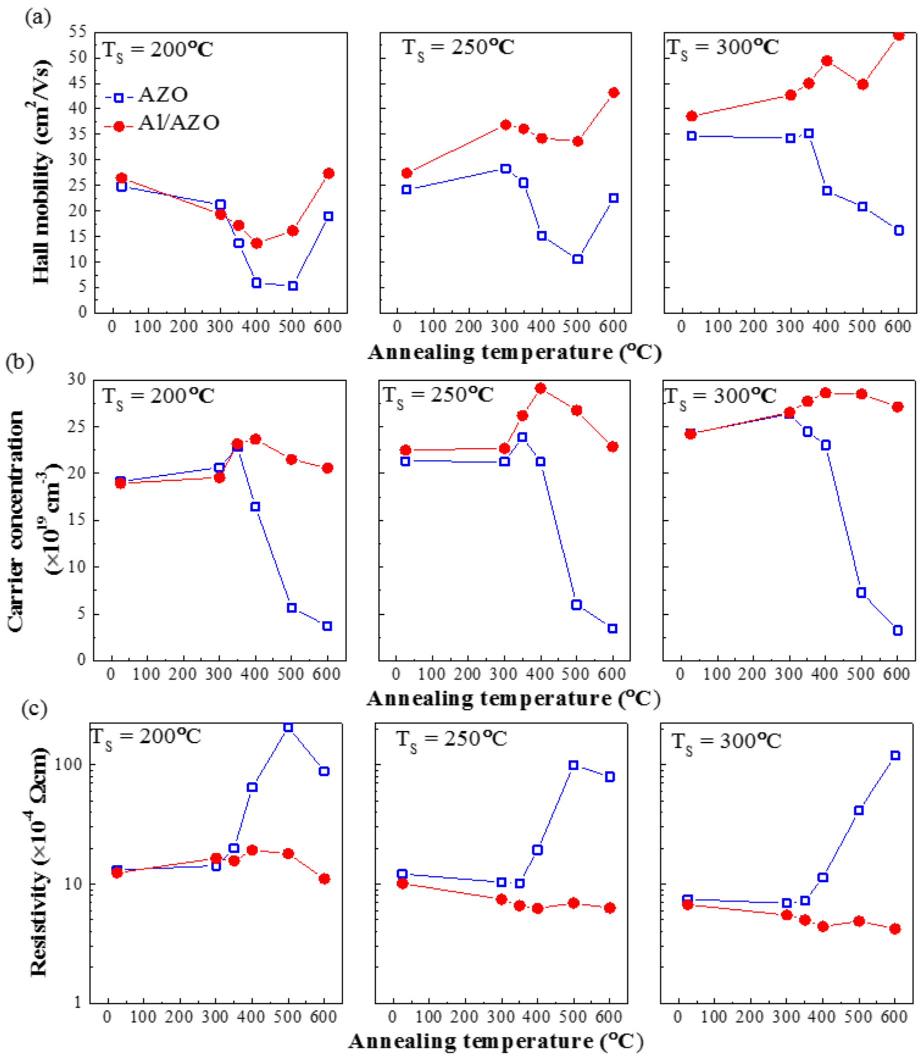

Fig. 4. 9. Evolutions of Hall mobility (a), carrier concentration (b) and resistivity (c) of Al (2.2 nm)/AZO samples, comparison with them of bare AZO films under annealing in N_2 gas for 1 h.

Interestingly, even though Hall mobility of Al (2.2 nm)/AZO (T_S = 200 °C) decreased with annealing temperature, the carrier concentration of this sample was found slightly increased after annealing with T_A of 300 – 400 °C, and then slightly decreased for higher T_A. Nevertheless, carrier concentration was remained comparable to the carrier concentration of as-deposited Al (2.2 nm)/AZO film, even after annealing at 600 °C. Similar evolutions of carrier concentration were observed in Al (2.2 nm)/AZO (T_S = 250 °C) and Al (2.2 nm)/AZO (T_S = 300 °C) samples. These results strongly suggest that the evolution of carrier concentration was independent on T_S, like in the bare AZO samples. As a consequence, the resistivity of Al (2.2

nm)/AZO (T_S = 200 °C) was increased slightly by annealing, but remained significantly lower than that of bare AZO samples. Resistivity of Al (2.2 nm)/AZO (T_S = 250 – 300 °C) samples was decreased by annealing. The resistivity of Al (2.2 nm)/AZO (T_S = 300 °C) decreased from ~ 6.7×10^{-4} Ω cm to ~ 4.5×10^{-4} Ω cm, corresponding to a decrease of sheet resistance from ~ 26.6 Ω/sq to ~ 17.7 Ω/sq by annealing at temperature of 400 °C for 1 h. The evolution of electrical properties of all Al (2.2nm)/AZO samples suggest that ultrathin Al capping layer can effectively prevent the degradation of electrical properties of AZO films under annealing in N_2 gas.

The evolutions of transmission spectra of Al (2.2 nm)/AZO (T_S = 200 – 300°C) samples with the annealing temperature were presented in Fig. 4.10. In this figure, the transmission spectra of as-deposited AZO samples were included for comparison. As shown in Fig. 4.10, the as-deposited Al (2.2 nm)/AZO samples exhibited high transmittance that was slightly lower than that of as-deposited AZO sample. In this study, the ultrathin Al film was deposited directly on AZO films at room temperature in Ar gas. However, after the samples were exposed to the air, the top of Al film was naturally oxidized. The existence and the oxidation of the Al film were confirmed based on XPS spectra of Al 1s and Al 2p core electrons, which showed one broad peak corresponding to the Al-O bond as presented in Fig. 4.11. The significantly stronger intensity of Al 1s peak as well as much lower intensity of Zn 2p peak in the HAXPES spectra of Al (2.2 nm)/AZO sample in comparison with those of the AZO sample, as shown in Fig. 4. 11 (d) and Fig. 4.11 (e), strongly support the existence of Al layer in oxidized state on top of AZO layer. Although no trace of Al metal was found by XPS, the slightly lower transmittance of Al/AZO sample in Vis range compared to that of AZO film implies the existence of incompletely oxidized Al atoms with oxygen vacancies, which decreased transmission via absorption and scattering of light.

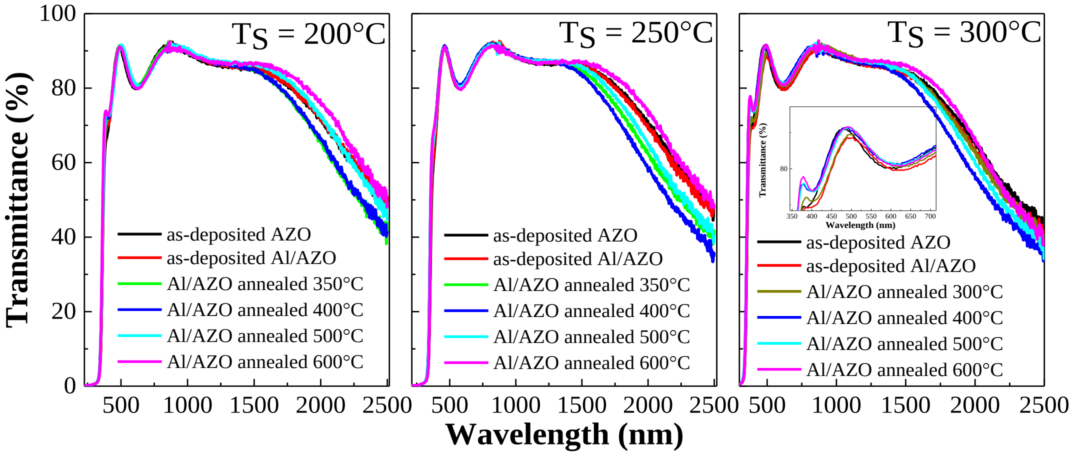

Fig. 4. 10. Transmission spectra of Al 2.2 nm/AZO samples before and after annealing in N_2 gas for 1h, in comparison with transmission spectra of as-deposited AZO samples. The inset show the magnification of transmittance spectra in the Vis range of Al/AZO (T_S = 300 °C) sample.

We can see in the Fig. 4.10 that after annealing in N_2 gas at 400 °C for 1h, transmission of all the Al/AZO samples reached to the level of the as-deposited AZO sample, implying a complete oxidation of Al capping layer. The complete oxidation of Al capping layer can be seen from the Fig. 4. 11 (c) with the narrowing of O 1s peak at the high binding energy side. The complete oxidation of Al capping layer by annealing in N_2 gas ambience might be due to interaction and slight inter-diffusion of atoms between top Al layer and AZO layer [63]. Although the inter-diffusion at annealing temperature of 400 °C was negligible, as indicated in Fig. 4.11 (a) and 4.11 (b) by extremely small change in intensity of Al 2p and Zn 2p peak, Al capping layer might capture oxygen atoms from AZO bottom layer. A slight decrease in transmittance in the NIR range was observed in Al (2.2 nm)/AZO samples after annealing at 350 °C and 400°C, due to increase in carrier concentration as observed in Fig. 4.9 (b). For higher annealing temperatures, the transmission in the NIR range slightly increased, implying a small decrease in carrier concentration, but remained lower than or comparable to transmittance of as-deposited AZO samples. The evolutions of the transmission spectra of Al (2.2 nn)/AZO samples were strongly consistent with the electrical properties of these samples.

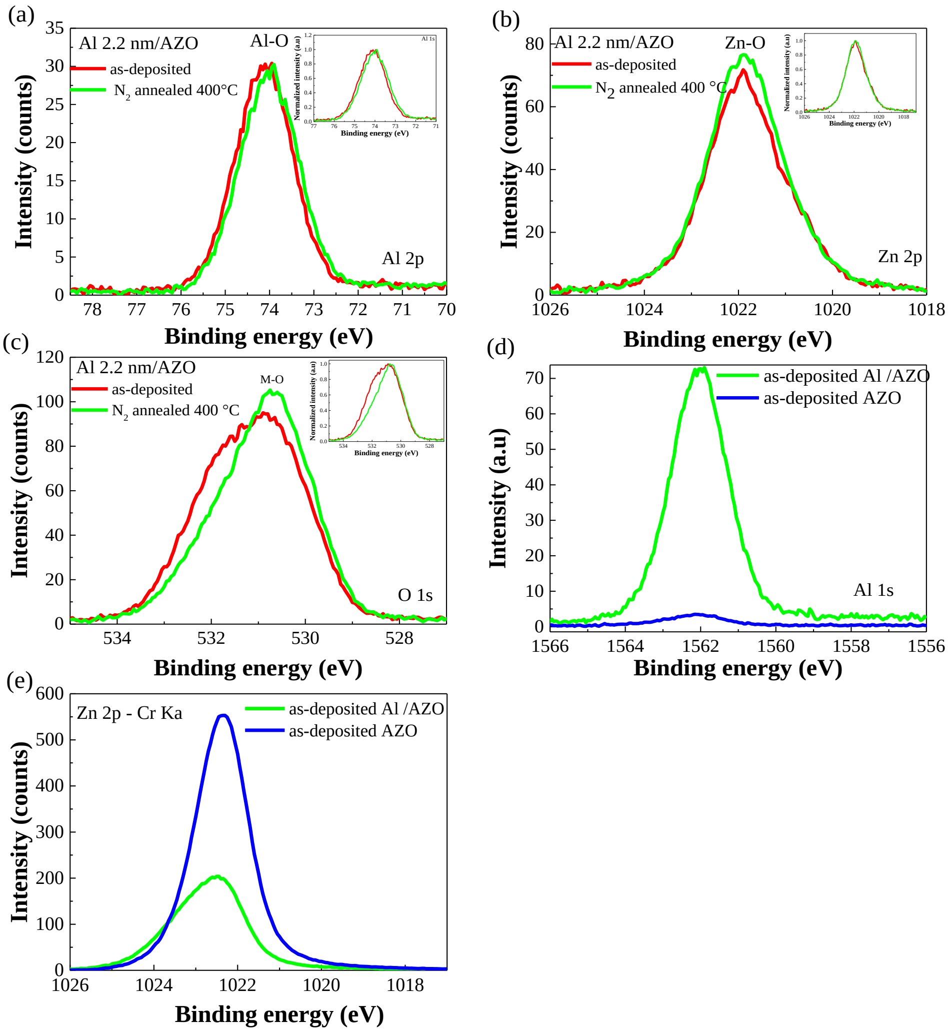

Fig. 4. 11. SXPS spectra of Al 2p (a), Zn 2p (b), O 1s (c) of Al (2.2 nm)/AZO sample (T_S = 300 °C) before and after annealing in N_2 gas at 400 °C for 1h (corrected using C 1s), and HAXPES of Al 1s (d) and Zn 2p (e) of as-deposited Al(2.2 nm)/AZO (T_S = 300 °C) sample in comparison with those of as-deposited AZO sample.

It is worth mentioning that the electrical conductivity of the Al/AZO (T_S = 250-300°C) samples was increased after annealing in N_2, starting from a low temperature of 350 - 400°C, while exhibited high transparency as high as that of bare AZO samples. The increase in electrical conductivity was mostly attributed to the increase in the Hall mobility with a small increase in the carrier concentration. By annealing Al/AZO (T_S = 300°C) sample in N_2 gas, we can obtain significantly high Hall mobility, ~ 49.1 cm^2/Vs at 400 °C and ~54.4 cm^2/Vs at 600 °C. For application as TCOs, such increase in Hall mobility is preferred than increase in carrier concentration.

Since a significant improvement of Hall mobility of Al/AZO (T_S = 250-300 °C) samples was observed at annealing temperature of 400 °C, while Hall mobility of AZO samples decreased at this temperature, we investigated the evolution of electrical properties of Al 2.2 nm/AZO (T_S = 300 °C) sample with annealing time at 400 °C in N_2 gas. Fig. 4.12 shows the long-term stability of the electrical properties of the Al 2.2 nm/AZO (T_S = 300 °C) sample annealed in N_2 at 400 °C, in comparison with the stability of the AZO sample. As shown in this figure, the Hall mobility and carrier concentration of bare AZO sample decreased monotonically with the annealing time, resulted in the continuous increase in the electrical resistivity, or continuous degradation of the electrical conductivity. This result suggests continuous desorption of Zn and continuous segregation of defects at the GBs during annealing. For Al/AZO sample, the Hall mobility drastically increased to a value of approximately ~ 49.6 cm^2/Vs, and then remained at this level for further annealing duration. The carrier concentration also increased slightly and remained high. As a result, the resistivity was decreased drastically to an optimum value after annealing for 30 min, and then remained constant for further annealing time. These results suggested that ultrathin Al layer is very effective to prevent the degradation of electrical properties of bottom AZO layer. The evolutions of the electrical properties were well consistent with the evolutions of optical properties, as shown in Fig. 4.13. While transmission spectra of AZO sample showed an continuous increase in NIR range, the transmission spectra of Al(2.2 nm)/AZO sample did not change with annealing time.

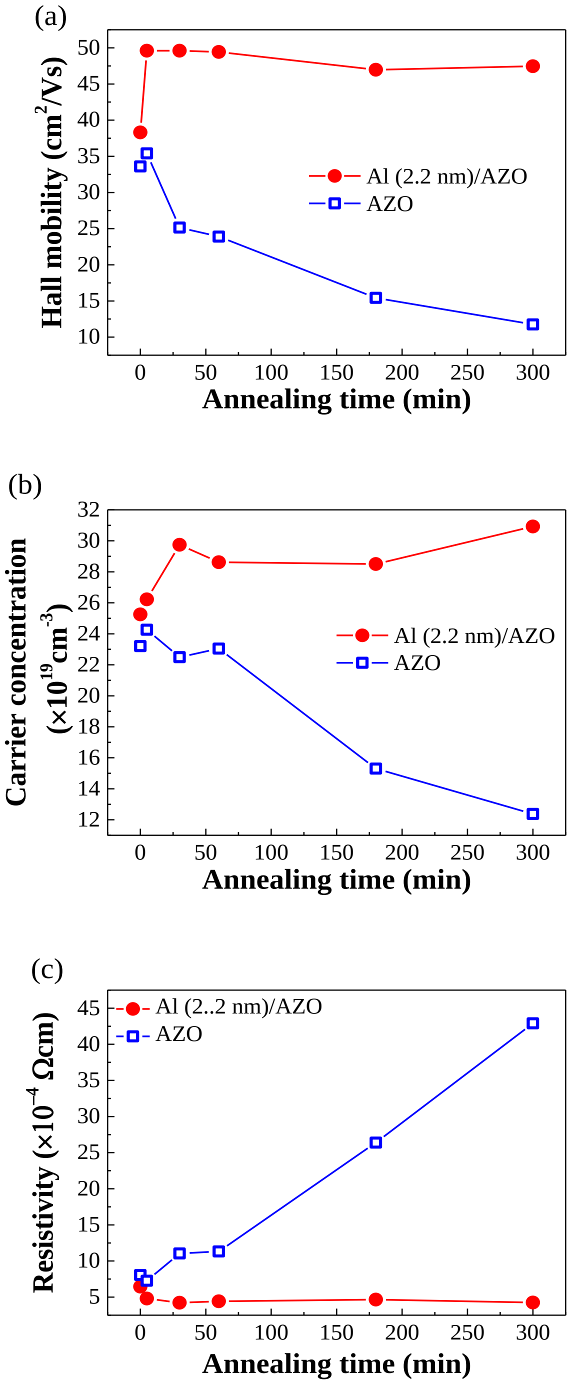

Fig. 4. 12. Evolution of Hall mobility (a), carrier concentration (b) and resistivity (c) of AZO and Al (2.2 nm)/AZO (T_S = 300 °C) with annealing time in N_2 at 400 °C

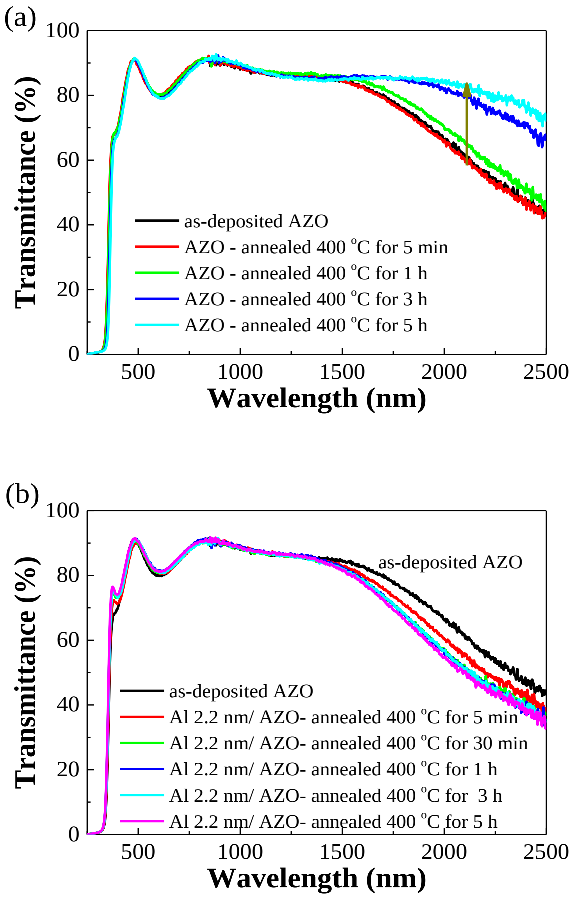

Fig. 4. 13. Evolution of transmission spectra of AZO (a) and Al (2.1 nm)/AZO (T_S = 300 °C) (b) with annealing time in N_2 gas at 400 °C.

As shown above, using ultrathin Al capping layer on AZO samples deposited at T_S of 250 – 300 °C can greatly improve thermal stability of AZO samples. Moreover, their electrical conductivity was improved by annealing in N_2. There are two possibilities that account for this improvement. One possibility is the interdiffusion of Al and Zn. Once Zn atoms in the lattice desorb, they leave their positions as V_{Zn}. Then, Al atoms from capping layer occupy these positions of desorbed Zn atoms and passivate them, preventing the degradation of electrical properties. Al atoms may also migrate into AZO to be Al interstitials (Al_i) and act as shallow donors. If this possibility of Al migration dominated in the improvement of the thermal stability, the samples would exhibit a reduction in electrical properties after Al metal is consumed and the film become transparent. However, our results for high annealing temperature, 500 °C and

600 °C, did not show a reduction in the electrical properties. In addition, Al (2.2 nm)/AZO (T_S = 300 °C) sample also did not show the degradation of electrical properties with long annealing time, while electrical conductivity of AZO sample continuously decreased with annealing time. Moreover, at annealing of 400 °C, we did not obtain noticeable interdiffusion of atoms via XPS measurement. Therefore, the possibility of Al migration into AZO films as Al_i or substitution for desorbed Zn atoms may not be the main mechanism for the improvement in the electrical conductivity of AZO film and their thermal stability.

Instead, the improvements might be dominated by the passivation effect of the Al capping layer, which was dominated by oxidized state. This top layer may passivate the defects near the surface of AZO. During annealing process, some of Al atoms could diffuse into some initial defects along the GBs and passivate them. The movement and the desorption of atoms in the lattice are favored by large number of defects and vacancies. Once the defects and vacancies are passivated, the diffusion and desorption paths will be blocked. Therefore, Zn desorption may be passivated, and the segregation of defects at the GBs caused by Zn desorption is also prevented. Accordingly, carrier concentration can be remained and reduction in Hall mobility can be lowered.

Fig. 4.14 shows the TDS spectra of Zn (M/Z = 64) from Al (2.2 nm)/AZO samples, in comparison with TDS spectra of Zn from AZO samples. As seen in Fig. 4.14, for all Al (2.2 nm)/AZO sample, the Zn desorption was almost passivated. The desorption peak was reduced significantly, and seem to be shifted to a higher temperature, corresponding to a higher desorption energy. This result supports for the aforementioned mechanism very well. The suppression of Zn desorption also agrees well with the evolution of carrier concentration of Al/AZO films. As discussed in section 4.1, Zn desorption may account for the decrease in carrier concentration and steep reduction of Hall mobility of AZO samples after annealing from 400 °C. In Al (2.2 nm)/AZO samples, Zn desorption was suppressed, and their carrier concentration was remained, accompanied with increase in Hall mobility of samples with high T_S of 250 -300 °C and lower reduction in Hall mobility of sample with low T_S of 200 °C.

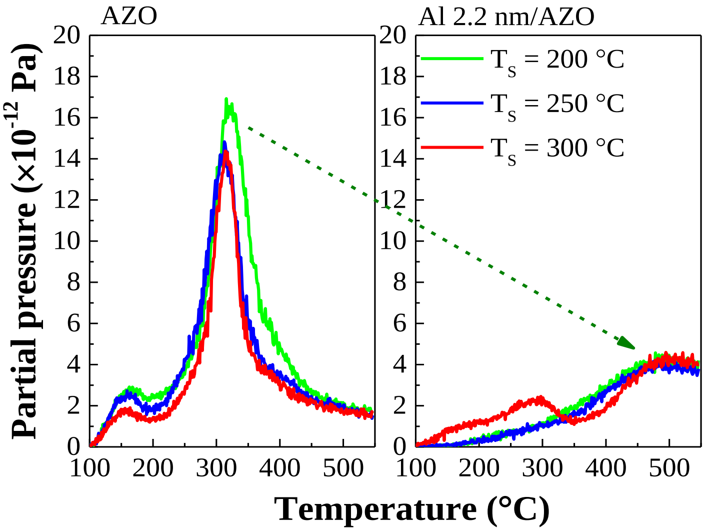

Fig. 4. 14. TDS spectra of Zn (M/Z = 64) from Al (2.2 nm)/AZO samples in comparison with those of AZO samples.

Although the Zn desorption was identically passivated and high carrier concentration was similarly retained in Al (2.2 nm)/AZO samples with every T_S, the Hall mobility of Al (2.2 nm)/AZO samples with T_S of 200 °C still degraded under annealing. The calculated μ_{opt} and μ_{opt}/μ_{GB} ratios of Al (2.2 nm)/AZO samples are presented in Fig. 4.15 (a) and Fig. 4.15 (b), respectively. The optical mobility μ_{opt} of all Al (2.2 nm)/AZO samples were quite comparable, and also increased with T_A, like in AZO samples. However, the μ_{opt}/μ_{GB} ratios of Al (2.2 nm)/AZO samples after annealing were much lower than those of AZO samples. The μ_{opt}/μ_{GB} ratio of Al (2.2 nm)/AZO sample with T_S of 300 °C was small, ~ 0.1-0.2, and remained after annealing. The μ_{opt}/μ_{GB} ratio of Al (2.2 nm)/AZO sample with T_S of 250 °C was little bit larger than that in sample with T_S of 300 °C. It was ~0.9 in as-deposited film and reduced to 0.4 after annealing at low T_A up to 400 °C. Afterward, it slightly increased with higher T_A (450 – 500 °C), but remained lower than 0.9. Different from these two samples, the μ_{opt}/μ_{GB} ratio of Al (2.2 nm)/AZO sample with T_S of 200 °C gradually increased with T_A, although the

μ_{opt}/μ_{GB} ratio was significantly lower than that in annealed AZO sample, for T$_A$ from 400 °C. For instance, μ_{opt}/μ_{GB} ratio was ~2.75 in Al (2.2 nm)/AZO sample compared to ~11 in bare AZO sample at T$_A$ of 400 °C. The lower μ_{opt}/μ_{GB} ratios in annealed Al (2.2 nm)/AZO samples compared to those in annealed AZO samples might be due to Zn desorption passivation. The Zn desorption might induce an increase in number of defects at GBs, thus, raised the GBs potential and increased GBs scattering. Once the Zn desorption was passivated in Al (2.2 nm)/AZO samples, the contribution of Zn desorption to the increment in GBs scattering was eliminated. Therefore, Hall mobility could be remained higher in annealed Al (2.2 nm)/AZO samples compared to that in annealed AZO samples.

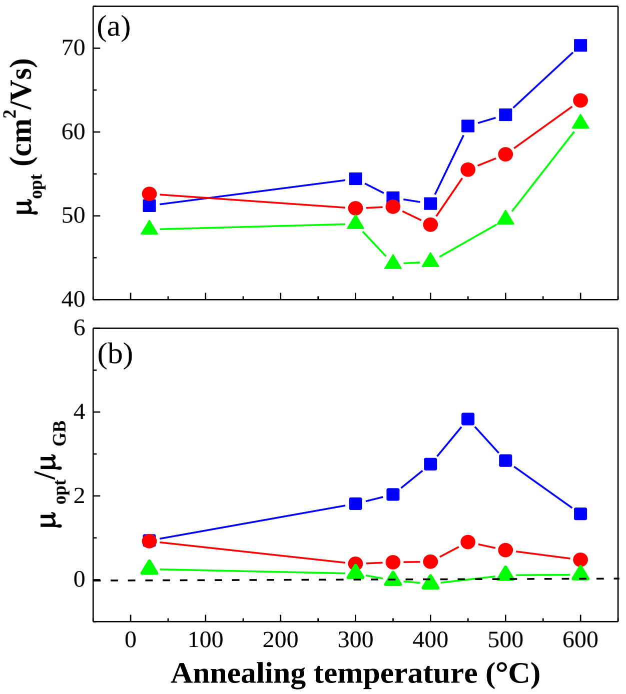

Fig. 4. 15. Evolution of optical mobility μ_{opt} (a) and contribution of GBs scattering (μ_{opt}/μ_{GB}) (b) of Al (2.2 nm)/AZO samples with annealing temperature in N$_2$ gas.

Despite of lower μ_{opt}/μ_{GB} ratios at T$_A$ higher than 400 °C in Al (2.2 nm)/AZO sample with T$_S$ of 200 °C compared with those in bare AZO sample, the increment of μ_{opt}/μ_{GB} ratio in Al (2.2 nm)/AZO sample with T$_S$ of 200 °C from T$_A$ of 300 °C, like in AZO sample, was observed. A slight increase in μ_{opt}/μ_{GB} ratio was also observed in Al (2.2 nm)/AZO sample with T_S of 250 °C at T_A of 450 -500 °C. These results might suggest other segregation of defects to GBs beside the segregation induced by Zn desorption. This segregation might depend on the T_S, which occurred at lower T_A in sample deposited at lower T_S, and hardly be passivated by ultrathin Al film. Therefore, reduction in Hall mobility was still observed in Al (2.2 nm)/AZO sample with low T_S of 200 °C. It should be mentioned that even the low μ_{opt}/μ_{GB} ratios in Al (2.2 nm)/AZO samples with T_S of 250 and 300 °C were almost remained, the μ_{opt}/μ_{GB} ratios in sample with T_S of 250 °C were always higher than those in sample with T_S of 300 °C, implying that the contribution of domain alignment was retained and could not be passivated. Accordingly, even though the Hall mobility in these two samples was not degraded by annealing, the Hall mobility of Al (2.2 nm)/AZO samples with T_S of 250 °C was always lower than that in sample with T_S of 300 °C.

4.3. Effect of Al film thickness on thermal stability of opto-electrical properties of Al/AZO samples

In previous section, effect of ultrathin Al film (2.2 nm-thick) has been found to increase electrical conductivity and its thermal stability of AZO samples which have good *c*-axis orientation. In this section, effect of Al film thickness on thermal stability of electrical properties of AZO film which was deposited at T_S = 300 °C will be discussed.

Fig. 4.16 shows the plan view of SEM images of Al films with the thickness of 4.4 – 8.7 nm on AZO samples. As shown in this figure, the Al film with thickness of 4.4 nm has started growing into clusters. For thicker Al films, the Al clusters were larger, and merged together to form continuous film. Therefore, in as-deposited Al/AZO samples with thick Al film, the resistivity was much lower than as-deposited AZO film, due to conduction of top Al film. For thin Al film (2.2 – 6.5 nm), the Al film was discontinuous islands, the influence of top Al film to the electrical properties characterized by Hall measurement was negligible. The resistivity and the sheet resistance of as-deposited Al/AZO samples with different Al thicknesses was presented in table 4.2.

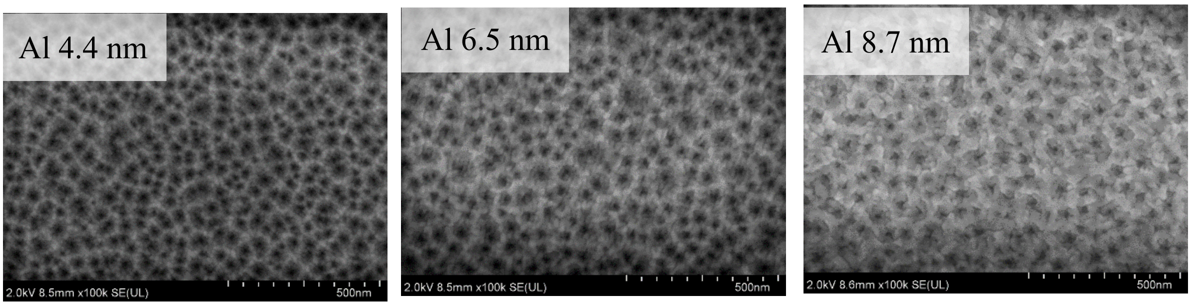

Fig. 4. 16. Plane-view FE-SEM images of Al films with different thicknesses on AZO layer.

Table 4. 2. Resistivity of as-deposited Al/AZO samples with different Al thicknesses

Al thickness (nm)	**Resistivity (×10^{-4} Ωcm)**	**Sheet resistance (Ω/sq)**
0	7.4 ± 0.7	29.8 ± 3
2.2	6.7 ± 0.7	26.7 ± 3
4.4	7.2 ± 0.7	28.3 ± 3
6.5	6.6 ± 0.7	25.8 ± 3
8.7	4.7 ± 0.5	18 ± 2
10.8	3.4 ± 0.3	13 ± 1

As shown in section 4.2, Al (2.2 nm)/AZO sample, after exposing to the air, Al layer was naturally oxidized, and the film was dominated by AlO_x state without any Al metal peak observed by XPS. For thicker Al film, Al metal was remained, as shown in Fig. 4.17, therefore, the as-deposited Al/AZO samples exhibited low transmittance in Vis range, compared to as-deposited AZO samples.

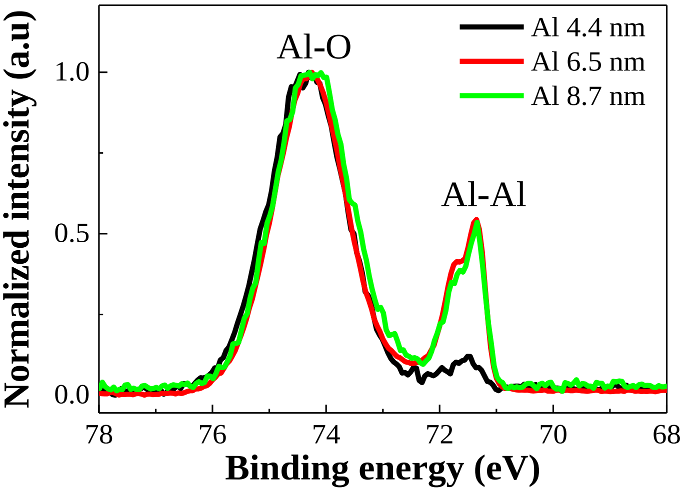

Fig. 4. 17. Normalized SXPS spectra of Al 2p core electrons of Al/AZO samples characterized using Al Kα X-rays.

Fig. 4.18 show the evolution of resistivity of Al/AZO samples with different Al thicknesses (2.2 to 10.8 nm). As shown in this figure, the resistivity of all Al/AZO samples are quite similar, and remained low even with high annealing temperature. The similar resistivity of all the samples, regardless of Al thickness, strongly suggest that the improvement in electrical conductivity of Al/AZO samples are dominated by improvement in electrical conductivity of bottom AZO layer, and not be dominated by the diffusion of Al metal. It is worth noting that, different from the Al (2.2 nm)/AZO samples with no Al metal remained, the remaining of Al metal in as-deposited capping layer may cause the reduction of Zn^{2+} and lead to stronger Zn desorption from lattice site near the interface, as presented in next chapter. However, the substitution of Al to Zn positions can nullify the effect of Zn desorption in Al/AZO samples with thick Al film. Thicker Al film caused the loss of transmittance in Vis range, and it had to be annealed at high temperature to get high transparency as that of as-deposited AZO sample (Fig. 4. 19).

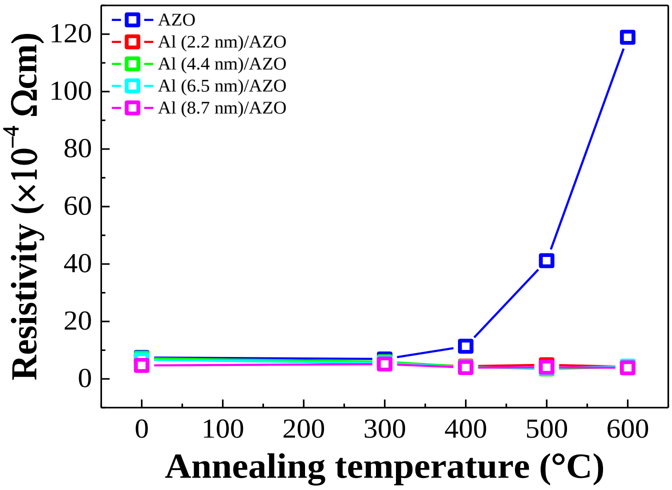

Fig. 4. 18. Evolution of resistivity of Al/AZO sample under annealing in N_2 gas for 1h with different Al thickness (0-8.7 nm).

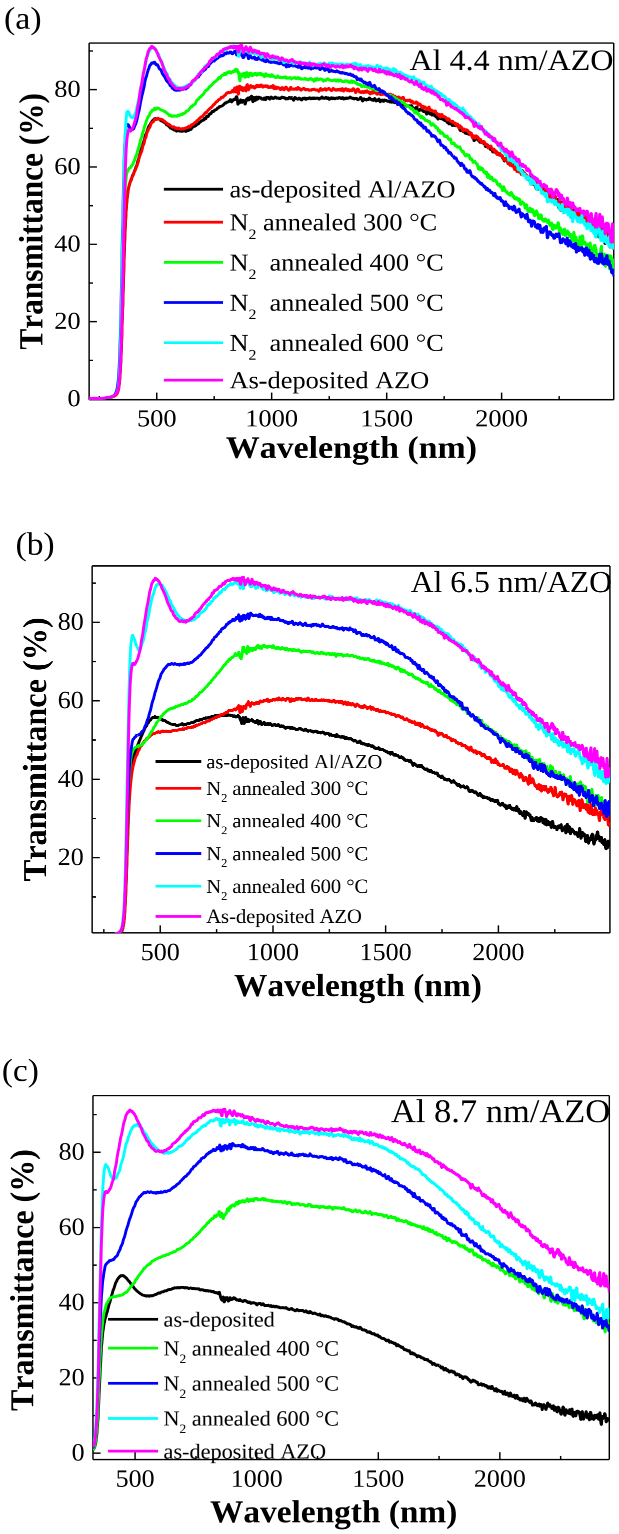

Fig. 4. 19. Evolution of transmission spectra of Al/AZO samples with annealing temperature in N_2 gas for different Al thicknesses.

4.4. Conclusion

In this chapter, we have studied the thermal stability of Al-doped AZO sample under annealing in N_2 gas and its dependence on substrate temperature. The results show that the substrate temperature strongly influenced on crystallinity of the AZO films, especially on the alignment of crystalline domains along the c-axis orientation. For 0.5 wt % Al_2O_3 doping content, the increase in T_S led to improvement in crystallinity, and therefore, improved thermal stability of electrical properties, especially thermal stability of Hall mobility. Our calculation based on Drude model suggested that the optical mobility, or ingrain mobility, was increased by annealing, whereas the scattering at GBs was increased, leading to the reduction of Hall mobility. The Zn desorption under annealing was observed via TDS measurement. This desorption may account for the similar degradation of carrier concentration and the similarly steep reduction in Hall mobility of AZO samples after annealing in N_2 gas with T_A from 400 °C. Using an ultrathin Al capping layer, with the thickness of 2.2 nm, which was dominated by oxidized state of Al, could improve the thermal stability of AZO films. The thermal desorption of Zn was passivated similarly in all Al (2.2 nm)/AZO samples, leading to the maintenance of carrier concentration of all Al (2.2 nm)/AZO samples. An improvement in Hall mobility was obtained in samples deposited at T_S of 250 – 300 °C which have good c-axis orientation, while the reduction in Hall mobility was still observed in sample deposited at lower T_S of 200 °C. Evolution of μ_{opt}/μ_{GB} ratios reveals that the contribution of GBs scattering to the carrier mobility strongly depended on the T_S. The μ_{opt}/μ_{GB} ratio was always higher in AZO samples deposited at lower T_S compared with that in sample deposited at higher T_S, implying the contribution of domains alignment on the GB scattering. The steep increase of GBs scattering in all AZO samples after annealing at 400 °C was due to Zn desorption, while the increase in GBs scattering from quite low T_A of 300 °C in AZO sample deposited at low T_S of 200 °C might suggest another defect segregation to the GBs in this sample. Using ultrathin capping layer, the increasing in GBs scattering induced by Zn desorption was prevented, while other contributions due to crystallinity imperfection, which depends on T_S, could not be passivated. Consequently, the degradation of Hall mobility was passivated in good *c*-axis oriented film, but was still observed in poor *c*-axis oriented sample, which are deposited at low T_S. Significantly high Hall mobility, ~ 49 – 54.4 cm^2/Vs, nearly reached to the theoretical limit, was obtained in Al (2.2 nm)/AZO sample with T_S of 300 °C by annealing in N_2 gas. The similar evolution of electrical conductivity of Al/AZO samples with thicker Al films under annealing in N_2 strongly supports for the enhancement in electrical conductivity of bottom AZO layer itself. Our capped AZO samples, therefore, can be applied in optoelectronic devices and solar cells which require high thermal stability in the manufacturing process. There may be one concern regarding to the resistance of AlO_x layer, which possibly behave as an insulating layer. However, the capping layer was ultrathin, allowing charge carriers to tunnel through it. Electrical measurement was performed on the Al/AZO samples, through AlO_x layer, revealed linear I-V curves, almost identical to the I-V curve measure on AZO layer (see appendix A). This characteristic suggests that such the thin AlO_x capping layer did not prevent the carrier conduction, and the films can be practically used as TEs.

References

[1]. V. L. Kuznetsov, A. T. Vai, M. A. Mamouri, J. S. Abell, M. Pepper, P. P. Edwards, Appl. Phys. Lett., 107 (2015) 232103.

[2]. Q. Li, L. Zhu, Y. Li, X. Zhang, W. Niu, Y. Guo, Z. Ye, J. Alloy. Comp., 697 (2017) 156-160.

[3]. J. C. Lin, M. C. Huang, T. H. Wang, J. N. Wu, Y. T. Tseng, K.C. Peng, Mater. Express., 5 (2015) 153-158.

[4]. K. M. Kang, Y. Wang, M. Kim, H. H. Park, Thin Solid Films, 660 (2018) 913-919.

[5]. R. A. Afre, N. Sharma, M. Sharon, M. Sharon, Rev. Adv. Mater. Sci., 53 (2018) 79-89.

[6]. A. Mallick, D. Basak, Prog. Mater. Sci., 96 (2018) 86-110.

[7]. H. Agura, A. Suzuki, T. Matsushita, T. Aoki, M. Okuda, Thin solid films, 445 (2003) 263-267.

[8]. N. Hirahara, B. Onwona-Agyeman, M. Nakao, Thin Solid Films, 520 (2012) 2123-2127.

[9]. H. L. Tulzo, N. Schneider, D. Lincot, F. Donsanti, Sol. Energy Mater. Sol. Cells, 200 (2019) 109965.

[10]. X. Ji, J. Song, T. Wu, Y. Tian, B. Han, X. Liu, H. Wang, Y. Gui, Y. Ding, Y. Wang, Sol. Energy Mater. Sol. Cells, 190 (2019) 6-11.

[11]. J. Kim, J. Jang, D. S. Lee, J. H. Moon, H. -J. Kim, J. H. Kim, Sol. Energy, 186 (2019) 46-51.

[12]. M. Asemi, M. Ahmadi, M. Ghanaatshoar, Ceram. Int., 44 (2018) 12862-12868.

[13]. J. Nomoto, H. Makino, T. Yamamoto, Thin Solid Films, 644 (2017) 33-40.

[14]. S. Cornelius, M. Vinnichenko, N. Shevchenko, A. Rogozin, A. Kolitsch, W. Möller, Appl. Phys. Lett., 94 (2009) 042103.

[15]. K. Ellmer, R. Mientus, Thin solid films, 516 (2008) 4620-4627.

[16]. H. Tong, Z. Deng, Z. Liu, C. Huang, J. Huang, H. Lan, C. Wang, Y. Cao, Appl. Surf. Sci., 257 (2011) 4906-4911.

[17]. S. Ghosh, A. Mallick, B. Dou, M. F. A. M. van Hest, S. M. Garner, D. Basak, Sol. Energy, 174 (2018) 815-825.

[18]. Z. Zhan, J. Zhang, Q. Zheng, D. Pan, J. Huang, F. Huang, Z. Lin, Cryst. Growth Des., 11 (2011) 21-25.

[19]. V. Anand, A. Sakthivelu, K.D.A. Kumar, S. Valanarasu, A. Kathalingam, V. Ganesh,

M. Shkir, S. AlFaify, I. Yahia, Ceram. Int., 44 (2018) 6730-6738.

[20]. V. Anand, A. Sakthivelu, K. D. A. Kumar, S. Valanarasu, V. Ganesh, M. Shkir, A. Kathalingam, S. AlFaify, Superlattices Microstruct., 123 (2018) 311-322.

[21]. K. Ravichandran, R. Mohan, B. Sakthivel, S. Varadharajaperumal, P. Devendran, T. Alagesan, K. Pandian, Appl. Surf. Sci., 321 (2014) 310-317.

[22]. B. G. Choi, I. H. Kim, D. H. Kim, K. S. Lee, T. S. Lee, B. Cheong, Y. -J. Baik, W. M. Kim, J. Eur. Ceram. Soc., 25 (2005) 2161-2165.

[23]. G. Fang, D. Li, B.L. Yao, Vacuum, 68 (2003) 363-372.

[24]. J. Nomoto, H. Makino, T. Yamamoto, Nanoscale Res. Lett., 11 (2016) 320.

[25]. N. Kumar, A. Dubey, B. Bahrami, S. Venkatesan, Q. Qiao, M. Kumar, App. Surf. Sci., 436 (2018) 477-485.

[26]. M. Mickan, U. Helmersson, D. Horwat, Surf. Coat. Technol., 347 (2018) 245-251.

[27]. J. -P. Niemelä, B. Macco, L. Barraud, A. Descoeudres, N. Badel, M. Despeisse, G. Christmann, S. Nicolay, C. Ballif, W.M. Kessels, Sol. Energy Mater. Sol. Cells, 200 (2019) 109953.

[28]. D. B. Potter, M. J. Powell, I. P. Parkin, C. J. Carmalt, J. Mater. Chem. C, 6 (2018) 588-597.

[29]. K. Zhu, Y. Yang, W. Song, Mater. Lett., 145 (2015) 279-282.

[30]. Z. Pan, X. Tian, G. Hu, C. Xiao, Z. Wei, S. Wu, Z. Li, J. Deng, Mater. Sci. Semicond. Process, 16 (2013) 587-592.

[31]. C. A. Gupta, S. Mangal, U. P. Singh, Appl. Surf. Sci., 288 (2014) 411-415.

[32]. N. M. Le, J. -C. Park, J. Kim, B.-T. Lee, Sol. Energy Mater. Sol. Cells, 198 (2019) 1-4.

[33]. W. -K. Chen, J. -C. Huang, Y. -C. Chen, M. -T. Lee, J. -Y. Juang, J. Alloy. Compd. (2019).

[34]. G. Torrisi, E. Cavaliere, F. Banfi, G. Benetti, R. Raciti, L. Gavioli, A. Terrasi, , Sol. Energy Mater. Sol. Cells, 199 (2019) 114-121.

[35]. H. J. Wang, Y. Y. Zhu, IOP Conf. Ser. Mater. Sci. Eng., 382 (2018) 022054.

[36]. S. Y. Tsai, M. H. Hon, Y. M. Lu, J. Cryst. Growth, 326 (2011) 85-89.

[37]. J. Fan, Z. Li, W. Zhou, Y. Miao, Y. Zhang, J. Hu, G. Shao, Appl. Surf. Sci., 319 (2014) 75-82.

[38]. K. Shen, Z. Bai, Y. Deng, R. Yang, D. Wang, Q. Li, D. Wang, RSC Adv., 6 (2016) 52326-52333.

[39]. I. H. Kim, D. Y. Ku, J. H. Ko, D. Kim, K. S. Lee, J. -H. Jeong, T. S. Lee, B. Cheong,

Y. -J. Baik, W. M. Kim, J. Electroceram, 17 (2006) 241-245.

[40]. J. Montero, C. Guillén, J. Herrero, Thin Solid Films, 519 (2011) 7564-7567.

[41]. N. Formica, D. S. Ghosh, A. Martinez-Otero, T. L. Chen, J. Martorell, V. Pruneri, Appl. Phys. Lett., 103 (2013) 183304.

[42]. T. L. Chen, D. S. Ghosh, D. Krautz, S. Cheylan, V. Pruneri, Appl. Phys. Lett., 99 (2011) 093302.

[43]. Y. -F. Chang, C. -L. Liao, C. -L. Ho, A. -S. Liu, M. -C. Wu, ECS J. Solid State Sci. Technol., 2 (2013) N140-N144.

[44]. F. Ruske, M. Roczen, K. Lee, M. Wimmer, S. Gall, J. Hüpkes, J. Hrunski, B. Rech, J. Appl. Phys., 107 (2010) 013708.

[45]. T. Dimopoulos, G.Z. Radnoczi, Z. E. Horváth, H. Brückl, Thin Solid Films, 520 (2012) 5222-5226.

[46]. M. Wimmer, F. Ruske, S. Scherf, B. Rech, Thin Solid Films, 520 (2012) 4203-4207.

[47]. Y. Yamada, S. Inoue, H. Kikuchi, and S. Funaki, Thin Solid Films, 657 (2018) 50-54.

[48]. J. Huang, R. Tan, Y. Zhang, J. Li, Y. Yang, X. Zhang, W. Song, J. Mater. Sci: Mater Electron, 23 (2012) 356-360.

[49]. F. -H. Wang, C. -L. Chang, Appl. Surf. Sci., 370 (2016) 83-91.

[50]. D. -K. Kim, H. -B. Kim, Superlattices Microstruct., 85 (2015) 50-58.

[51]. Y. M. Hu, J. Y. Li, N. Y. Chen, C. Y. Chen, T. C. Han, C. C. Yu, J. Appl. Phys., 121 (2017) 085302.

[52]. Z. Zhang, C. Bao, W. Yao, S. Ma, L. Zhang, S. Hou, Superlattices Microstruct., 49 (2011) 644-653.

[53]. Y. Kinemuchi, H. Nakano, H. Kaga, S. Tanaka, K. Uematsu, K. Watari, J. Am. Ceram. Soc. , 94 (2011) 2339-2343.

[54]. Y. Sato, J. P. Buban, T. Mizoguchi, N. Shibata, M. Yodogawa, T. Yamamoto, Y. Ikuhara, Phys. Rev. Lett., 97 (2006) 106802.

[55]. F. -J. Haug, Z. Geller, H. Zogg, A. N. Tiwari, C. Vignali, J. Vac. Sci. Technol. A, 19 (2001) 171-174.

[56]. C. Y. Liu, F. He, Y. F. Zhang, S. G. Zang, Y. Zuo, J. R. Ma, Mater.Technol: Adv. Perform. Mater., 30 (2015) 249-256.

[57]. H. C. M. Knoops, B. W. H. van de Loo, S. Smit, M. V. Ponomarev, J. -W. Weber, K. Sharma, W. M. Kessels, M. Creatore, J. Vac. Sci. Technol. A-Vac. Surf., 33 (2015) 021509.

[58]. E. Burstein, Phys. Rev., 93 (1954) 632.

[59]. T. Koida, T. Kaneko, H. Shibata, Materials, 10 (2017) 141.

[60]. H. Makino, Y. Sato, N. Yamamoto, T. Yamamoto, Thin Solid Films, 520 (2011) 1407-1410.

[61]. W. Yang, Z. Wu, Z. Liu, A. Pang, Y. L. Tu, Z. C. Feng, Thin Solid Films, 519 (2010) 31-36.

[62]. T. Kato, K. Sugawara, ACS Omega, 4 (2019) 14714-14720.

[63]. C. Tong, J. Yun, Y. -J. Chen, D. Ji, Q. Gan, W. A. Anderson, ACS Appl. Mater. Interfaces, 8 (2016) 3985-3991.

[64]. H. Fujiwara, M. Kondo, Phys. Rev. B, 71 (2005) 075109.

[65]. L. Nulhakim, H. Makino, J. App. Phys., 119 (2016) 235302

Chapter 5. Improvement of thermal stability of AZO film under annealing in air ambience using thin Al capping layer – Effect of interaction and interdiffusion between Al and AZO layers

As introduced in chapter 4, TCOs should be able to keep their high conductivity and transparency under severe conditions and high temperature stress. Although several types of capping layers have been employed in order to improve the thermal stability of AZO and doped ZnO samples, the effect were insufficient, even thick capping layer, such as 210 nm-thick-ATO, 100 nm-thick-ZTO or 125 nm-thick-Al_2O_3, have been used [1-4]. The electrical conductivity was easily to be degraded under a short duration annealing in air or in oxygen rich environment. Metal stacking layers were also employed in order to improve thermal stability of AZO film, the stability was only reported to 300 °C, nonetheless [5]

In previous chapter, we found that using thin Al film can effectively prevent the degradation of electrical conductivity of AZO sample under annealing in N_2. An improvement in electrical conductivity even was observed. In this chapter, we present the effect of thin Al capping layer on the thermal stability of AZO sample under annealing in ambient air. The effect of oxygen from environment on the degradation of electrical conductivity of AZO layer will be discussed. Ultrathin Al film was found to be able to passivate the degradation of electrical conductivity of AZO layer under annealing in air, but not so effective at high temperature of 500 °C. Using thicker Al capping layers, high electrical conductivity can be kept for a longer duration at annealing temperature of 500 °C in air. The result was found related to the existence of a non-equilibrium layer, which depends on the interaction and interdiffusion between Al capping layer and bottom AZO layer. An Ar plasma was also employed in order to improve thermal stability of Al/AZO sample, owing to the deceleration of interaction and interdiffusion between capping and bottom layer.

In this study, 250 nm-thick AZO (0.5 wt% Al_2O_3) films and Al/AZO films were deposited by magnetron sputtering as presented in chapter 4, with AZO films deposited at the substrate temperature of 300 °C. Thermal stability of AZO and Al/AZO samples with different Al thicknesses (2.2 -10.8 nm) was studied using annealing in air at 300 - 500 °C for 1 h. The evolution of optoelectrical properties with annealing time in air at 500 °C was also studied. The heating rate was 20 °C/min. For further improvement of thermal stability, Al/AZO films were exposed to an Ar plasma in 5 min prior to the annealing. The Ar plasma treatment was operated in a low vacuum chamber (base pressure 5 Pa) with an RF power of 9 W and Ar flowing rate of 10 sccm to obtain a working pressure of 14 Pa. Electrical properties of as-deposited and annealed samples were characterized by Hall measurement with the Van der Pauw method (Nanometrics, HL5500PC). Optical properties of samples were investigated using a spectrophotometer (Hitachi, U-4100) with spectral range of 200 - 2500 nm. Interaction between Al capping layer and AZO layer was evidenced using thermal desorption of Zn, which was monitored using a thermal desorption spectroscopy (ESCO, TDS 1200 II). Chemical states of Al/AZO samples were investigated using a hard X-ray photoelectron spectroscopy (HAXPES) using a custom-made XPS system equipped with a monochromatic Cr Kα (photon energy of 5414.9 eV) X-ray source (ULVAC-PHI) and a wide acceptance angle electron analyzer (Scienta Omicron, EW4000). During the HAXPES measurements, charging on the surface was neutralized by simultaneous irradiation of a low-energy electron beam and a low-energy Ar ion beam (ULVAC-PHI).

5.1. Thermal stability of AZO samples under annealing in air environment – passivation effect of an ultrathin Al capping layer.

Thermal stability of electrical properties of AZO sample under annealing in air was presented in Fig. 5.1. In this figure, the evolution of electrical properties of AZO sample under annealing in N_2 was inserted to evaluate the effect of oxygen from air environment. As shown in Fig. 5.1, both Hall mobility and carrier concentration of AZO sample did not show the degradation under annealing in air at temperature of 300 °C for 1h. This is similar with annealing in N_2 gas. This implies that at annealing temperature of 300 °C, the degradation has not occurred. For higher annealing temperatures, the Hall mobility and carrier concentration drastically decreased, much stronger than degradation observed after annealing in N_2 gas. At annealing temperature of 400 °C, the Hall mobility of AZO samples decreased from ~ 34 ± 0.7 cm^2/Vs in as-deposited sample to ~ 5.2 cm^2/Vs and carrier concentration decrease from ~ 2.4×10^{20} cm^{-3} to ~ 2.9×10^{19} cm^{-3}, leading to the steep increase in resistivity by two order of magnitude, from ~ 7.7×10^{-4} Ωcm to ~ 4.1×10^{-2} Ωcm. Whereas, for annealing in N_2 at 400 °C , the Hall mobility only reduced to ~ 23.9 cm^2/Vs and carrier concentration reduced to ~ 2.3×10^{20} cm^{-3}. Stronger degradation in carrier concentration was observed with annealing at 500 °C in air, to ~ 5.6×10^{18} cm^{-3}. These results suggest a strong influence of oxygen from the environment. The excess of oxygen atom that migrating from environment to AZO layer might bond with Al_i, Zn_i, occupy the interstitial positions, and the adsorption site at GBs [1, 3]. These oxygen atoms will act as acceptors, leading to the decrease in carrier concentration and Hall mobility. O atoms also migrate into the V_O, which has been considered as a carrier source in ZnO material, and compensate them. The adsorption of oxygen at GBs can increase the space-charged region at GBs, and then, increase the GBs potential barrier, resulting in the increase in charge scattering at the GBs [1, 6, 7]. As a result, combining with the effect of desorption and segregation as in case of annealing in N_2, the degradation of electrical conductivity under annealing in air environment was more severe than annealing in N_2 gas.

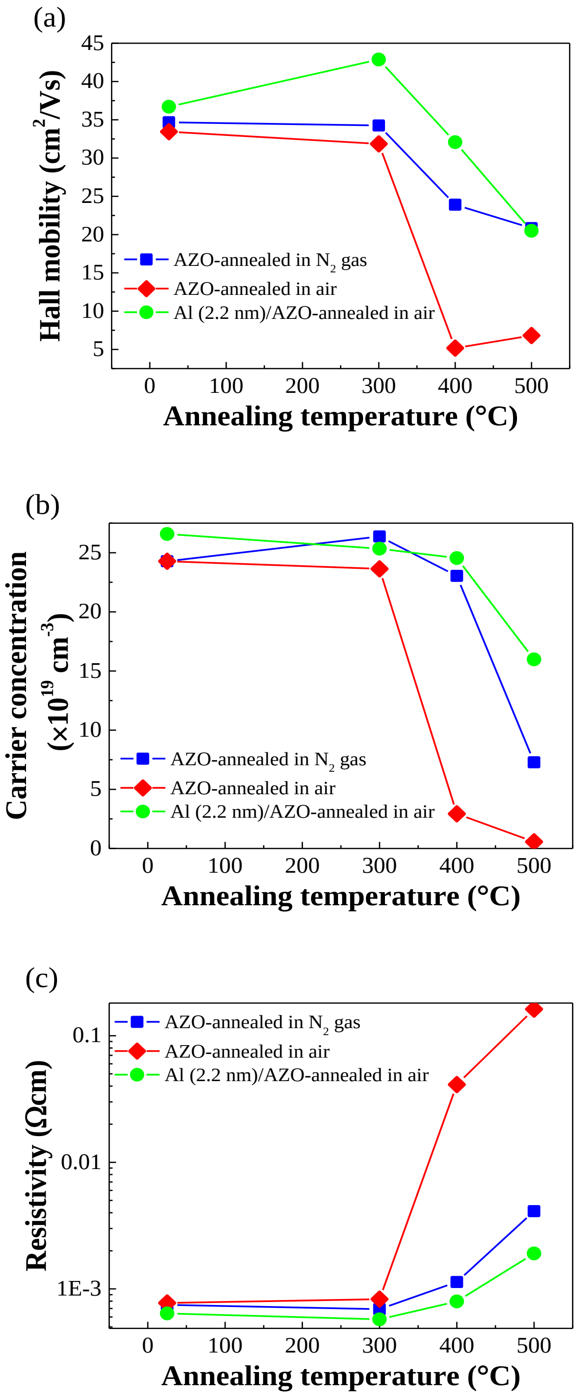

Fig. 5. 1. Evolution of Hall mobility (a), carrier concentration (b) and resistivity (c) of AZO and Al (2.2 nm)/AZO samples under annealing in air environment, in comparison with evolution of electrical properties of AZO sample under annealing in N_2.

The effect of oxygen from air environment on the electrical properties of AZO sample can be reflected through the change in the transmission spectra. As shown in Fig. 5.2 (a), the AZO sample annealed in air environment showed a strong increase in the transmittance in the

NIR range. This increase was significantly stronger than increase in transmittance of AZO sample annealed in N_2 gas. Simultaneously, the red-shift of absorption band edge was larger (Fig. 5. 2(b)). These changes in transmission spectra of AZO sample annealed in air were attributed to the strong reduction of carrier concentration. This reduction was much larger than reduction in sample annealed in N_2 gas.

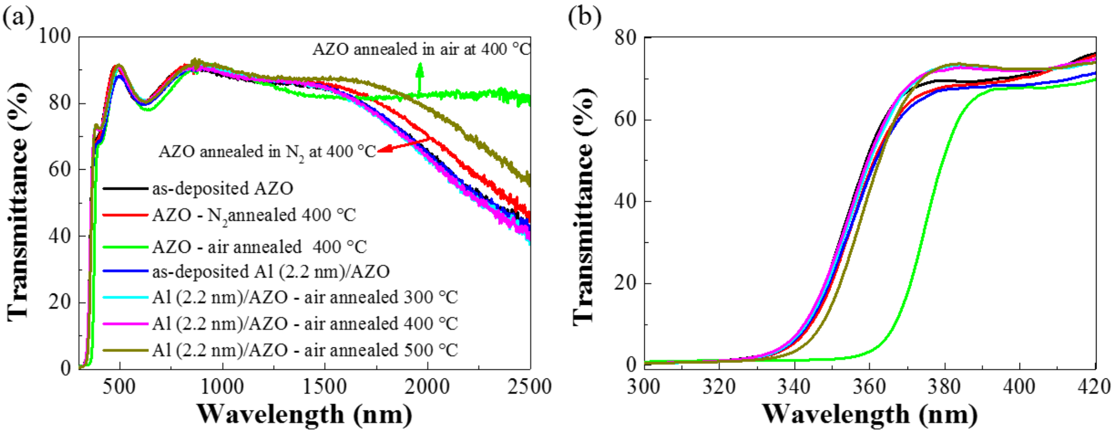

Fig. 5. 2. Transmission spectra of AZO sample annealed in air and in N_2 for 1 h, in comparison with transmission spectra of Al (2.2 nm)/AZO sample under annealing in air (a) and the magnification view of absorption band edge in transmission spectra (b).

Effects of ultrathin Al (2.2 nm-thick) capping layer on thermal stability of optoelectrical properties of AZO samples under annealing in air were also presented in Fig. 5.1 and Fig. 5.2. As depicted in Fig. 5.1, sample Al(2.2nm)/AZO showed a slight increase in Hall mobility at annealing temperature of 300 °C for 1h, while its carrier concentration did not change. For higher annealing temperature, 400 °C, the Hall mobility and carrier concentration decreased slightly, but remained high, at ~ 32 cm^2/Vs and ~ 2.45 $\times 10^{20}$ cm^{-3}, respectively. The obvious reductions in Hall mobility and carrier concentration were observed with annealing temperature of 500 °C, to the values of ~ 20.5 cm^2/Vs and ~ 1.6 $\times 10^{20}$ cm^{-3}, respectively, resulting in the increase in resistivity. However, the decreases in Hall mobility and carrier concentration were significantly smaller than those of bare AZO film. This implies that ultrathin Al film can partly prevent the degradation of electrical properties of AZO layer annealing in air. The passivation was quite effective for the annealing at 400 °C, but not enough for higher annealing temperature at 500 °C in air. Supporting very well for the evolution of electrical properties characterized using Hall measurement, the transmission spectra of Al (2.2 nm)/AZO did not show the increase in transmittance in NIR range with annealing temperature lower than 400 °C. A slight increase in transmittance in NIR range was observed for annealing at 500 °C, and the absorption band edge slightly shifted to longer wavelength. But these changes were significantly smaller than those in bare AZO sample.

5.2. Effect of Al thickness on evolution of electrical and optical properties of Al capped AZO samples under annealing in air ambience.

As mentioned in section 5.1 that ultrathin Al (2.2 nm-thick) can prevent the degradation of electrical properties of AZO layer at annealing temperatures up to 400 °C, but it was not so effective to prevent the degradation at temperature of 500 °C. Therefore, we employed slightly thicker Al films as capping layer to investigate their ability to improve the thermal stability of AZO layer under annealing at 500 °C. Fig. 5.3 (a) shows the effect of Al film thickness on the resistivity of Al/AZO samples under annealing in air at 500 °C for 1 h. It has been presented in section 5.1 that the resistivity of bare AZO sample was drastically increased by annealing in air. At 500 °C, its resistivity increased by three orders of magnitude, from ~ 7.7×10^{-4} Ωcm to ~ 0.2 Ωcm, due to reduction in both Hall mobility and carrier concentration, from ~ 34 cm^2/Vs to ~ 6.2 cm^2/Vs and from ~ 2.4×10^{20} cm^{-3} to ~ 5.0×10^{18} cm^{-3}, respectively. For Al/AZO samples, after annealing in air for 1 h, the resistivity of sample with thin Al films (2.2 – 6.5 nm) increased, although the increase was significantly lower than increase in resistivity of bare AZO sample. Their Hall mobility and carrier concentration were lower than those in as-deposited AZO sample. For samples with thicker Al film (8.7 nm and 10.8 nm), no increase in resistivity was observed. High Hall mobility of ~ 44-48 cm^2/Vs was observed after annealing. This implies that thick Al capping layer can prevent the thermal degradation of electrical properties of bottom

AZO layer under annealing in oxidizing environment.

The transmission spectra of Al/AZO samples after annealing in air at 500 °C for 1 h were presented in Fig. 5.3 (b), in comparison with transmission spectra of as-deposited AZO sample. Compared with the transmission spectra of as-deposited Al/AZO samples, which can be found in Fig. 4.18, chapter 4, we can see that the transmission spectra of all the Al/AZO samples were drastically increased, even though the transmittance of samples with thick Al films (8.7 and 10.8 nm) was remained lower than transmittance of as-deposited AZO sample. The Al/AZO samples with thin Al film (2.2 -6.5 nm) exhibited the transmittance in Vis range comparable to the transmittance of as-deposited AZO film. In the NIR range, the transmittance was raised, due to the reduction of carrier concentration in these samples. The low transmittance in Vis range of samples with thick Al film, together with it low resistivity, might be considered as results of the remained metallic Al layer. However, our following data show the otherwise.

To get insight into the retaining of low resistivity of Al/AZO films, the evolution of the electrical and optical properties of the Al/AZO samples with annealing time at a temperature of 500 °C was studied. The evolution of the electrical properties of Al/AZO films with annealing time was presented in Fig. 5.4. In the Fig. 5.4 (a), the level of resistivity of as-deposited AZO sample was indicated by a dashed line for a reference. It was shown that the resistivity of Al/AZO samples revealed two periods of evolutions. The resistivity firstly decreased, for Al (6.5 nm)/AZO sample, from ~ 7×10^{-4} Ωcm to 4.2×10^{-4} Ωcm, corresponding to a sheet resistance of ~ 16.5 Ω/sq, a Hall mobility of 48 cm^2/Vs and a carrier concentration of 3.1×10^{20} cm^{-3} with the short annealing time of 5 -15 min. Then, the resistivity started increasing with longer annealing time. For samples with thicker Al layers, the low resistivity was retained for a longer annealing time. Their retention time were ~ 2 h for 8.7 nm-thick Al and ~ 7 h for 10.8 nm-thick Al. It can be seen from the Fig. 5.4 (a) that, even the resistivity increased, it occurred at a lower rate compared to that of bare AZO film.

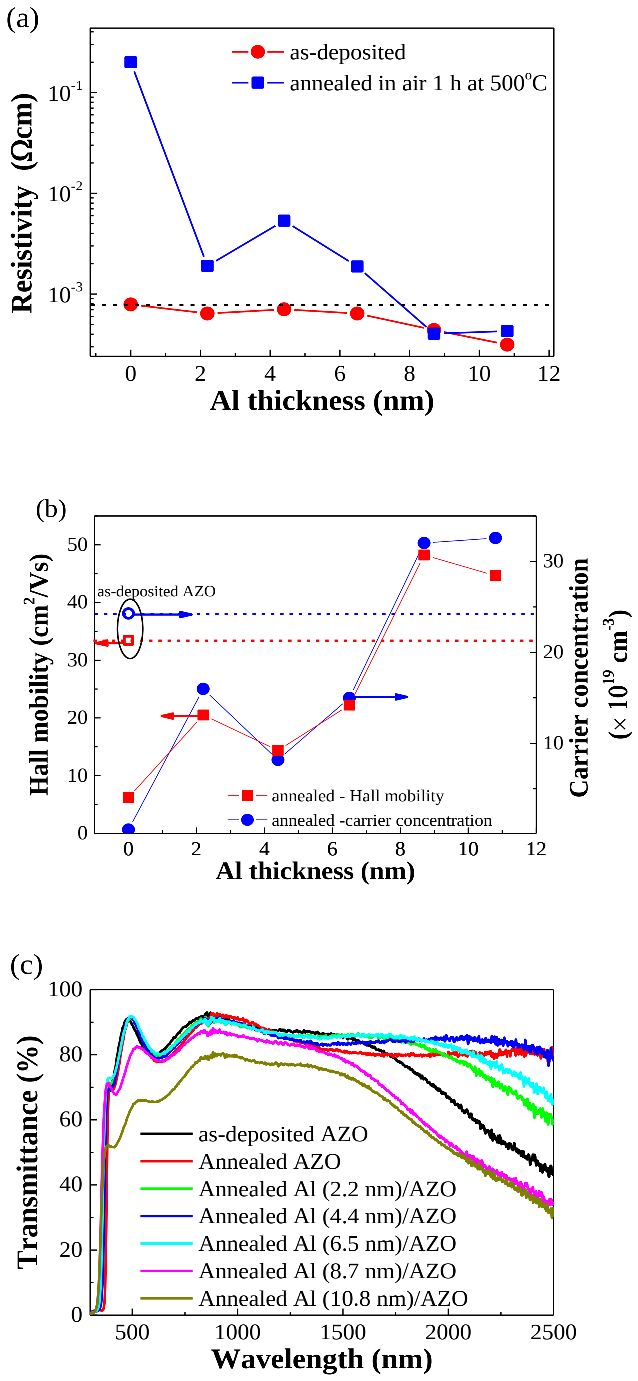

Fig. 5. 3. Effect of Al thickness on variation of resistivity (a), Hall mobility and carrier concentration (b) and transmission spectra (c) of Al/AZO sample under annealing in air at 500 °C for 1 h. The dashed line was inserted in (a) and (b) to indicate the level of as-deposited AZO sample.

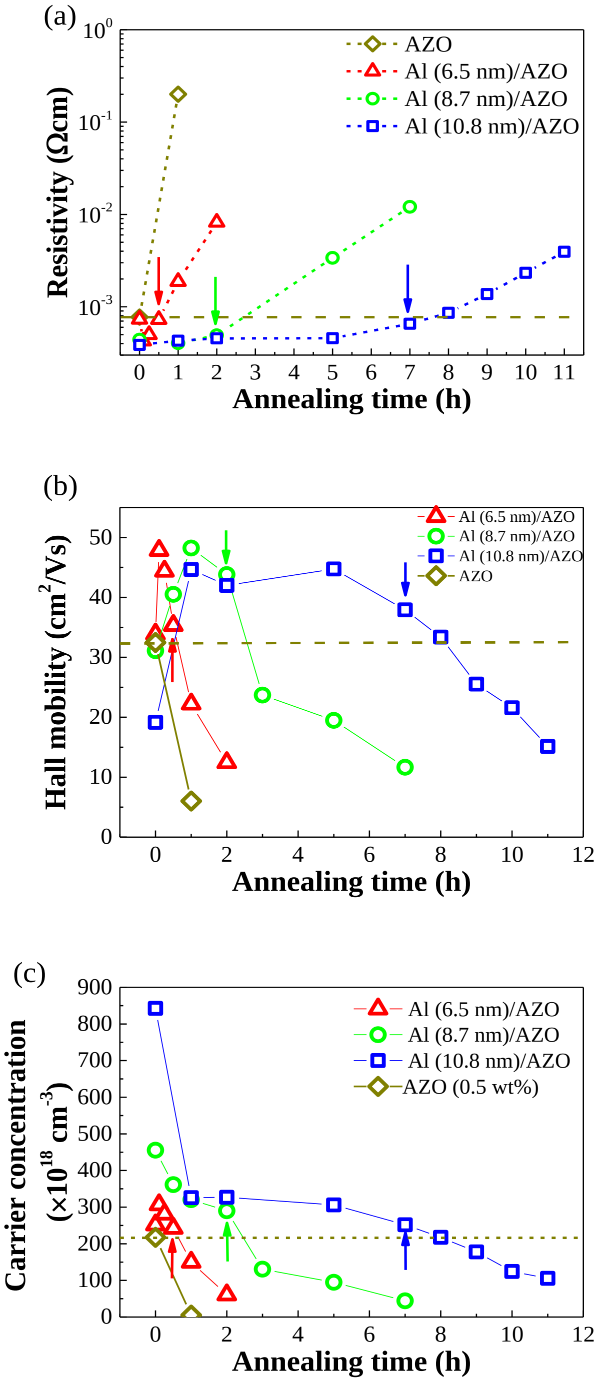

Fig. 5. 4. Evolution of resistivity (a), Hall mobility (b) and carrier concentration (c) of Al/AZO samples with annealing time at 500 °C in air.

Fig. 5.5 shows the evolution of transmission (a), reflection (b) and absorption (c) spectra of the Al (8.7 nm)/AZO film with annealing time at 500 °C in air. The as-deposited Al/AZO films exhibited very low transparency over a wide wavelength range. The low transmittance was due to high reflection and high absorption of as-deposited Al/AZO, as shown in Fig. 3 (b) and (c), respectively. The transmittance of Al/AZO in the Vis region was found to increase sharply after annealing for 30 min, and increased slowly afterwards with increasing annealing time. The sharp increase in transmittance in the Vis range after a short annealing duration was accompanied by a sharp decrease in reflectance to be comparable to the reflectance of as-deposited AZO film. However, high absorption in the Vis range, especially an absorption peak at ~ 450 nm, was observed for longer annealing durations. This absorption in the visible range caused lower transmittance compared to as-deposited AZO film, and thus, resulted in a gradual increase of the transmission. Finally, the absorption in the visible range nearly disappeared after annealing for 2 h, and consequently, the transmittance of Al/AZO in the Vis range equaled that of the as-deposited AZO film.

Similar evolutions were observed in optical spectra of samples with other Al thicknesses, as shown in Fig. 5.6. According to the evolutions of optical spectra of Al/AZO samples, the sample with thicker Al film needed longer annealing time to obtain the high transparency comparable to that of as-deposited AZO film. It was observed that the Al film with thicknesses 6.5 nm, 8.7 nm, and 10.8 nm needed ~ 0.5 h, ~ 2 h, and ~ 7 h, respectively. These characteristic times were indicated by arrows in Fig. 5.4 to compare the evolution of optical properties with electrical properties. It can be observed that there were two regimes of evolution of optoelectrical properties exists, before and after the characteristic time. In the first stage, when the samples had slightly low transparency, the resistivity was very stable around the minimum value, which was lower than that of as-deposited AZO sample. The second stage was from the annealing time when Al/AZO samples got high transparency, which was comparable to transparency of as-deposited AZO sample. In this stage, the electrical properties gradually degraded with further annealing time, but degradation rate was much lower than degradation rate of uncoated AZO sample. In addition, the minimum resistivity of ~ $4 \pm 0.5 \times 10^{-4}$ Ωcm, corresponding to the sheet resistance value of ~16 ± 1 Ω/sq was found to independent of the Al thickness and the darkness of the samples.

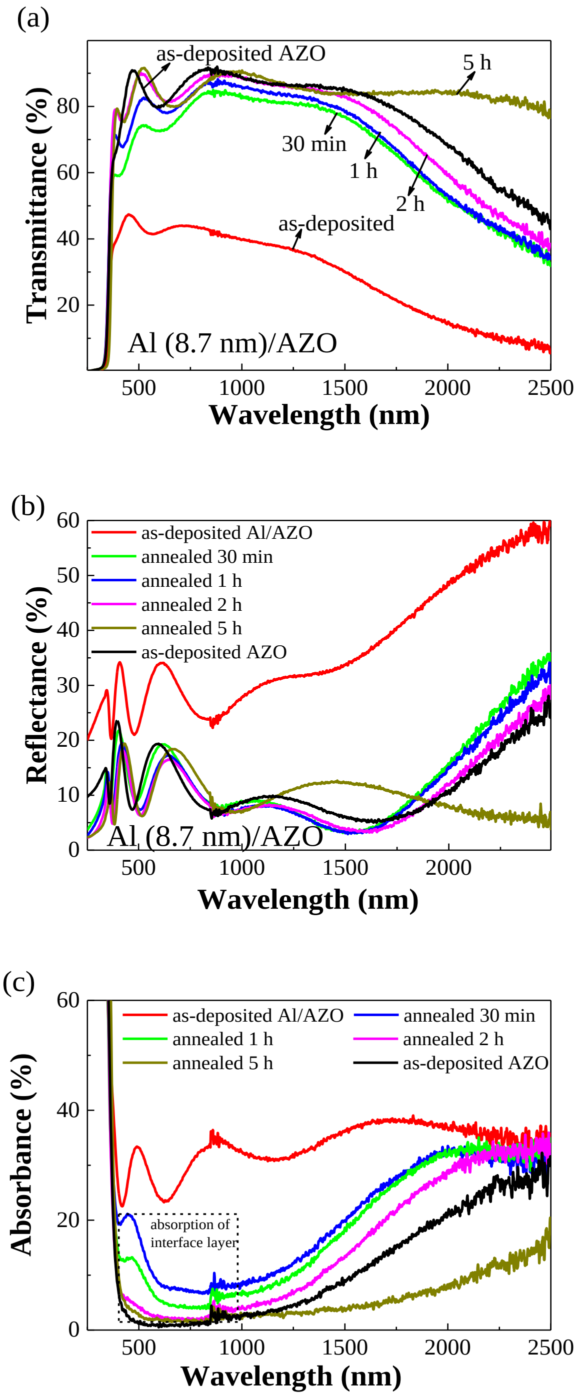

Fig. 5. 5. Evolution of transmission (a), reflection (b) and absorption (c) spectra of Al (8.7nm)/AZO sample with annealing time in air at 500 °C.

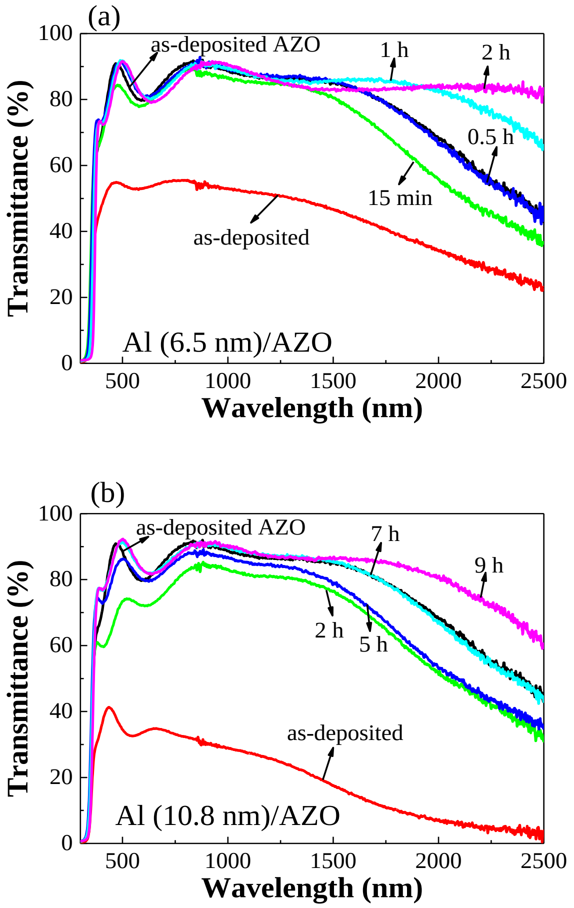

Fig. 5. 6. Evolution of transmission spectra of Al (6.5 nm)/AZO (a), and Al (10.8 nm)/AZO (b) under annealing in air at 500 ºC.

Although the transparency of annealed Al/AZO samples was slightly lower than that of as-deposited AZO samples in the first stage, it was not significantly low to cause reduction in performance of transparent electrode, as shown by Haacke figure of merit (FOM) (see table 5.1) [8]. The annealed Al/AZO samples even showed an improvement in FOM. The FOMs of our samples were comparable to or higher than the FOMs of other multilayers transparent electrode films [2, 5, 9-15].

At the annealing time attaining high transparency as the as-deposited AZO film (indicated by the arrows in Fig. 5.4), the Hall mobility and the carrier concentration of all Al/AZO films were slightly higher than those of the as-deposited AZO film, for example, the

Hall mobility and carrier concentration of Al (8.7 nm)/AZO sample showed 44 cm^2/Vs and 2.9 × 10^{20} cm^{-3}, respectively. These results suggest that the electrical properties of bottom AZO layer could be retained even after the annealing in air. After the Al/AZO reached high transparency, the Hall mobility as well as the carrier concentration decreased slowly with increasing annealing time. The change of carrier concentration can also be confirmed indirectly by the optical spectra. As shown in Fig. 5.5 (a), the spectral shape of transmission spectra in the NIR range was nearly identical with annealing time of 30 min – 2 h. The lower transmittance in the NIR, compared to that of as-deposited AZO sample, was due to higher carrier concentration. The reduction of carrier concentration for longer annealing time, for example, 5h for Al (8.7 nm)/AZO sample, led to the increase of transmittance in NIR.

Table 5. 1. Comparison of sheet resistance (R_S), estimated average transparency (T_{av}) over the Vis range and Haacke figure of merit (FOM) of our Al coated AZO samples with those of other reported multilayer transparent electrodes. FOM = T_{av}^{10}/R_S. The critical point when annealed Al/AZO samples got high transparency as as-deposited AZO sample was marked by asterisk symbol.

Sample		R_S (Ω/sq)	T_{av} (%)	Wavelength range (nm)	FOM (10^{-3} Ω^{-1})	Ref.
As-deposited AZO		**35.5**	**86.8**	400-1200	**6.83**	This work
As-deposited Al 6.5 nm/AZO		28.47	50.6	400-1200	0.039	
Al 6.5 nm/AZO air annealed 500° C	5min	16.54	75.8	400-1200	3.78	
	15 min	19.4	84.1	400-1200	9.12	
	30 min	**28.365**	**86.9**	400-1200	**8.65 ***	
	1 h	73.085	86.4	400-1200	3.17	
As-deposited Al 8.7 nm/AZO		16.99	41.83	400-1200	0.0096	
Al 8.7 nm/AZO air annealed 500° C	30 min	16.45	78.1	400-1200	5.13	
	1 h	15.585	82.3	400-1200	9.14	
	2 h	**18.9**	**86.1**	400-1200	**11.8***	
	5 h	130.75	86.1	400-1200	1.71	
As-deposited Al 10.8 nm/AZO		14.7975	30.5	400-1200	0.00047	
Al 10.8 nm/AZO	1 h	16.42	72.1	400-1200	2.31	

air annealed 500° C	2 h	17.4025	77.8	400-1200	4.67	
	5 h	17.46	84.3	400-1200	10.38	
	7 h	**25**	**87.2**	400-1200	**10.16 ***	
	9 h	52.6	87.4	400-1200	4.94	
ITO/Ag (11.4 nm)/ITO		6.4	73.5	400-1100	7.19	[10]
AZO/AgNps/AZO		34	76	400-800	1.89	[11]
ATO (130)/AZO (600)		33.5	67	400-800	0.544	[2]
ATO (130)/AZO (600) annealed in air at 450 °C for 15 min		100	74	400-800	0.49	
AZO/Au/AZO		30	85	380-750	6.56	[5]
Graphene/Ag nanowires/Graphene		10.8	77.6	400-800	7.33	[12]
Ni/AZO		20	80	375-700	5.37	[9]
SnO_2/APC (10 nm)/SnO_2		10	55.5	400-1200	0.28	[13]
ZnO/AgO_x (8 nm)/ZnO		20	91	400-1000	19.4	[14]
ZnO/Al (20 nm)/ZnO annealed in air at 300 °C for 3 h		155	75	400-700	0.36	[15]

5.3. Inter-diffusion of atoms between Al capping layer and bottom AZO layer

The evolution of electrical and optical properties of Al/AZO samples suggest that the Al capping layer can prevent the thermal degradation of AZO films with two regimes related to the transmittance. To understand about the mechanism behind these evolutions in optoelectrical properties of Al/AZO samples, chemical states of Al/AZO were studied by HAXPES using monochromatic Cr Kα X-rays. The high energy X-rays create photoelectrons with sufficient kinetic energy to escape from the deeper regions inside the sample. For an amorphous Al_2O_3 with bandgap of ~ 7 eV [16] and a high density of ~ 3.97 g/cm^3 [17], estimated inelastic mean free paths (IMFPs) of Al 1s, O 1s, and Zn 2p photoelectrons excited using Cr Kα X-rays are ~ 6.98, 8.5, and 7.78 nm, respectively, based on the TPP-2M formula [18]. Correspondingly, probing depths can be approximately 20.9, 25.5, and 23.3 nm, which were three times that of IMFPs. Due to the large probing depth of HAXPES, the data were expected to contain information from the entire Al film thicknesses. The evolution of HXPS spectra of Al (8.7

nm)/AZO in the Al 1s region, O 1s region, and Zn 2p region with annealing time are displayed in Fig. 5.7 (a), (b), and (c), respectively. The evolution of the integral intensities of each peaks and their relative ratios are plotted in Fig. 5.7 (d). As shown in Fig. 5.7 (a), the Al 1s spectrum of as-deposited Al (8.7 nm)/AZO consisted of two peaks which centered at binding energies of ~ 1559.75 eV and ~ 1562.45 eV, corresponding to the metallic Al and Al oxide (AlO_x) [19], respectively. The appearance of two peaks in the Al 1s spectrum implies that a part of the Al layer in the as-deposited Al/AZO was naturally oxidized.

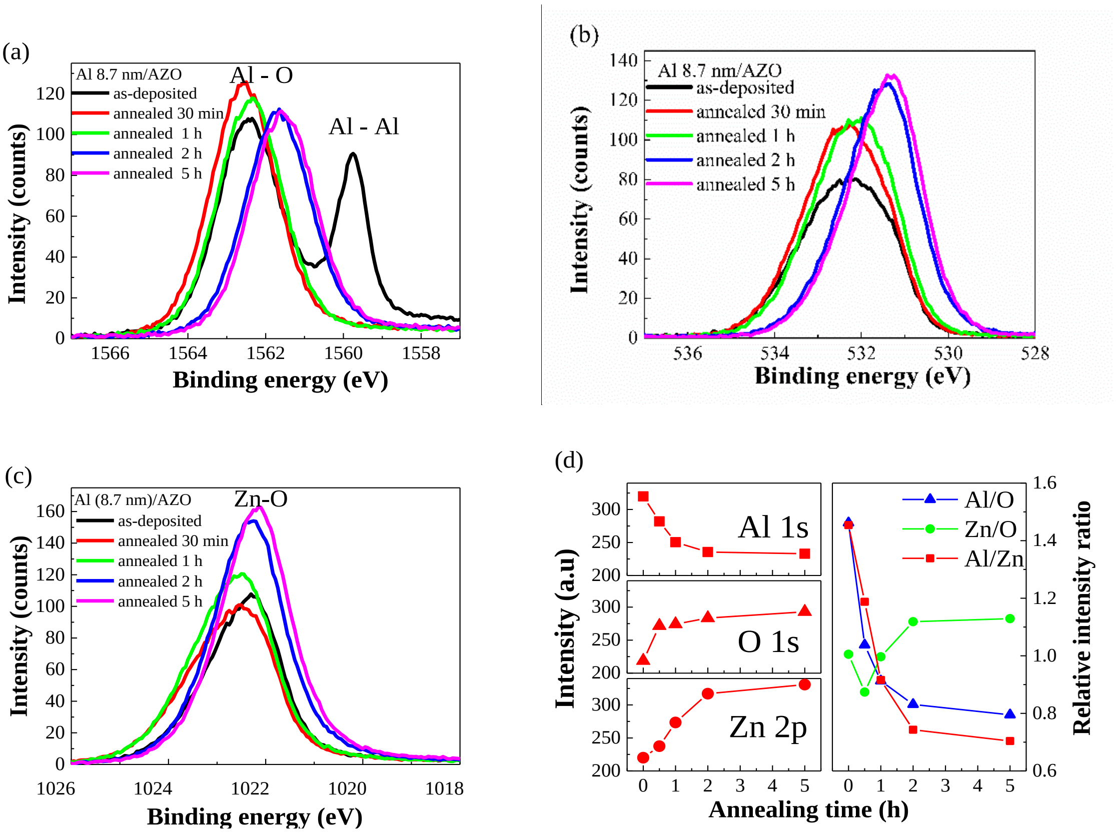

Fig. 5. 7. HAXPES spectra of Al 1s, O 1s, and Zn 2p core levels (a-c), integrated intensities of Al 1s, O 1s, and Zn 2p core levels and their relative ratios (d) of Al (8.7 nm)/AZO samples before and after annealing in air at 500 °C, respectively.

After a short duration of annealing in air, ~ 30 min, the Al 1s spectrum showed only a broad peak of Al-O bonding. No trace of Al metal bonding was observed. Simultaneously, the intensity of O 1s peak increased. These observations suggest the oxidation of Al layer by annealing. For further annealing time, the intensity of Al 1s peak gradually decreased.

Simultaneously, the intensity of Zn 2p was found increased. Subsequently, the intensities of core level spectra almost saturated at the annealing time of 2 h. The annealing time of 2 h corresponded to the time when the sample attained high transparency comparable to the as-deposited AZO (Fig. 5.5 (a)). With this annealing time, the Al-O peak shifted to lower binding energy side, from ~ 1562.4 eV to ~ 1561.6 eV. Additionally, the O 1s peak became narrower and was dominated by lower binding energy component.

The disappearance of metallic Al peak in Al 1s spectrum occurred quickly after annealing confirmed a quick oxidation of Al film. Accordingly, the strong decrease in reflectance (Fig. 5.5 (b)) and the sharp increase in transmittance (Fig. 5.5 (a)) in Vis range after a short annealing duration can be attributed to the disappearance of metallic Al film. The slightly lower transmittance in short time annealed Al/AZO samples was due to optical absorption in the Vis range, with absorption peak around ~ 450 nm. However, such absorption in Vis range did not appeared in annealed Al film coated on glass substrate (Fig. 5.8). Initially, the levels of absorption of as-deposited Al/glass and Al/AZO sample were similar, except the interference fringes in the absorption spectra of Al/AZO sample due to bottom AZO layer. It was shown that a steep reduction in absorbance of Al/glass occurred after annealing only for 5 min. Whereas, the Al/AZO sample showed significantly high absorbance, even with longer annealing time. This result strongly suggests the quick oxidation of Al metal film, and the absorption peak in Vis range is unique in Al/AZO samples.

After annealing, Al 1s intensity decreased while Zn 2p intensity increased. Simultaneously, HAXPES intensity ratios of Al/Zn and Al/O were decreased, and Zn/O ratio increased. These results suggest that the concentration of Zn near the surface increased with annealing time, while Al content decreased, might be due to interdiffusion of constituent elements between capping and bottom layer. According to study of Tong et al. [20], interdiffusion between thick Al film (15 nm) and bottom ZnO layer can slightly occur from annealing temperature of 400 °C and increased with higher annealing temperature. The diffusion depth, characterized by SIMS, from initial interface, was obtained around ~ 20 nm for annealing at 400 °C and ~ 65 nm for annealing at 600 °C. This interdiffusion may resulted in a non-equilibrium interface layer. This process occurred during annealing, up to the characteristic time, which was 2 h for Al 8.7 nm/AZO sample. After that, core level intensities and their relative ratios became saturated, implying an equilibrium state of Al/AZO sample. The HAXPES peaks were almost stable.

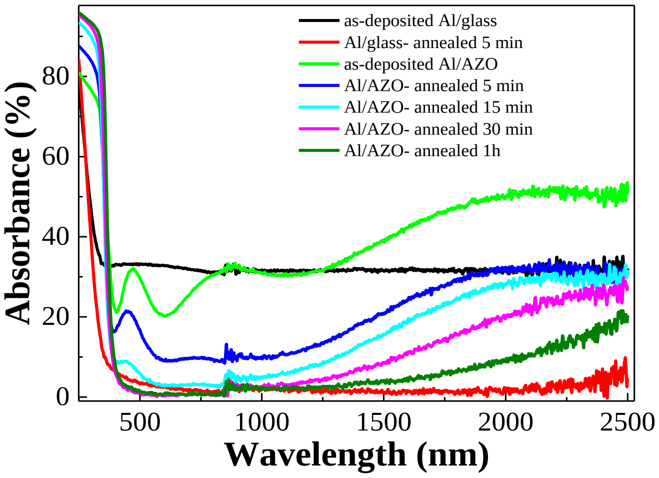

Fig. 5. 8. Evolution of absorption spectra of Al (6.5 nm)/AZO sample under annealing in air at 500 ºC in comparison with single Al metal film (~6.5 nm thick) grown on glass substrate.

It is worth noting that, during annealing time before equilibrium, the absorption peak in Vis range appeared in Al/AZO samples, and their low resistivity was kept. After reaching the equilibrium state, the absorption peak disappeared, the Al/AZO samples became transparent, and their resistivity started to increase. These results suggest a strong correlation between electrical properties, absorption peak in Vis range and the existence of the non-equilibrium interface layer in Al/AZO sample, because of the interdiffusion during annealing. The non-equilibrium layer may capture oxygen from environment, preventing the degradation of bottom AZO layer. A schematic view of interface layer can be presented in Fig. 5.9

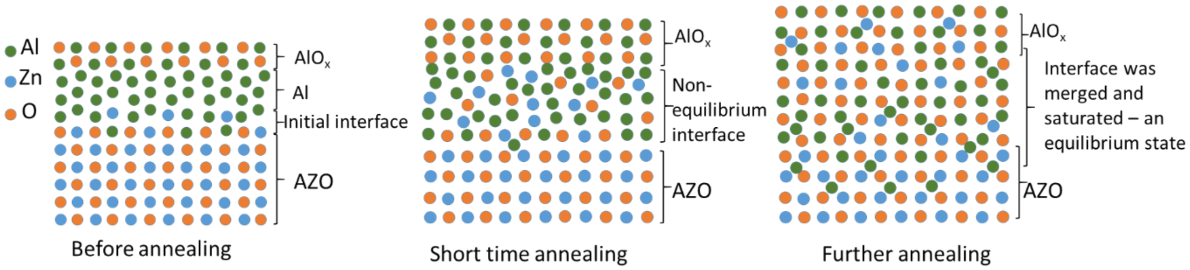

Fig. 5. 9. Schematic view of the interface layer in Al/AZO sample under annealing.

5.4. Effect of Ar plasma treatment on thermal stability of Al/AZO samples – preventions of interaction and interdiffusion

In order to improve thermal stability of Al/AZO sample under annealing in air, we employed Ar plasma treatment in low vacuum chamber. Fig. 5.10 (a) shows the evolution of electrical properties of plasma treated Al/AZO samples with annealing time at 500 °C in air. After plasma treatment, the resistivity of these films did not show noticeable change, due to their good crystallinity and their good electrical properties. The evolutions of electrical properties with annealing time in plasma treated Al/AZO sample were similar to those in untreated Al/AZO samples, except that the retention time was longer. That was ~1 h, ~5 h, and ~14 h, for the Al thickness of 6.5 nm, 8.7 nm, and 10.8 nm, respectively. Fig. 5.10 (b) shows the evolution of transmission spectra of plasma treated Al (8.7 nm)/AZO sample with annealing time. We can see that the transmittance of plasma treated sample was slightly higher than that of the as-deposited film because of an additionally slight oxidation of Al metal film, which can be confirmed using HAXPES of Al 1s as shown in Fig. 5.11 (a). Consistent with the evolution of electrical properties, the evolution of optical spectra of plasma treated samples were similar with the evolution of untreated samples. The reflection of the sample was also reduced quickly. However, it took longer time for plasma treated sample to reach the high transparency in Vis range, due to high absorption retained for longer time (Fig. 5.10 (c)). Once the sample attained high transparency comparable to that of as-deposited AZO film, that is after 5 h of annealing for Al (8.7nm)/AZO sample, the resistivity started to increase, and the transmittance in NIR range increased because of the decrease in carrier concentration.

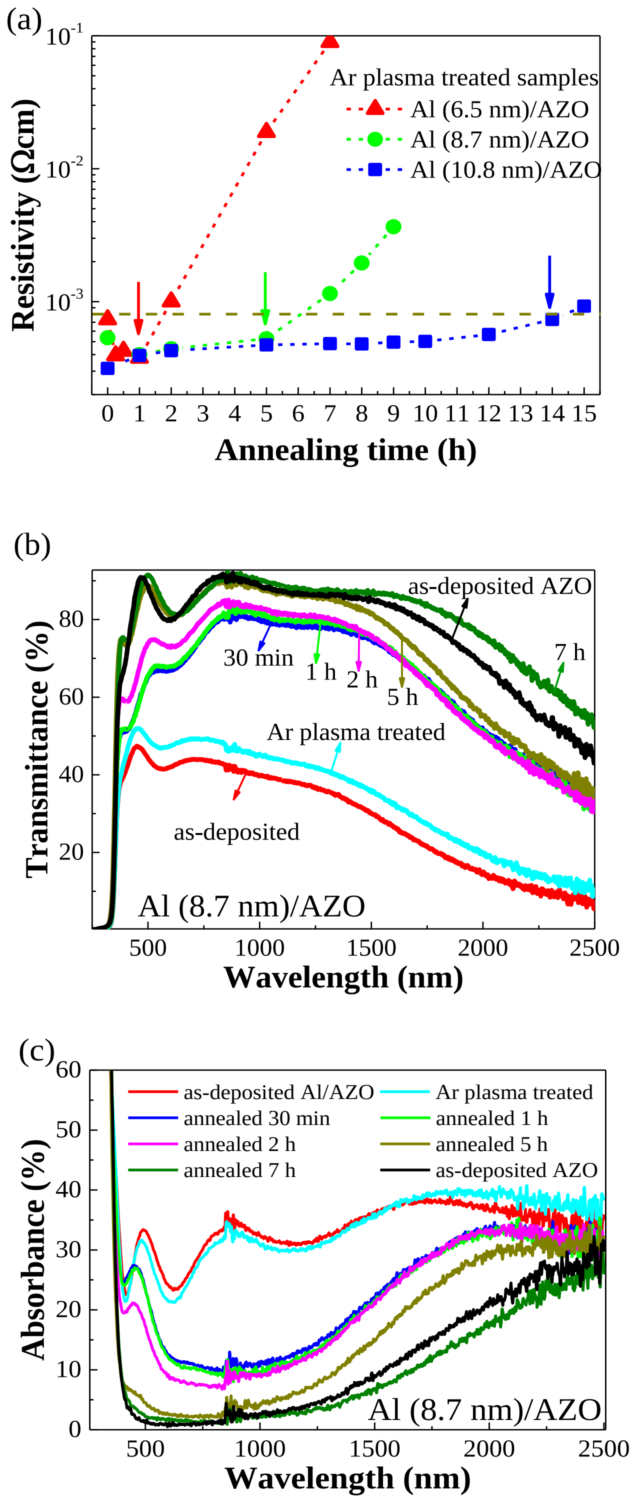

Fig. 5. 10. Evolution of resistivity (a), transmission spectra (b) and absorption spectra of plasma treated Al (8.7 nm)/AZO sample with annealing time in air at 500 °C.

The chemical states of plasma treated Al (8.7 nm)/AZO samples characterized using

HAXPES were presented in Fig. 5.11. The evolutions of HAXPES spectra were consistent with the optical and electrical properties of plasma treated sample. The evolution of HAXPES spectra of plasma treated sample showed the similar changes with the untreated Al/AZO sample, but occurred after longer duration of annealing. An Ar plasma treatment on AZO layer prior to the deposition of top Al layer showed the similar effect with the plasma treatment after deposition of Al layer, as shown in Fig. 5.12. This result suggest that the Ar plasma treatment influenced on the process occurring in bottom AZO layer. Accordingly, the longer existence of non-equilibrium layer by plasma treatment might be attributed to the slowing of the inter-diffusion of atoms.

The interaction and inter-diffusion between top Al capping layer and bottom AZO layer were also investigated by TDS of Zn (M/Z = 64) from Al/AZO samples (Fig. 5.13). It has been suggested that Zn desorption from lattice site occurs around 300 – 400 °C [21, 22], which accounts for the degradation of electrical properties, especially carrier concentration of ZnO thin film. Fig. 5.13 shows that with Al overlayer (thicker than 4 nm), the Zn desorption was promoted. Under thermal excitation, Al atoms migrate into the bottom AZO layer and capture oxygen from Zn-O bonds to form Al-O bonds, and reduce Zn [23, 24]. Then, the reduced Zn atoms will diffuse out. The evolution of Zn desorption with Al thickness implies that more Zn was reduced when thicker Al film was deposited. The desorbed Zn atoms had to diffuse through the coating layer which also acted as a mass-transport barrier, therefore the desorption peak shifted to a higher temperature compared to the desorption peak in the bare AZO film. This observation is in good agreement with the study of Gao et al. [23] about the interaction between Al metal and ZnO. Even though Zn desorption was considered as an origin of the degradation of electrical properties in doped ZnO, the substitution of Al for Zn can nullify this effect. Accordingly, the increase in Zn desorption did not cause a stronger degradation in electrical properties of the Al/AZO sample.

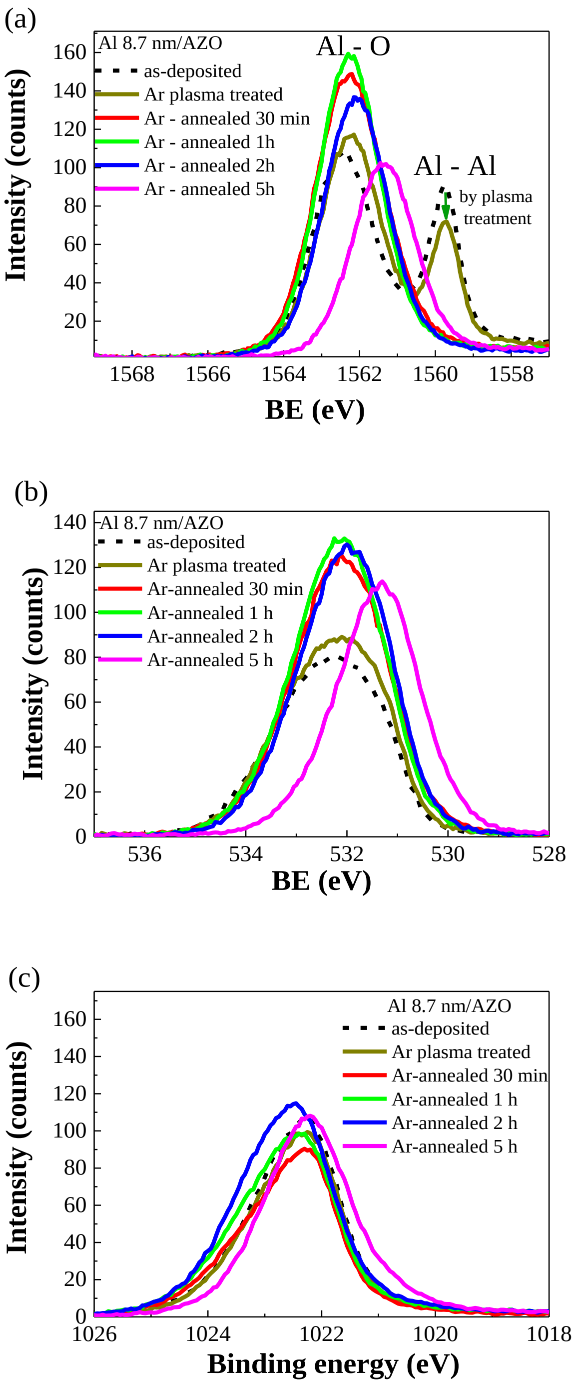

Fig. 5. 11. Evolutions of HAXPES spectra of Al 1s (a), Zn 2p (b), and O 1s (c) of plasma treated Al (8.7 nm)/AZO sample with annealing time in air at 500 °C.

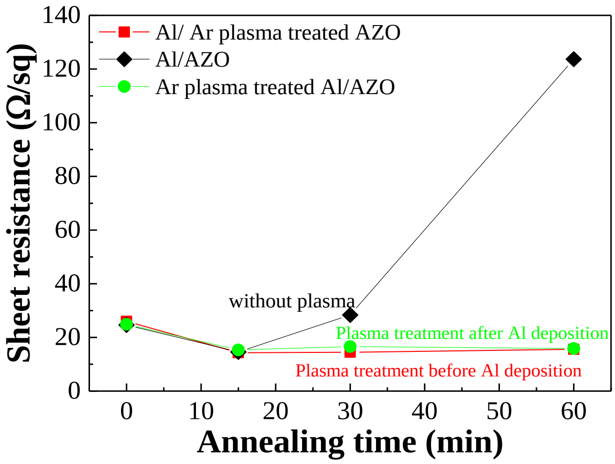

Fig. 5. 12. Comparison of evolution of sheet resistance of untreated, pre-Ar plasma treated and post-Ar plasma treated Al (6.5 nm)/AZO samples under annealing in air at 500 °C.

However, the interaction and interdiffusion between Al metal and bottom AZO layer might determine the existence of the non-equilibrium interface layer. The TDS spectra shows that the intensity of Zn desorption peak was lower in the Ar plasma treated sample. Additionally, the desorption peak was shifted to higher temperature. This observation would imply that the interaction of Al metal and ZnO, and the interdiffusion of Al and Zn were impeded by the Ar plasma treatment. Moreover, the reduction in interdiffusion rate was also revealed by the evolution of relative ratios of Al 1s, Zn 2p and O1s core level intensities with annealing time as shown in Fig. 5.14. The plasma treated sample exhibited higher Al/Zn, Al/O intensity ratios, and lower Zn/O ratio than those in untreated sample. According to study in chapter 3, H was found incorporated into ZnO film by Ar plasma in low vacuum chamber. Hydrogen atoms passivated vacancies and defects along grain boundaries (GBs) [25], thereby passivating the interaction site and blocking diffusion pathway for the interaction and interdiffusion of atoms, and thus, preventing the migration of Al into AZO. As a result, the interaction of Al and ZnO was decelerated and hence, Zn desorption was reduced, and the desorption peak was shifted to a higher temperature. Because the interaction and the interdiffusion between Al and AZO were suppressed, the non-equilibrium layer existed for longer annealing time in sample treated by Ar plasma. Consequently, the low resistance of Ar plasma treated Al/AZO samples was maintained for longer annealing time.

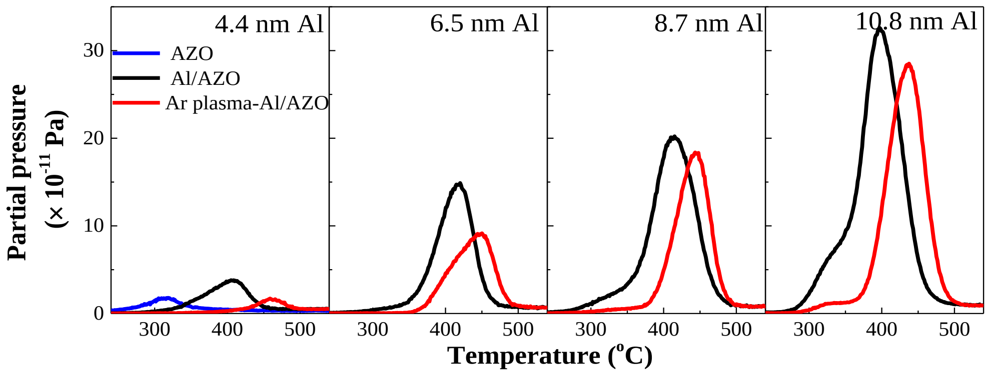

Fig. 5. 13. TDS spectra of Zn (M/Z = 64) from Al/AZO samples with and without Ar plasma treatment in comparison with TDS spectra of AZO film.

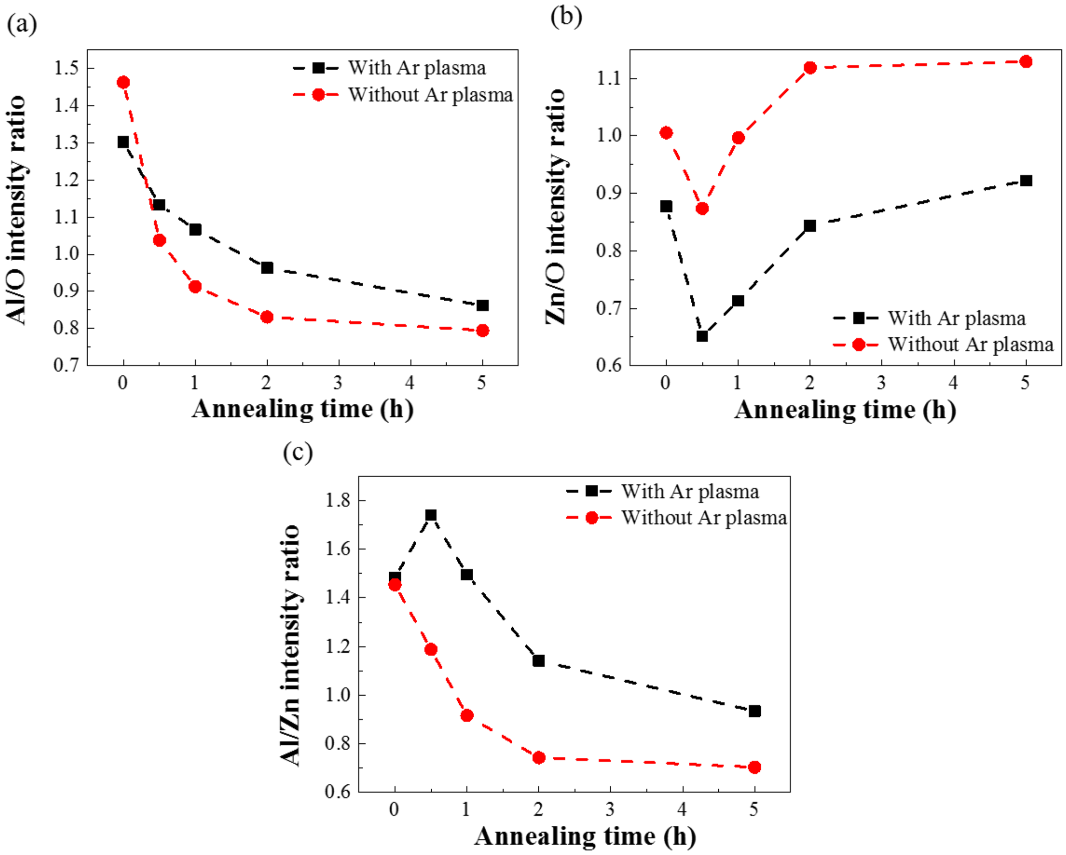

Fig. 5. 14. Evolution of HAXPES relative intensity ratios of Al 1s/O 1s (a), Zn 2p/ O1s (b) and Al 1s/Zn 2p (c) of Ar plasma treated Al (8.7 nm)/AZO sample with annealing time in air at 500 °C

The interaction and interdiffusion between Al metal capping and AZO layer could be decelerated by Ar plasma in low vacuum chamber. This is not only benefit in our study to improve thermal stability of Al/AZO samples, but also useful for other application. In electronics devices, Al was frequently used as electrode, for instance, in ZnO based surface acoustic wave (SAW) devices [26], or thin film transistor [27]. The interaction and interdiffusion between metal and oxide layer strong influenced on performance of such devices, and it should be prevented [27]. Our result suggests a simple method of using plasma to decelerate the interdiffusion between metal and oxide layer for these applications.

5.5. Conclusions

This chapter presented our studies on the thermal stability of electrical properties of AZO sample under annealing in air. The results showed that the electrical properties of AZO samples were strongly degraded under annealing in air, due to strong effect of oxygen from environment. Using ultrathin Al film as capping layer can improve thermal stability of AZO film, but its effect was not adequate to completely prevent the degradation. Thicker Al films have been employed to further improve thermal stability of bottom AZO layer. The results suggest that thick Al film can help to improve thermal stability of AZO layer. Low resistivity state of AZO layer can be retained for long duration of annealing in air, even at high temperature of 500 °C. Thicker Al film would lead to longer retention time. The results suggested that optoelectrical properties of Al/AZO samples strongly depends on the interaction and interdiffusion between Al capping and bottom AZO layer. There were two stages of evolution of electrical and optical properties with annealing time. During the first stage, before getting transparent at a characteristic time, the low resistivity of Al/AZO samples was kept, and an absorption peak in Vis range appeared. The interaction and interdiffusion between Al capping layer and bottom AZO layer occurred during annealing, resulted in existence of a non-equilibrium layer, up to the characteristics time. Afterward, chemical states of Al/AZO sample were saturated, and Al/AZO sample was in equilibrium state. The absorption peak in Vis range disappeared, and resistivity of Al/AZO samples started to raise.

Our study also found that the Ar plasma treatment in low vacuum chamber before annealing can decelerate the interaction and thermal interdiffusion of atoms between Al capping layer and bottom AZO layer, resulted in longer retention time of low resistivity of Al/AZO samples. The study suggest that a highly transparent and highly conductive Al/AZO transparent electrode can be realized by using appropriate thickness of Al capping layer depending on the fabrication process of the devices.

References

[1]. I. H. Kim, D. Y. Ku, J. H. Ko, D. Kim, K. S. Lee, J. -H. Jeong, T. S. Lee, B. Cheong, Y.-J. Baik, W. M. Kim, J Electroceram, 17 (2006) 241-245.

[2]. J. Montero, C. Guillén, J. Herrero, Thin Solid Films, 519 (2011) 7564-7567.

[3]. Y. -F. Chang, C. -L. Liao, C. -L. Ho, A. -S. Liu, M. -C. Wu, ECS J. Solid State Sci. Technol., 2 (2013) N140-N144.

[4]. N. Formica, D. S. Ghosh, A. Martinez-Otero, T. L. Chen, J. Martorell, V. Pruneri, Appl. Phys. Lett., 103 (2013) 183304.

[5]. T. Dimopoulos, G. Z. Radnoczi, Z. E. Horváth, H. Brückl, Thin Solid Films, 520 (2012) 5222-5226.

[6]. H. Tong, Z. Deng, Z. Liu, C. Huang, J. Huang, H. Lan, C. Wang, Y. Cao, Appl. Surf. Sci., **257** (2011) 4906-4911.

[7]. J. Huang, R. Tan, Y. Zhang, J. Li, Y. Yang, X. Zhang, W. Song, J. Mater. Sci.: Mater. Electron., **23** (2012) 356-360.

[8]. G. Haacke, J. Appl. Phys.,**47** (1976) 4086.

[9]. T. L. Chen, D. S. Ghosh, D. Krautz, S. Cheylan, V. Pruneri, Appl. Phys. Lett., **99** (2011) 093302.

[10]. C. C. Wu, RSC. Adv. **8** (2018) 11862.

[11]. G. Torrisi, E. Cavaliere, F. Banfi, G. Benetti, R. Raciti , L. Gavioli, A. Terrasi, , Sol. Energy Mater. Sol. Cells, 199 (2019) 114-121.

[12]. Z. Chen, Y. Liu, W. Zhang, X. Guo, L. Yin, Y. Wang, L. Li, Y. Zhang, Z. Wang, T. Zhang, Mater. Chem. Phys., **221** (2019) 78-88.

[13]. D. -H. Kim, K. -S. Cho, H. -K. Kim, Sci. Rep., **7** (2017) 2550.

[14]. W. Wang, M. Song, T. -S. Bae, Y. H. Park, Y. -C. Kang, S. -G. Lee, S. -Y. Kim, D. H. Kim, S. Lee, G. Min, G. -H. Lee, J. -Wook. Kang, J. Yun, Adv. Funct. Mater., **24** (2014) 1551-1561.

[15]. M. F. Al-Kuhaili, M. A. Al-Maghrabi, S. M. A. Durrani, I. A. Bakhtiari, J. Phys. D: Appl. Phys. 41 (2008) 215302.

[16]. E. O. Filatova, A. S. Konashuk, J. Phys. Chem. C 119 (2015) 20755-20761.

[17]. C. C. Cheng, C. H. Chien, G. L. Luo, J. C. Liu, C. C. Kei, D. R. Liu, C. N. Hsiao, C. H. Yang, C. Y. Chang, J. Electro. Soc., 155 (2008) G203-G208.

[18]. S. Tanuma, C. J. Powell, D. R. Penn, Surf. Interface. Anal., 35 (2003) 268-275.

[19]. A. Regoutz, M. Mascheck, T. Wiell, S. K. Eriksson, C. Liljenberg, K. Tetzner, B.A.D. Williamson, D.O. Scanlon, P. Palmgren, Rev. Sci. Instrum., 89 (2018) 073105.

[20]. C. Tong, J. Yun, Y. -J. Chen, D. Ji, Q. Gan, W. A. Anderson, ACS Appl. Mater. Interfaces, 8 (2016) 3985-3991.

[21]. T. Koida, T. Kaneko, H. Shibata, Materials, 10 (2017) 141.

[22]. H. Makino, Y. Sato, N. Yamamoto, T. Yamamoto, Thin Solid Films, 520 (2011) 1407-1410.

[23]. Y. Gao, L. Marín, E. C. Mattson, J. Cure, C. E. Nanayakkara, J. -F. Veyan, A. T. Lucero, J. Kim, C. Rossi, A. Estève, J. Phys. Chem. C, 121 (2017) 12780-12788.

[24]. R. Knut, R. Lindblad, S. Grachev, J. Y. Faou, M. Gorgoi, H. Rensmo, E. Søndergård, O. Karis, J. Appl. Phys., 115 (2014) 043714.

[25]. M. Wu, T. Huang, C. Jin, L. Zhuge, Q. Han, X. Wu, IEEE Trans. Plasma. Sci., 42 (2014) 3687-3690.

[26]. X. Y. Du, Y. Q. Fu, S. C. Tan, J. K. Luo, A. J. Flewitt, S. Maeng, S. H.Kim, Y. J. Choi, D. S. Lee, N. M. Park, J. Park, W. I. Milne, J. Phys. Conf. Ser 76 (2007) 012035.

[27]. J. E. Lee, B. K. Sharma, S. -K. Lee, H. Jeon, B. H.Hong, H. -J. Lee, J. -H. Ahn, Appl. Phys. Lett. 102 (2013) 113112.

Chapter 6. Conclusions: findings and challenges

The primary goals of this thesis were finding the methods to improve optoelectrical properties of ZnO and AZO films, and improving the thermal stability of electrical properties of AZO films for application as transparent electrodes, as well as getting insight into the mechanism behinds the improvements. Below are our findings and the remained challenges which need further studies

6.1. Findings

Firstly, we explored that using post Ar plasma treatment in a low vacuum chamber can greatly enhance electrical and photoluminescence properties of ZnO based thin films, especially increase Hall mobility in significantly short exposure duration. Carefully simultaneous investigations on evolutions of electrical properties, optical properties, photoluminescence properties, and evolutions of structure properties, as well as evolution of surface morphologies of ZnO films with plasma treatment time have been done to understand the mechanism of the improvement and the effect of plasma treatment. Based on the evolution of electrical properties accompanied with evolution of photoluminescence spectra of different ZnO films, we found a strong correlation between electrical properties and photoluminescence properties. The increase in Hall mobility and reduction of deep level emissions were due to the defects passivation. Our studies confirmed the incorporation of ions/atoms from plasma into interior of ZnO film. We have found that the He plasma treatments in the same low vacuum chamber have similar effect on optoelectrical properties of ZnO films. On the contrary, O plasma in low vacuum chamber and Ar plasma in high vacuum chamber did not result in any improvement in optoelectrical properties of ZnO films. The results, together with the reduction of Hall mobility when the etching on the surface occurred, suggest the enhancement in optoelectrical properties is not resulted from bombardment of Ar ions. Investigation of depth profile of hydrogen concentration by secondary ions mass spectroscopy figured out that the improvement in optoelectrical properties of ZnO thin films might originated from incorporation of hydrogen during plasma treatment. Hydrogen atoms passivated the defects and acted as shallow donors. This study introduces new safety method to enhance optoelectrical properties of ZnO-based thin films, as well as help to get insight into the correlation of defects levels and their passivation with electrical properties of ZnO thin films. This method can be applied to enhance performance of ZnO thin films in optoelectrical applications such as transparent electrodes, transistor, light emitting diode, or random laser.

Regarding to the thermal stability of ZnO-based thin films, AZO films were subjected to the studies. The effect of annealing temperatures, annealing environments and crystallinity of the films, which was controlled by substrate temperature, on the thermal stability of electrical properties have been investigated. To improve thermal stability of AZO film, thin Al metal films were deposited as capping layers for AZO films. The roles of Al films on thermal stability of AZO films in different annealing environments were studied. Our study found that the annealing environments strongly affected to the thermal stability of electrical properties. The degradation of electrical properties of AZO films is not solely resulted from the migration of oxygen from ambience, but also resulted from Zn desorption and segregation of defects at grain boundaries. The sample grown at higher substrate temperature showed better crystallinity with better *c*-axis orientation, and therefore, they exhibited higher electrical conductivity and better thermal stability due to narrower grain boundaries. We found that using ultrathin Al capping layer, with thickness of only 2.2 nm, can effectively improve thermal stability of AZO films under annealing in N_2 gas, particularly in films with good *c*-axis orientation. Our results figured out that ultrathin Al film can suppress the Zn desorption from AZO samples, based on TDS spectra. All the Al capped AZO films exhibited good thermal stability of carrier concentration under annealing, but sample grown at low temperature did not show good thermal stability of Hall mobility as other films deposited at higher temperatures. These results strongly suggested the influence of substrate temperature, or film crystallinity, on thermal stability of AZO films, as well as the different factors governing the carrier concentration and Hall mobility. The increase of Hall mobility in good *c*-axis oriented AZO films with ultrathin Al capping layer at moderate annealing temperature of 400 °C, where interdiffusion have not yet occurred, implies that the improvement was not due to diffusion of Al. Our calculation of optical mobility from optical spectra using Drude model suggested that the mobility of charge carrier in grains was increased by annealing, and the reduction of Hall mobility was due to increase in GBs scattering by annealing. Our study showed that beside the contribution of crystalline domain alignment on GBs scattering, the Zn desorption induced the increase in GBs scattering. Other defects segregation to the GBs also occurred in AZO film deposited at low substrate temperature. Therefore, the degradation of Hall mobility strongly depended on substrate temperature. Using ultrathin Al capping layer, Zn desorption was passivated, but GBs scattering due to domain alignment and the defect segregation to GBs in sample with low substrate temperature could not be passivated. Accordingly, improvement in Hall mobility was observed in sample deposited at high temperature, but reduction was still observed in sample deposited at low temperature.

Though ultrathin Al capping layer resulted in an improvement in electrical conductivity and its thermal stability of good *c*-axis oriented AZO films under annealing in N_2 gas, it was not significantly effective for annealing in air at high temperature of ~500 °C, because of strong influence of oxygen. Thicker Al films were employed to investigate the ability of passivating oxygen migration. We explored that thick Al capping layer could prevent the degradation of AZO film under annealing in air. There was a strong correlation between electrical properties, optical properties and evolution of chemical states of Al/AZO during annealing. The interaction and interdiffusion between Al and AZO layer occurred. During this process, low resistance was kept and absorption peak in Vis range appeared. After a characteristic time, when the interdiffusion was saturated, and sample was in equilibrium state, the absorption peak disappeared and resistance of sample was increased. Ar plasma in low vacuum chamber can prevent the interaction and interdiffusion between Al capping layer and bottom AZO layer, then prolonging the retention time of low resistivity of capped samples. Our results on thin Al capping layer suggest an effectively method to improve both electrical properties of ZnO-based thin films and their thermal stability. This method is beneficial for application of ZnO–based thin films as transparent electrodes, especially applicable in high temperature processes.

6.2. Challenges

\+ Regards to the effect of Ar plasma in low vacuum chamber, we have found that the electrical properties and NBEs of ZnO films can be greatly enhanced, due to passivation effect and shallow donor states of H. However, defects identification is difficult, and further studies need to be done in order to verify what defects exist in ZnO films causing the high DLEs and low electrical conductivity.

\+ Thermal stability of AZO films was enhanced using thin Al capping layer. Because Al film might be oxidized into AlO_x layer, there must be one concern regarding to conduction through insulating layer. Because the thickness of capping layer was significantly thin, charge carriers may tunnel through it (Appendix A). Nevertheless, further study using Al/AZO films as transparent electrodes for optoelectronic devices should be done to verify the practical applicability of Al/AZO films.

\+ The evolution of optoelectrical properties of Al/AZO films was found strongly related to the interdiffusion between Al and AZO. The remaining of electrical properties was found correlated with the existence of an absorption peak in Vis range. However, origin of absorption peak in the Vis range was still mysterious, and it would be studied to figure out what behind the absorption peak in annealed Al/AZO sample and its benefit to the thermal stability of AZO layer.

Publications

[1]. **Hoa T. Dao,** Hisao Makino, “Enhancement in optoelectrical properties of polycrystalline ZnO thin films by Ar plasma”, ***Materials Science in Semiconductor Processing*** **96** (2019) 46–52.

[2]. **Hoa T. Dao,** Hisao Makino**,** “Improving electrical conductivity and its thermal stability of Al-doped ZnO polycrystalline films using ultrathin Al film as a passivation layer”, ***Solar Energy Materials and Solar Cells*** 203 (2019) 110159.

[3]. **Hoa T. Dao,** Hisao Makino, “The effects of interface layer between Al overlayer and Al-doped ZnO on thermal stability in high temperature oxidizing environment”, to be submitted.

[4]. **Hoa T. Dao,** Hisao Makino, “Effect of substrate temperature on thermal stability of AlO_X capped AZO thin film” to be submitted.

Acknowledgements

First of all, I would like to express my deepest gratitude to my supervisor, Prof. Hisao Makino for his guidance and precious advice during my PhD course. He has shared me lots of technical skills and scientific knowledge, which allow me to operate research experiments and help me to understand and improve my research work. His comments and feedbacks are greatly valuable for me to dealing with many challenges in doing research. I would like to thank him for his constant supporting, his patience and tolerance with me. Overcome my weakness, he constantly helped me and encouraged me, and gave me many advices, not only in doing research, but also in community.

I am also very grateful to all of the comments and feedbacks from professors in my assessment committee. Their comments were very valuable and meaningful for me to improve my work and my understanding. I would like to express my gratitude to Prof. Li Chaoyang, and Prof. Hiroshi Furuta, my co-supervisors, for their valuable advices and encouragements. I would like to thank Prof. Li Chaoyang for her sympathy and encouragement for me. Her comments are indispensable and very helpful for me to dealing with difficulties during my study. I would like to sincerely thank Prof. Hiroshi Furuta for teaching me to operate XPS system, and his patience to explain things for me. I would like to express my sincere gratitude to Prof. Mamoru Furuta for teaching me and helping me to use TDS system.

I would like to thank Dr. Junichi Nomoto, for his guidance on Ellipsometry system, and sharing his knowledge on research for me. I especially thank Dr. Dang Thai Giang and Dr. Philmophan Rutthongjan for guiding me to operate AFM and SEM system in Nano center.

I also deeply thank to SSP program for giving me a chance to enjoy studying. I would like to thank to all of IRC members for helping me during studying here.

Finally, I would like to spend lines to express my deepest love to my family, especially my parents and my daughter, who always encourage me and give me mental strength to overcome difficulties. I owe a debt of gratitude to them. I also would like to thank all of my friends here in KUT for sharing the happiness and troubles during studying in KUT.

Abbreviations

TE	Transparent electrode
TCO	Transparent conductive oxide
DLEs	Deep level emissions
NBEs	Near band edge emissions
UV	Ultraviolet
Vis	Visible
NIR	Near infrared range
GBs	Grain boundaries
LED	Light emitting device
CVD	Chemical vapor deposition
ALD	Atomic layer deposition
MS	Magnetron sputtering
RF MS	Radio frequency magnetron sputtering
DC MS	Direct current magnetron sputtering
PL	Photoluminescence
XRD	X-ray diffraction
XPS	X-ray photoelectron spectroscopy
HAXPES	Hard X-ray photoelectron spectroscopy
SXPS	Soft X-ray photoelectron spectroscopy
TDS	Thermal desorption spectroscopy
SIMS	Secondary ion mass spectroscopy
AFM	Atomic force microscopy
FE-SEM	Field effect scanning electron microscopy

$\mathbf{T_S}$	Substrate temperature
$\mathbf{T_A}$	Annealing temperature
T	Transmittance
R	Reflectance
$\boldsymbol{\mu_{opt}}$	Optical mobility
$\boldsymbol{\mu_{GB}}$	Grain boundary mobility

Appendix A

Electrical conduction through thin AlO_x capping layer

To verify the linear conduction through the AlO_x capping layer, which might evolve from Al film, we have performed the I-V curve measurement through AlO_x layer. The AlO_x capping layer was partly removed, allowing part of bottom AZO to be uncovered. Then an In electrode was deposited on AlO_x side and another electrode was deposited on AZO side. For comparison, we deposited another electrode on AZO side. The electrodes have similar size, and their distances were similar, as illustrated on Fig. A. 1.

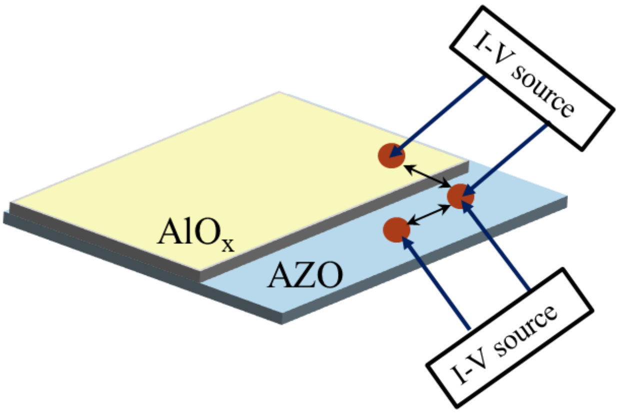

Fig. A. 1. Configuration of electrodes on Al/AZO samples to investigate the I-V curve

Fig. A.2 shows the I-V curves measured on as-deposited Al (2.2 nm)/AZO sample and on Al (8.7nm)/AZO sample after annealing in air at 500 °C for 2 h. The I-V curves measured between electrodes on AlO_x and on AZO (AlO_x – AZO) were compared with I-V curves measured between two electrodes both on AZO. All of the I-V curves were linear, and quite identical, implying that resistance of AlO_x layer was negligible, and would not prevent the conduction of charge carrier in practical devices. AlO_x removing process somehow caused the bad contact on the surface of AZO, leading to slightly higher resistance between electrodes on AZO.

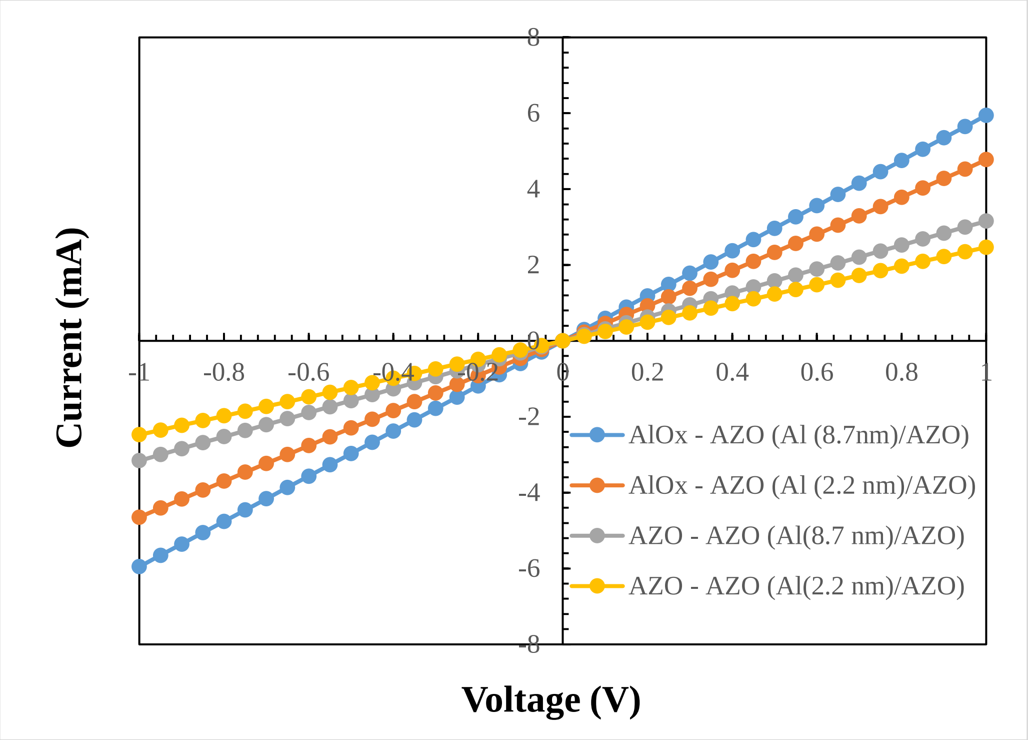

Fig. A. 2. I-V curve measured on as-deposited Al (2.2 nm)/AZO and annealed Al(8.7 nm)/AZO (annealed in air at 500 °C for 2 h)

The contact resistances were also investigated on annealed Al (8.7nm)/AZO and as-deposited AZO samples using transmission line model to evaluate the effect of capping layer to the resistance of electrical contact in practical application. Fig. A.3 (a) show a schematic view of the In contacts which were deposited on samples in configuration of a transmission line. The resistances were then measured between neighboring In contacts. The measured resistances were presented in Fig. A. 3 (b). The observed contact resistances (Rc) were 3.13 Ω and 2.70 Ω for annealed Al/AZO, and as-deposited AZO sample, correspondingly. The contact resistance was not much increased in capped sample, suggesting a negligible effect of AlO_x layer on contact resistance. Accordingly, Al/AZO samples are possibly employed as TCO in practical application.

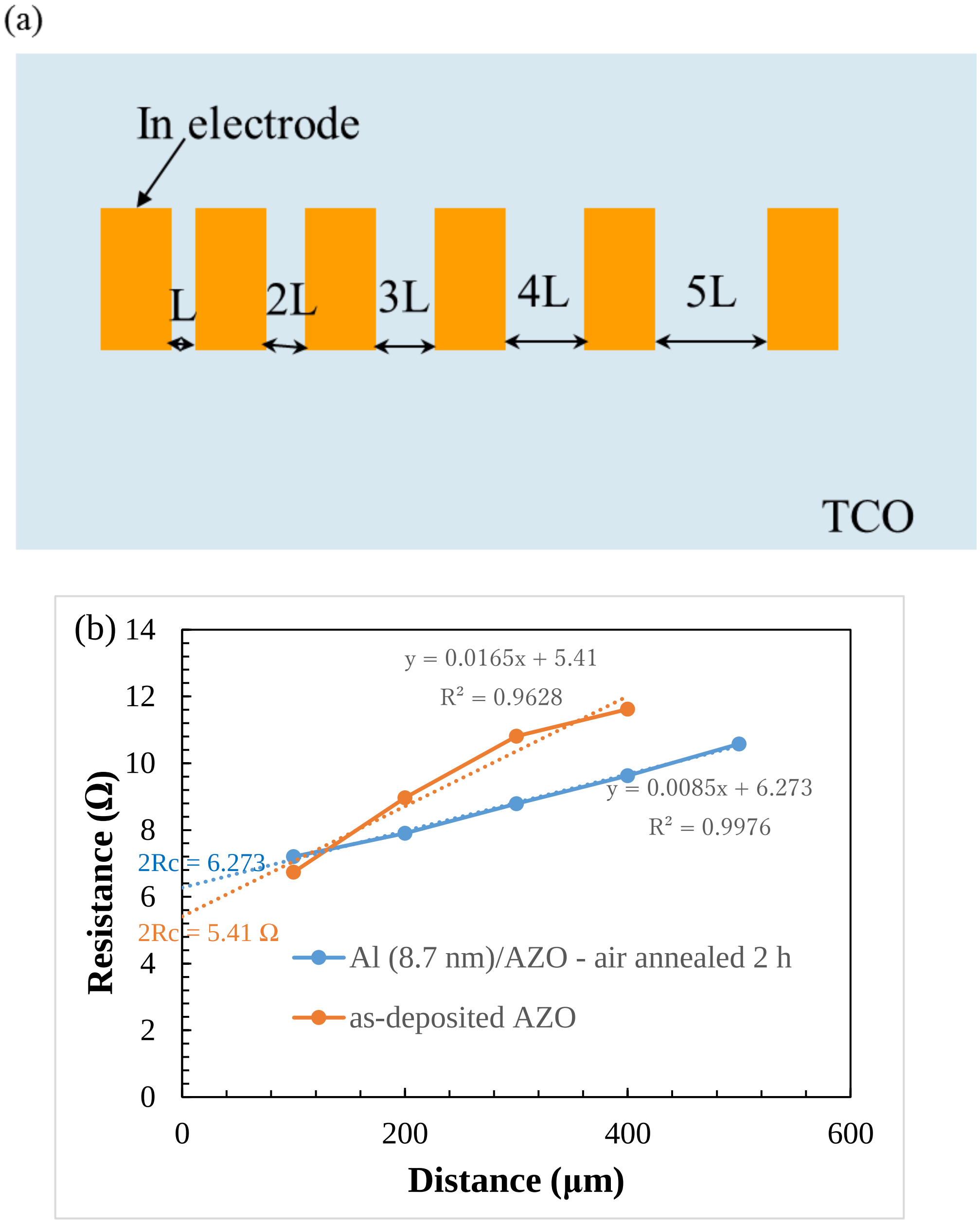

Fig. A. 3. Transmission line model for investigation of contact resistance (a), and evolution of measured resistance with distance between In electrodes (b). The dashed lines show the linear evolution of resistance.

Even if AlO_x film acts as insulating layer, because of significantly thin thickness, charge carrier can tunnel through it when the Al/AZO film is used as electrode. Below is an example of band alignment and electron transfer in a dye sensitized solar cell (Fig. A. 3) if using Al/AZO film as TE. Electron can transfer from conduction band of semiconductor layer to the AZO layer by tunneling through AlO_x layer.

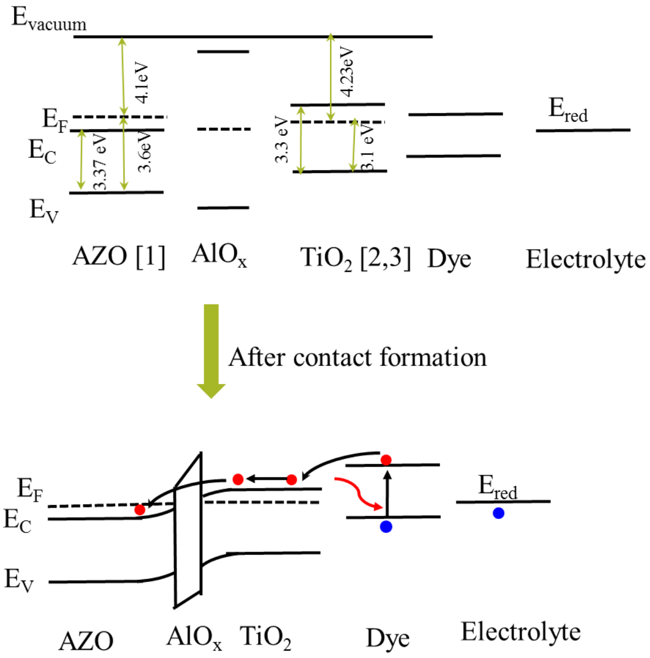

Fig. A. 4. An illustration of band alignment when contact was formed – an example for Dye-sensitized solar cell. Electron can tunnel through the thin AlO_x layer [4, 5].

References

[1]. J. K. Jha, W. Sun, J. Du, N.l D. Shepherd, J. Appl. Phys., **121** (2017) 185304.

[2]. S. Kashiwaya, J. Morasch, V. Streibel, T. Toupance , W. Jaegermann, A. Klein, Surfaces 1 (2018) 73–89.

[3]. Z. Xu, J. Wu, T. Wu, Q. Bao, X. He, Z. Lan, J. Lin, M. Huang, Y. Huang, L. Fan, Energy Technol. 5 (2017) 1820 – 1826.

[4]. B. Bill, M. Shanmugam, M. F. Baroughi, Thin Solid Films, 519 (2011) 7803-7808.

[5]. A. Ashok, S. N. Vijayaraghavan, S. V. Nair, M. Shanmugam, RSC Adv. 7 (2017) 48853.